HIGH TRANSVERSE MOMENTUM HADRON PRODUCTION IN 400 AND 800 GEV/C PROTON-NUCLEON COLLISIONS

A Dissertation presented

by

David Edward Jaffe

to

The Graduate School

in Partial Fulfillment of the Requirements

for the Degree of

DOCTOR OF PHILOSOPHY

in

Physics

State University of New York

at

Stony Brook

August 1987

STATE UNIVERSITY OF NEW YORK
AT STONY BROOK

THE GRADUATE SCHOOL

David Edward Jaffe

We, the dissertation committee for the above candidate for the Ph.D. degree, hereby recommend acceptance of the dissertation.

Dr. Robert L. McCarthy, Professor, Physics

Dr. Roderich J. Englemann, Professor, Physics

Dr. Paul D. Grannis, Professor, Physics

Dr. John Smith, Professor, Physics

Dr. Michael Sivertz, Senior Research Associate, Physics
Temple University

This dissertation is accepted by the Graduate School.

Graduate School

Abstract of the Dissertation

HIGH TRANSVERSE MOMENTUM HADRON PRODUCTION IN 400 AND 800 GEV/C PROTON-NUCLEON COLLISIONS

by

David Edward Jaffe

Doctor of Philosophy

in

Physics

State University of New York at Stony Brook

1987

Results of high transverse momentum hadron production in 400 *Gev/c* proton-proton and proton-deuteron and 800 *Gev/c* proton-proton collisions are presented in this dissertation. The transverse momentum range of the data was from 5.2 to 9.0 *Gev/c* for the 400 *Gev/c* collisions and from 3.6 to 11.0 *Gev/c* for the 800 *Gev/c* collisions; the data were centered around the proton-nucleon center-of-momentum production angle of 90°. Single pion invariant cross sections and particle ratios were measured at both energies and the unlike-sign dihadron correlation function was measured at the higher energy. The results are compared to previous experiments and the Lund model.

Table of Contents

List of Tables

List of Figures

Acknowledgements

They gave me money
to find the sky.
And I took it with no questions
didn't even ask them why.
But days are open
and skies are free.
And the time it took to learn that
couldn't leave its chains on me.
I lived in shadows
way from the sun.
And the trembling in my mind
kept my heart and body on the run.
Then freedom called us,
called out our names.
And the beckoning of its highway
saw through all our useless games.

"Song for the North Star"
Jorma Kaukonen

I. A. Introduction

In the framework of quantum chromodynamics(QCD) and the parton model, the inclusive, high transverse momentum($p_\perp$), single hadron production cross section is written as (neglecting intrinsic transverse momentum of the partons)[1]

$$E\frac{d^3\sigma}{dp^3}(AB \to CX) = \int dx_a f_a^A(x_a,Q^2)dx_b f_b^B(x_b,Q^2)\times \left[\hat{E}\frac{d^3\hat{\sigma}}{d\hat{p}^3}(ab \to cd)\right]\frac{dz_C}{z_C^2}D_C^c(z_C,Q^2)$$

where A and B are the beam proton and target nucleon, respectively, C is the observed high $p_\perp$ hadron and a sum over the permutations of a,b,c and d is implied. The structure function, $f_a^A(x_a,Q^2)$, is the probability dnesity of finding parton a in proton A with longitudinal momentum fraction x_a; the fragmentation function, $D_C^c(z_C,Q^2)$, is the probability density to produce hadron C from parton c with longitudinal momentum fraction z_C. One assumption of the parton model is that both distribution functions can be measured independently. Structure functions are measured in deeply inelastic lepton-nucleon scattering; fragmentation functions are determined

[1] R.D. Field, "Applications of Quantum Chromodynamics", CALT-68-696, Lectures given at La Jolla Institute Summer Workshop, July 31 - Aug. 18, 105 (1978); A.P. Contogouris, R. Gaskell and S. Papadopoulos, Phys. Rev. D17, 2314 (1978).

from hadron production in electron-positron interactions.

The fundamental scattering of partons a and b to produce partons c and d is described by the invariant cross section $\hat{E}\frac{d^3\hat{\sigma}}{d\hat{p}^3}(ab \to cd)$. Explicitly,[2]

$$\hat{E}\frac{d^3\hat{\sigma}}{d\hat{p}^3}(ab \to cd) = \frac{\hat{s}}{\pi}\delta((p_a + p_b - p_c)^2 - m_d^2)\frac{d\sigma}{d\hat{t}}(ab \to cd),$$

where p_l = four-momentum of parton l, $\hat{s} = (p_a + p_b)^2$, $\hat{t} = (p_a - p_c)^2$, $\hat{u} = (p_a - p_d)^2$ and m_d = mass of parton d. The "hard-scattering" cross section $\frac{d\sigma}{d\hat{t}}(ab \to cd)$ includes the possible parton sub-processes that can contribute to the cross section; namely quark-quark(qq), quark-gluon(qg) or gluon-gluon(gg) scattering.

The scale of the interaction is set by the characteristic momentum transfer squared, Q^2. Naively Q^2 would be the square of the momentum transfer in the "hard-scattering" subprocess, but since several sub-processes can contribute to the cross section, the definition of Q^2 is ambiguous. Different choices of Q^2 have been,

1) $Q^2 = 2\hat{s}\hat{t}\hat{u}/(\hat{s}^2 + \hat{t}^2 + \hat{u}^2)$ which is symmetric in $\hat{s}, \hat{t}$ and $\hat{u}$,[3]

2) $Q^2 = -\hat{t}$ and $Q^2 = -\hat{u}$ at center-of-momentum production angle $\Theta^* = 90°$ in qq $\to$ qq interactions mediated by single gluon exchange,[4]

3) $Q^2 = -\hat{t}\ (-\hat{u})[\hat{s}]$ at $\Theta^* = 90°$ for the $\hat{t}(\hat{u})[\hat{s}]$ channel;[5]

[2] R. Cutler and D. Sivers, Phys. Rev. D16, 679 (1977).
[3] Field, CALT-68-696; R.D. Field, Phys. Rev. Letters 40, 997 (1978).
[4] Contogouris et al.
[5] Cutler and Sivers.

however, the choice of Q^2 does not significantly affect the results at $\Theta^* \approx 90°$.[6] The structure and fragmentation functions depend on Q^2; emission of gluons by the interacting partons before and after the "hard-scattering" modifies the parton momentum, resulting in more low x partons as Q^2 increases. The difficulties in measuring $\frac{d\sigma}{d\hat{t}}(ab \rightarrow cd)$ are apparent; however, there is no more direct method to investigate the nature of short distance (high Q^2), gluon-mediated parton-parton interactions than proton-proton or proton-neutron scattering.

Two aspects of hadronic interactions can be studied in proton–proton and proton–neutron collisions. Since the "hard–scattering" process is thought to be quark flavor independent, the relative production rates of each hadron species emphasize the effect of nucleon structure and parton fragmentation. In addition, as indicated in the initial equation of this section, measurement of the transverse momentum dependence of the single hadron invariant cross–section yields insight into the convolution of hadron structure, fragmentation and "hard–scattering" cross–section.

The naive, scale-invariant prediction for high $p_\perp$ hadron production based on simple fermion-fermion scattering mediated by a vector boson is[7]

$$E\frac{d^3\sigma}{dp^3}(AB \rightarrow CX) = f(x_\perp, \Theta^*)/p_\perp^N$$

---

[6] *Ibid.*

[7] Field, CALT-68-696; Field, Phys. Rev. Letters 40, 997 (1978); F.E. Close, An Introduction to Quarks and Partons (London, Academic Press, 1979),312.

where $x_\perp = 2p_\perp/\sqrt{s}$ and $s = (p_A + p_B)^2$. However, the Q^2 dependence of the structure and fragmentation functions and the intrinsic transverse momentum of the incident partons in a nucleon substantially complicates this picture so that N is a function of both $p_\perp$ and $\sqrt{s}$.[8] Nevertheless, the naive prediction roughly fits the data on $pp \rightarrow \pi^\pm X$ in the range $.25 < x_\perp < .6$ and $19.4 < \sqrt{s} < 62.4$ Gev at $\Theta^* \approx 90^o$ with $N \approx 8$.[9]

Results presented in this thesis cover a range of angles near $\Theta^* \approx 90^o$ at $\sqrt{s} = 27.4$ and 38.8 Gev with full hadron species identification. The following table displays the kinematic range and reactions explored:

Table 1: Reactions and Kinematic Ranges

Reaction	$\sqrt{s}$ (Gev)	$p_\perp$ range (Gev/c)	$x_\perp$ range	$\cos\Theta^*$ range
$pp(d) \rightarrow hX$	27.4	5.2 - 9.0	.38 to .66	$-.3$ to .3
$pp \rightarrow hX, hhX$	38.8	3.6 - 11.0	.19 to .57	$-.2$ to .2

[8] J.F. Owens, E. Reya and M. Glück, Phys. Rev. D18, 1501 (1978).

[9] D. Antreasyan et al, Phys. Rev. D19, 764 (1979);D. Antreasyan et al, Phys. Rev. Letters 38, 112 (1977);B. Alper et al, Nucl. Phys. B100, 237 (1975); F.W. Büsser et al,Nucl. Phys. B106, 1 (1976).

Since it has been shown[10] that the quantum numbers of high $p_\perp$ hadrons are correlated with the flavor of the scattered parent parton, hadron species identification allows the study of the quantum number flow in each interaction. For example, the relative production rates of π^+ ($u\bar{d}$ valence quarks) and π^- ($d\bar{u}$) naively reflects the valence u and d content of the proton — assuming that $\bar{u}$ or $\bar{d}$ quark production is equally probable during fragmentation; while the K^+ ($u\bar{s}$) to π^+ ratio yields the relative $\bar{s}$ and $\bar{d}$ fragmentation production probabilities.

I. B. The Lund Model

The measured hadron species production rates are compared with predictions of the Lund model to further elucidate the specific nature of the QCD interaction. The Lund monte carlo is an attractive model to describe single- and multi-particle production in hard-scattering processes involving partons (quarks, gluons and di-quarks).[11] A typical Lund-generated 'event' has three parts:

1) the primary partons colliding at high Q^2 with the interaction calculated to lowest order in perturbative QCD,

2) the partons receding from each other stretching a color 'string'

[10] A. Breakstone et al., Z. Phys. C25, 21 (1984) and references therein; A.L.S. Angelis et al, Nucl. Phys. B209, 284 (1982); T. Åkesson et al, Nucl. Phys. B246, 408 (1984).

[11] Andersson et al., Phys. Reports 97, 31 (1983); H.-U. Bengtsson and G. Ingleman, CERN preprint LU TP 84-3, Th.3820 (1984); T Sjöstrand, Computer Physics Communications,27, 243 (1982)

that eventually yields to confinement forces to produce primary hadrons and

3) the unstable hadrons decaying into observable hadrons.

The model is theoretically appealing because, among other reasons, it is Lorentz invariant and treats events as a whole unlike earlier independent fragmentation models.[12]

Predictions of inclusive meson and baryon production in e^+ e^- interactions have been fairly successful[13] but rely on several adjustable parameters of the monte carlo. Two relevant, relatively well-determined parameters in the Lund model are $P(s)/P(u)$, the strangeness suppression factor, where $P(q)$ is the probability to create a $q\bar{q}$ pair in the fragmentation chain, and $P(qq)/P(q)$, the di-quark suppression factor. Meson production rates in e^+ e^- scattering give the 'standard' Lund parameter values $P(s)/P(u) = .3$, while baryon production sets $P(qq)/P(q)$ to .1 .

On this basis the Lund monte carlo is useful in relating fragmentation processes in hadron–hadron collisions to the fragmentation of quarks and gluons in electron-positron annihilation.

Single hadron production in proton–proton[14] and muon–

[12] R.D. Field and R.P. Feynman, Nucl. Phys. B136, 1 (1978); Field and Feynman, Phys. Rev. D15, 2590 (1977); R.P. Feynman et al., Nucl. Phys. B128, 1 (1977)

[13] M. Althoff et al., Z. Phys. C17, 5 (1983); H. Aihara et al., Phys. Rev. Letters 53, 2199 (1984); Ch. Berger et al., Nuclear Physics B124, 189 (1983); M. Derrick et al., Phys. Letters 158B, 519 (1985); M. Derrick et al., Phys. Rev. Letters 54, 2568 (1985); W. Bartel et al., Phys. Letters 104B, 325 (1981); P. Baringer et al., ANL-HEP-PR-85-121 (1985)

[14] T. Åkesson et al., Nuclear Physics B246, 408 (1984); A. Breakstone et al., Z. Phys. C28, 335 (1985)

proton[15] interactions has been compared with Lund predictions. Several discrepancies are notable:

1) The predicted production ratio of K^+/π^+ at high $p_\perp$ in proton–proton collisions is significantly less than the experimentally determined value of .46 — suggesting that the strangeness suppression factor in fragmentation differs in pp and $e^+ e^-$ hadron production.

2) Fewer anti-protons are observed than predicted, possibly indicating a decrease in the probability to create di-quark pairs in the fragmentation chain in pp compared to $e^+ e^-$ interactions.

3) More low $p_\perp$ protons than expected by the Lund model are observed — possibly due to the presence of an intrinsic, spin-zero ud di-quark in the proton,[16] which is neglected in the Lund model.

[15] J.J. Aubert et al., Phys. Letters 135B, 225 (1984)
[16] S. Ekelin and S. Fredriksson, Phys. Letters, 149B, 509 (1984)

II. Apparatus

Experiment 605 (E605) was a focussing magnetic spectrometer designed to study long-lived, charged, high $p_\perp$ particles near 90° in the proton-nucleon center-of-momentum system (CMS) produced in 400 and 800 *Gev/c* proton-nucleus collisions.[17] The successful suppression of backgrounds led to E605's ability to measure relatively small cross sections at high $p_\perp$. Full hadron species identification was achieved with a ring-imaging Čerenkov counter to distinguish pions (π), kaons (K), and protons (p). Electrons were differentiated from hadrons by calorimetry, and muons were identified by scintillation counter hodoscopes and proportional tubes behind many absorption lengths of dense shielding. See Figure 1.

II. A. Beam

Both 400 and 800 *Gev/c* proton beams were delivered to this experiment for two separate running periods. The beam was slowly extracted from the Fermi National Accelerator Laboratory (Fermilab) Tevatron in a 15(20) second spill for the 400(800) *Gev/c* running.

[17] FNAL-605, in Major Detectors in Elementary Particle Physics, Particle Data Group, LBL-91 Supplement, revised (1985).

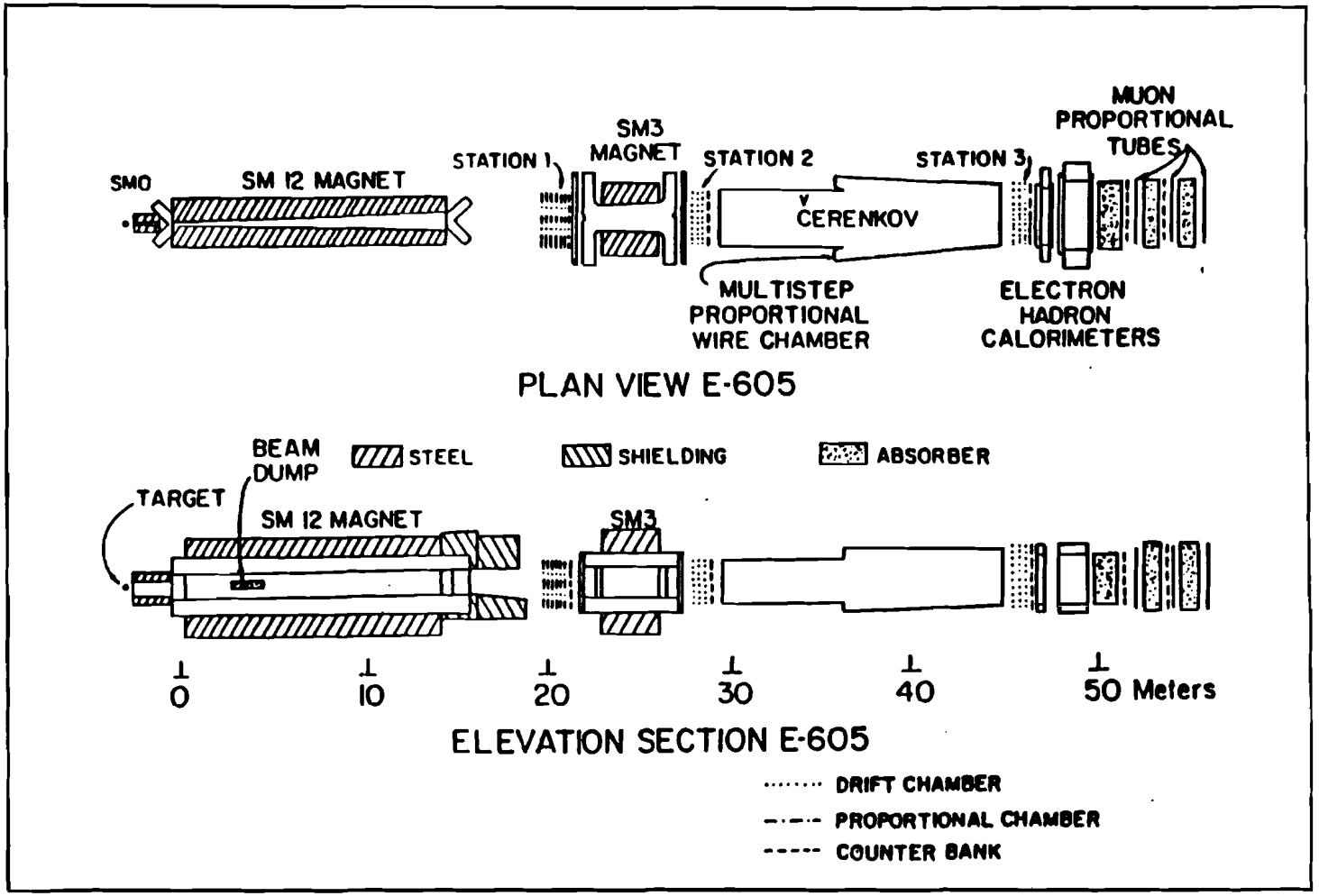

Figure 1. E605 Spectrometer

During extraction the radio frequency (RF) accelerating field of the proton synchotron remained on, so the extracted beam remained in bunches about 1 nanosecond(*ns*) long separated by 18.9 *ns*. The beam was brought through the main switchyard and Meson switchyard and transported to the Meson East beamline. The Meson East beamline contained 3 superconducting dipole magnet strings, 5 pairs of quadropole magnets, and 4 vertical vernier magnets as shown in Figure 2.

The resulting beam profile at the E605 target was determined to be roughly gaussian in both the vertical (Y) and horizontal(X) directions with a vertical root mean square (RMS) deviation of about .19 *mm* and a horizontal RMS deviation of about 2.3 *mm* for both running periods. The RMS angular divergence of the beam was determined to be approximately .68 milliradians(*mrad*) vertically and .06 *mrad* horizontally.

Two methods were used to measure the beam position and profile at the target. A retractable wire chamber (SWIC) with wires spaced .5*mm* (2.0*mm*) in the vertical (horizontal) direction was lowered into the beam approximately 1 meter upstream of the target.[18] The position of the beam at the SWIC was checked approximately once before each data run and was stable to ± .2 *mm* (2.0 *mm*) [limit of error] in the Y(X) direction for each running period.

[18] Secondary particle production by the proton beam incident on the SWIC produced a non-negligible background rate in the detector; hence, the SWIC was placed out of the beam during data taking.

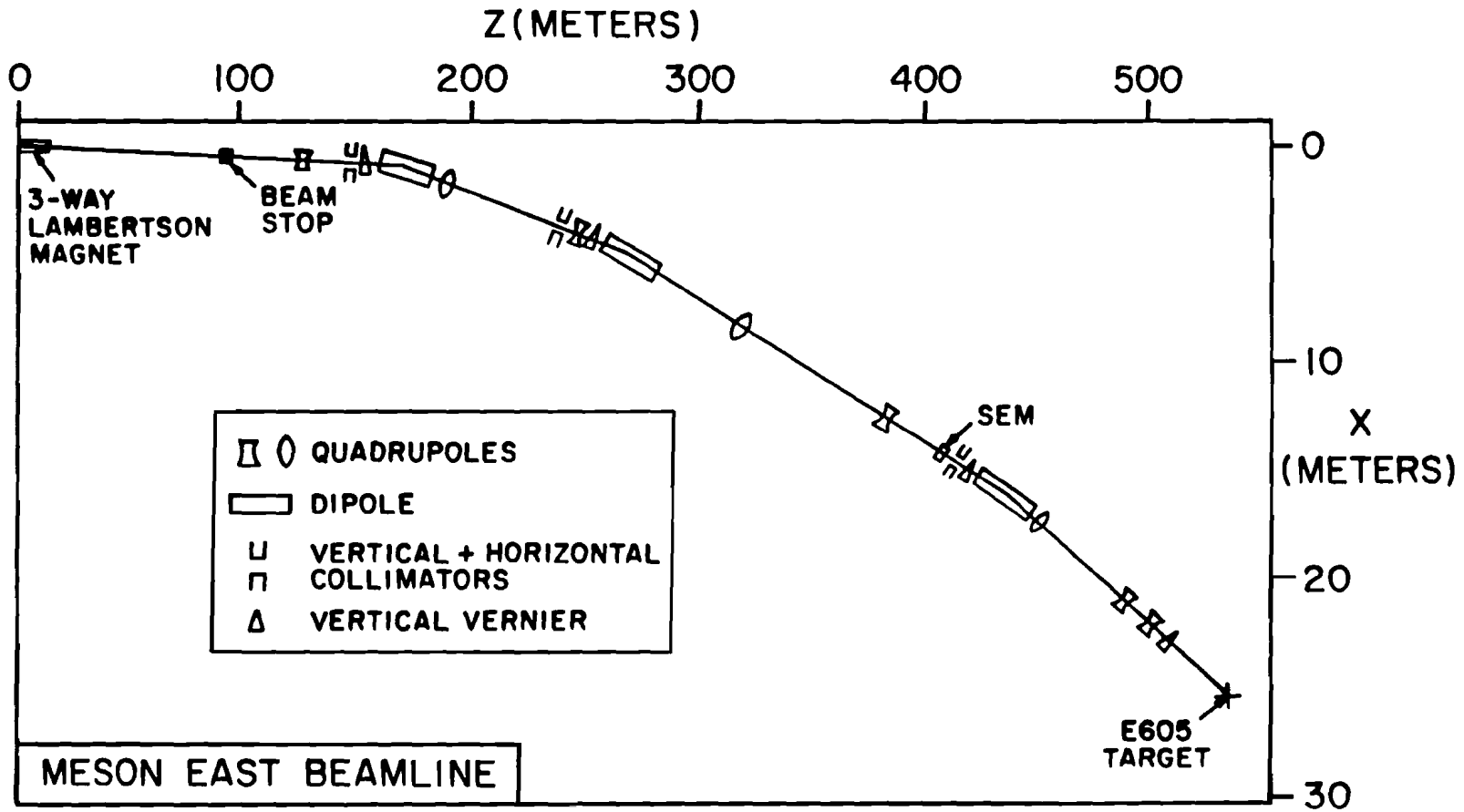

Figure 2. Meson East Beamline

The beam profile at the target (Figure 3) was inferred from the relative beam–target interaction rate[19] on thin metal targets moved through the incident beam. The metal target scans were interspersed with the liquid target data taking. Since the measured beam profile agreed with that predicted by beamline optics, it was assumed that the angular divergence of the beam was correctly determined by the optics of the beamline. In Figure 3 the X-profile curve is a hand–drawn fit.

During all the data taking runs, the beam intensity per spill was measured with a secondary emission monitor (SEM) located upstream of the last superconducting dipole string. A special run was taken during both the 400 and 800 *Gev/c* running periods to calibrate the SEM by foil activation. The results of the calibration runs were $(8.41 \pm .31)\times10^7[(8.52 \pm .53)\times10^7]$ protons-on-target per SEM count for the 400[800] *Gev/c* running.

II. B. Target

The liquid target vessel and its refrigeration unit — along with a rack of metal targets — were situated in an aluminum 'target box' mounted on the upstream face of the first spectrometer magnet. The position of the liquid and metal targets and the emptying and filling of the liquid target vessel were remotely controlled. The liquid target vessel was a cylinder of 25 *micron* thick stainless steel, 5.08 *cm* in dia-

[19] The interaction rate in the target was measured with a scintillation telescope, "AMON", fully described in Section V.B.

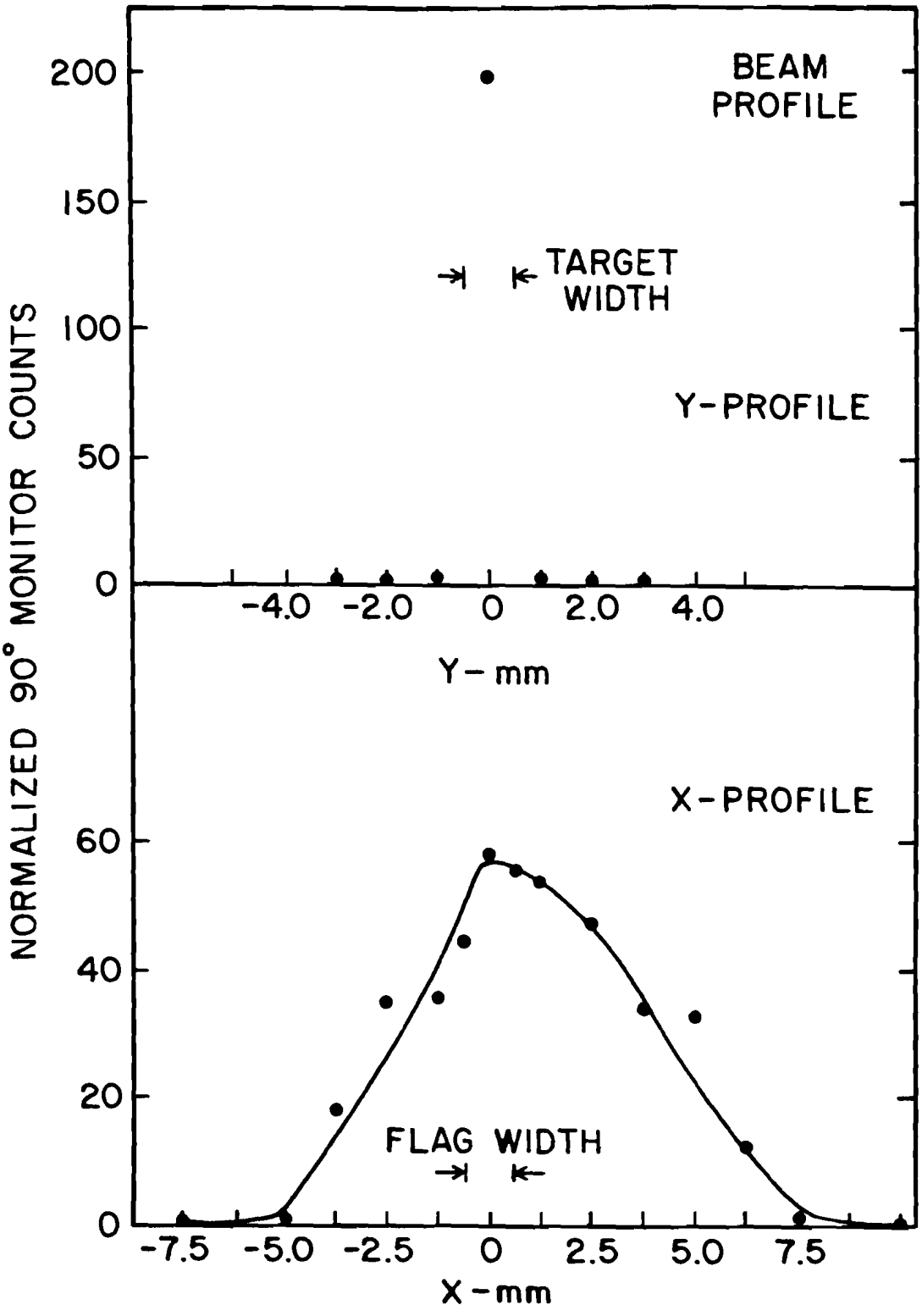

Figure 3. Beam Profile

meter and 20.2 ± .1 *cm* long when cooled to liquid hydrogen(LH_2) or liquid deuterium(LD_2) temperatures. The target vessel was enclosed in a thick aluminum block under vacuum with 5.08 *cm* diameter end windows of 25 *micron* stainless steel. These two thin windows were located 3.6 *cm* upstream and 1.5 *cm* downstream of the ends of the target vessel as shown in Figure 4. All detected secondary particles passed through the two downstream thin stainless steel windows only.

When the target was filled, the liquid level was maintained such that the entire target vessel was full of liquid, slightly below the boiling point, at 14.7 ± .3 *psi* .[20] The emptied target contained gas slightly above the boiling point at the same pressure. To correct the cross section for secondary production in the stainless steel windows, one emptied target run was taken for about every 3(4) $LH_2(LD_2)$ data runs. Emptying the target took less than a minute; filling typically took a few minutes.

The liquid hydrogen used in the target was measured[21] to be > 99.99% pure; the two different batches of liquid deuterium used were found to be 98.5% D_2, 1.5% HD and 95% D_2, 5% HD (percent by volume), respectively. It was necessary to use the second batch of deuterium when a refrigerator malfunction cracked the target vessel and vented the first batch. No correction was made to the measurement of the single hadron cross section to account for the slight hydrogen contamination of the "deuterium" target.

[20] J. Peifer, Fermilab liquid target group, private communication.
[21] J. Peifer.

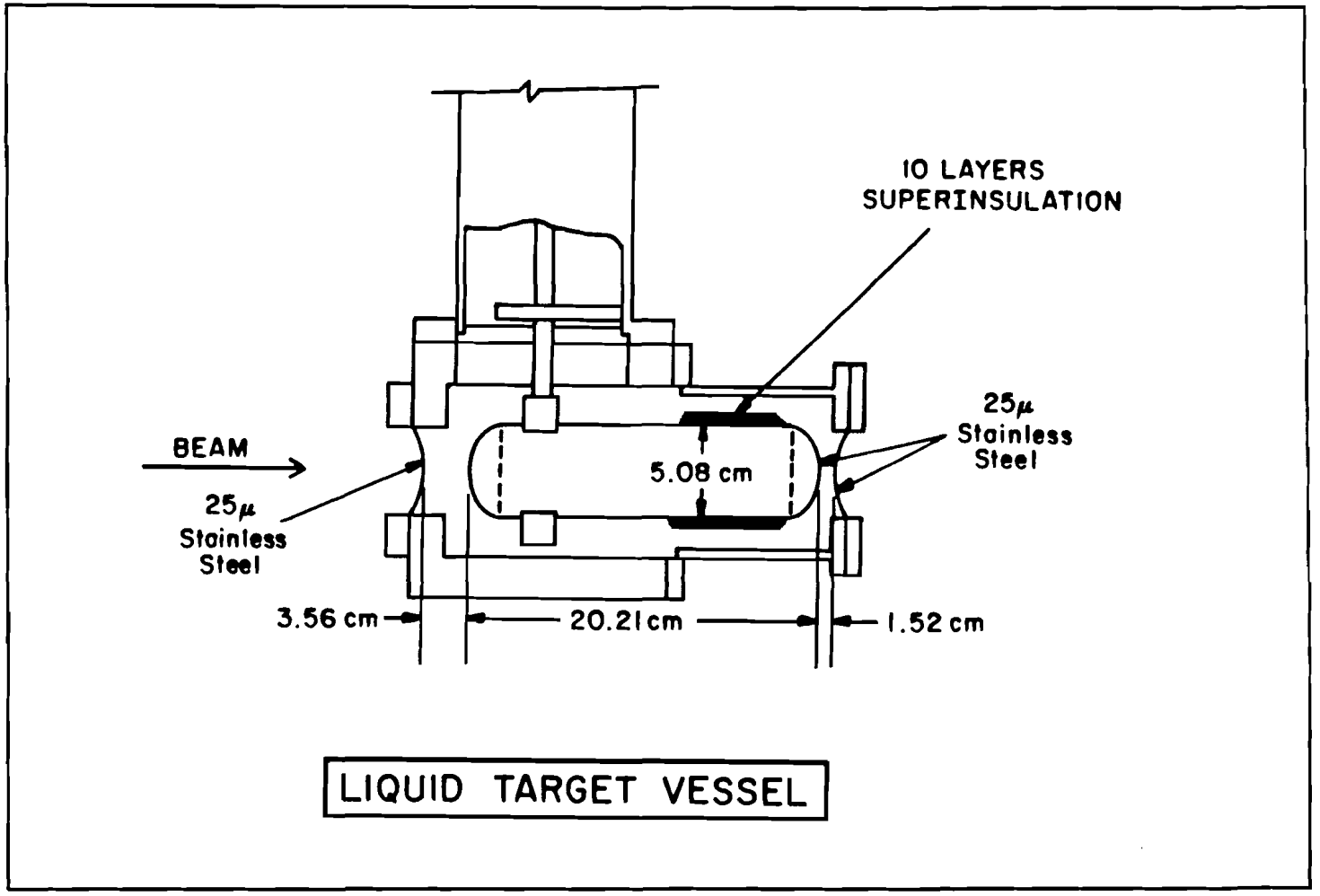

Figure 4. Liquid Target Vessel

II. C. Magnets

Three conventional, iron yoke dipole magnets were used to focus and momentum-analyse high $p_\perp$ particles produced in the target. These magnets were called, for historical reasons, SM0, SM12 and SM3 in order of increasing distance from the target. All magnets had the major component of the magnetic field in the horizontal direction, thus bending charged particles vertically.

The first magnet's yoke started approximately 33 *cm* from the center of the target. It was a standard BM-109 dipole[22] shimmed to have a horizontal gap width of 8.8(12.4) *cm* at the upstream(downstream) end; the vertical gap width was 42.9 *cm* and the length of the iron yoke was 1.83 *m*. The shimmed insert attached to the target box and consisted of a welded box with soft-iron sides and stainless steel top and bottom which allowed the Meson East beamline, target box and SM0 magnetic volume to be kept in a vacuum of 10^{-6} *Torr*. A thin, 250 *micron*, stainless steel window on the downstream end of the SM0 insert separated the vacuum from a small air gap and the SM12 aperture. SM0 was operated at 2000 *Amps* for a net $p_\perp$ kick of about 1.3 *Gev/c* during the 400 *Gev/c* run only.

About 10 *cm* from the SM0 downstream window was a 76 *micron* mylar window on the upstream end of the SM12 magnet. A

[22] Magnet and Targets Handbook - User's Handbook, Argonne National Laboratory, page 5.9, (30 March 1966)

similar window on the downstream end of SM12 allowed the magnet volume to be filled with helium to reduce multiple scattering.

The SM12 magnet yoke was 14.1 *m* long, 2.7 *m* wide, 5.2 *m* high. The upstream face of the SM12 yoke was defined to be Z = 0. in the E605 coordinate system (the positive Z direction pointed downstream). A transverse momentum kick of about 7.5 *Gev/c* was achieved with a current of 4000 *Amps*. The useful volume of this magnet was tapered horizontally from 15.24 *cm* at the upstream end to 61.0 *cm* at the downstream end with seven iron poleface modules. The second and third modules from the upstream end held a 4.57 *m* long copper beam dump that blocked the horizontal aperture and caught the primary beam and low vertical angle secondaries produced in the target. The dump was tapered vertically from Y= $\pm$ 12.7 *cm* at Z $\approx$ 1.73 *m* to Y = $\pm$ 15.2 *cm* at Z $\approx$ 2.64 *m* and remained at that height until it ended at Z $\approx$ 6.30 *m*. Each module held thick lead and tungsten baffles on the upper and lower surfaces of the SM12 aperture to intercept photons from the target and contain as much as possible of their electromagnetic showers. In addition a tungsten collimator was mounted on the upstream end of SM12. This collimator intercepted low vertical angle photons produced in the target but did not intercept the primary beam. The collimator and lead–tungsten baffles were arranged so that no neutral particles from the target directly struck the spectrometer detectors, while high $p_\perp$ charged particles were focussed onto the detector.

The third spectrometer magnet, SM3, was located between detector stations 1 and 2 and contained a polyethylene bag filled with helium. The gap in the yoke of this magnet was tapered from 1.35 m at the upstream end to 1.5 m at the downstream end. It is 3.23 m long and 1.68 m high. Iron flux return plates 5 cm thick were mounted on both ends to reduce the fringe field at the nearby detector stations. A running current of 4200 $Amps$ gave a $p_\perp$ kick of about .9 Gev/c. This third magnet allowed measurement of particle momentum to about $\pm$ 1.0 % and facilitated differentiation of target and non-target tracks emanating from the first two magnets.

The magnetic field of each magnet was mapped with the ZIPTRACK system in use at Fermilab. The ZIPTRACK was a long hollow aluminum beam which contained three mutually perpendicular coils that measured the change in flux as the coils moved through the magnetic field. The absolute magnitude of the ZIPTRACK measurements was determined by nuclear magnetic resonance probe measurements. The current in each magnet was monitored by the beamline control system and recorded on magnetic tape for each spill. The observed variation in current in all magnets was about $\pm$ 1 Amp.

II. D. Hodoscopes

Each of the four detector stations had vertically-segmented ("Y") hodoscopes and horizontally-segmented ("X") hodoscopes ex-

cept for station 2 which had only Y hodoscopes. The timing of the hodoscope signals at the trigger logic inputs was carefully adjusted to discriminate between particles produced in neighboring RF buckets. The following table lists the scintillation hodoscope specifications.

Table 2: Hodoscope Specifications

Plane	Number of counters X × Y	Aperture width x (cm)	Aperture width y (cm)	Z-position (m)	Counter width (cm)
Y1	2 × 12	121.9	152.4	20.47	12.70
X1	12 × 2	121.9	152.4	20.51	10.16
Y2	2 × 17	162.6	172.7	28.32	10.16
X3	13 × 2	264.2	233.7	46.66	22.01 [11.03]*
Y3	2 × 13	264.2	233.7	46.92	17.78 [19.05]*
Y4	2 × 14	294.6	254.0	51.70	17.78
X4	16 × 2	320.0	289.6	54.13	12.90

* [end counters only]

II. E. Wire Chambers

Three types of wire chambers provided tracking information at each station.

Station 1 had six multiwire proportional chambers(MWPC) in 3 different views: U, Y and V. U and V wires are inclined at angle $\Theta = \pm \arctan(1/4)$ with respect to the Y wires. The wire spacing of the Y(U and V) wires was 2.0 mm(1.94 mm). The MWPC specifications follow:

Table 3: Multiwire Proportional Chamber Specifications

Plane	Number of wires	Aperture width x (cm)	Aperture width y (cm)	Z-position (m)
U1A	896	128.27	151.38	18.97
Y1A	736	128.27	149.56	19.22
V1A	896	128.27	151.38	19.48
U1B	896	128.27	151.38	19.73
Y1B	736	128.27	149.56	19.96
V1B	896	128.27	151.38	20.23

Stations 2 and 3 each had three sets of paired drift chambers — one for each view, Y,U and V. Each chamber pair had one set of wires staggered by half the sense wire spacing to resolve the drift time ambiguity. The spacing of the sense wires was 10.0 mm(9.7 mm) and 20.0 mm(19.4 mm) in the Y(U and V) chambers in Stations 2 and 3, respectively. A spatial resolution of about 225 *microns* was achieved for each drift chamber. Further details are given in the next table.

Table 4: Drift Chamber Specifications

Plane	Number of wires	Aperture width x (cm)	Aperture width y (cm)	Z-position (m)
U2	208	167.64	182.88	27.52
U2′	208	167.64	182.88	27.58
Y2	176	167.64	178.82	27.76
Y2′	176	167.64	178.82	27.82
V2	208	167.64	182.88	28.03
V2′	208	167.64	182.88	28.08
U3	144	296.24	242.57	45.76
U3′	144	296.24	242.57	45.80
Y3	112	296.24	233.27	46.01
Y3′	112	296.24	233.27	46.08
V3	144	296.24	242.57	46.26
V3′	144	296.24	242.57	46.33

Three proportional tube planes, 2 Y planes and 1 X plane, were used in Station 4 to aid in muon identification. The wire spacing was 2.54 cm and each cell was a square 2.54 $\times$ 2.54 cm^2 extruded aluminum tube. Each plane had two layers of cells staggered by half the cell size to avoid dead regions.

Figure 5 shows an exploded view of the detector emphasizing the wire chambers and hodoscopes of the first three stations.

II. F. Ring-Imaging Čerenkov Detector

Between Stations 2 and 3, a 15 m long aluminum vessel filled with high-purity helium gas[23] served as the radiator for the ring-imaging Čerenkov detector. The development and operation of the detector are described in detail elsewhere.[24] Briefly, high momentum particles passing through the helium radiated Čerenkov photons that struck one of sixteen spherical mirror segments to be focussed on the two photon detectors located on each side of the radiator. For the majority of the data taking, an average of about 2.25 photons per ($\beta \approx 1$)particle was detected.

[23] See Appendix A.

[24] R. Bouclier et al, Nucl. Inst. & Methods 205, 403 (1983); Ph. Mangeot et al, Nucl. Inst. & Methods 216, 79 (1983); M. Adams et al, Nucl. Inst. & Methods 217, 237 (1083); G. Coutrakon, Ph.D. thesis, S.U.N.Y. at Stony Brook (1982); H.D. Glass, Ph.D. thesis, S.U.N.Y. at Stony Brook (1985).

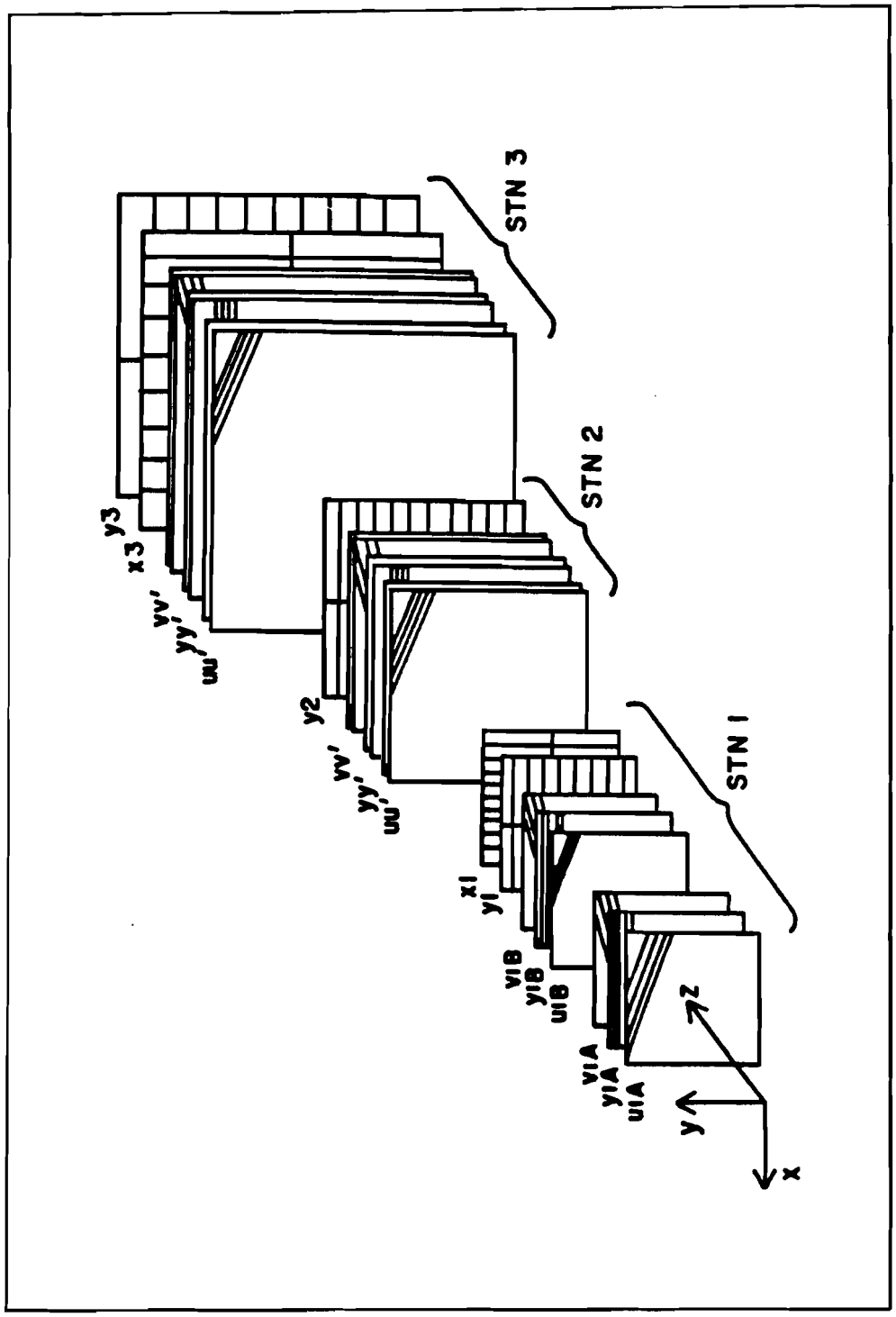

Figure 5. Wire Chambers and Hodoscopes of Stations 1, 2 and 3

II. G. Calorimeter

The electromagnetic and hadron calorimeters placed behind Station 3 served two functions:

1) To provide fast electron and hadron trigger signals and,

2) to aid in off-line particle identification.

The design, construction and calibration of the calorimeter has been described elsewhere.[25] Basically, the electromagnetic and hadronic calorimeters were sampling calorimeters consisting of plastic scintillators and dense absorbers with a total of 9 absorption lengths. The timing and gain balancing of the calorimeter phototubes were monitored with a laser-fibre optics system during the course of the data taking. The precise gains of each phototube were determined off-line, accounting for attenuation in the scintillator and energy sharing between the different modules. The energy resolution of the hadron calorimeter was found to be $\sigma_E/E \approx 1.1/\sqrt{(E(Gev))}$.

[25] J.A. Crittenden *et al.*, Phys. Rev. D 34, 2584 (1986) and references therein.

III. Trigger

Although many different triggers were employed to investigate different kinds of reaction products, only the 'hadron' triggers will be discussed here. The hadron triggers relied on a coincidence between the hodoscope and calorimeter signals.

III. A. Hodoscopes and Trigger Matrices

All hodoscope signals were fed into 16-channel Lecroy 4416 discriminators; the discriminator outputs were fed, in turn, into gated pulse stretchers.[26] The pulse stretchers were gated by the accelerator RF timing signal and thus synchronized the trigger timing to a single RF bunch even though individual hodoscope signals exhibited 'jitter' due to differences in signal propagation in the scintillators or phototubes. The pulse stretchers produced two sets of 16 outputs, one was sent to coincidence registers while the other set was fed into trigger matrix modules.

The trigger matrices were designed to produce an output when certain preset hodoscope hit patterns in the module's random access memory were satisfied.[27] For 'hadron' triggers, four types of 3 - fold

[26] R. Gray and J.P. Rutherfoord, Nucl. Inst. & Methods, A244, 440 (1986)
[27] H.D. Glass, Ph.D. thesis.

coincidences between hodoscopes in Y1, Y2 and Y3 were selected: YUL, YUR, YDL, YDR, where "U" and "D" specify selection of tracks from the target above and below the beam dump in the SM12 magnet, and "L" and "R" denote the left($X > 0$) and right($X < 0$) sides of the apparatus. Four types of coincidences of the four trigger matrices were created:

1) $Y \equiv YUL \vee YUR \vee YDL \vee YDR$,[28]

2) $2Y \equiv$ at least 2 out of 4 (YUL, YUR, YDL, YDR),

3) $YU \equiv YUL \vee YUR$,

4) $YD \equiv YDL \vee YDR$.

The pulse stretcher outputs were also fed into terminator modules which provided a logical "OR" of each set of up to 16 inputs corresponding to either the left or right half of a single hodoscope plane. In this way, the coincidences "3/4L" and "3/4R" were formed; "3/4" refers to a requirement of a hit in at least 3 out of the 4 hodoscope planes: X1, Y2, X3 and Y3.

[28] A "OR" B is denoted by $A \vee B$

III. B. Calorimeter

Dynode signals from the calorimeter phototubes were summed with linear fan-ins for each longitudinal module in both the electromagnetic ("e") and hadron ("H") calorimeter. The signals were summed as shown to produce two sorts of summed signals for each side:[29]

1) EUR = H1R(j–13) + H2R(j–13) + [eiR(5–12), $i = 1,2,3,4,$]

2) EDR = H1R(1–k) + H2R(1–k) + [eiR(1–8), $i = 1,2,3,4,$]

   where j = 5(6) and k = 9(8) for the 400(800) *Gev/c* data,

3) ER = Sum of all modules in H1R, H2R, eiR, $i = 1,2,3,4$.

(EUL, EDL and EL were formed in a similar fashion).

Figure 6 shows how these signals were combined with the hodoscope combinations described previously to form the hadron triggers.

[29] Calorimeter nomenclature: "H2L7" = Hadron calorimeter, 2nd layer, Left side, counter number 7.

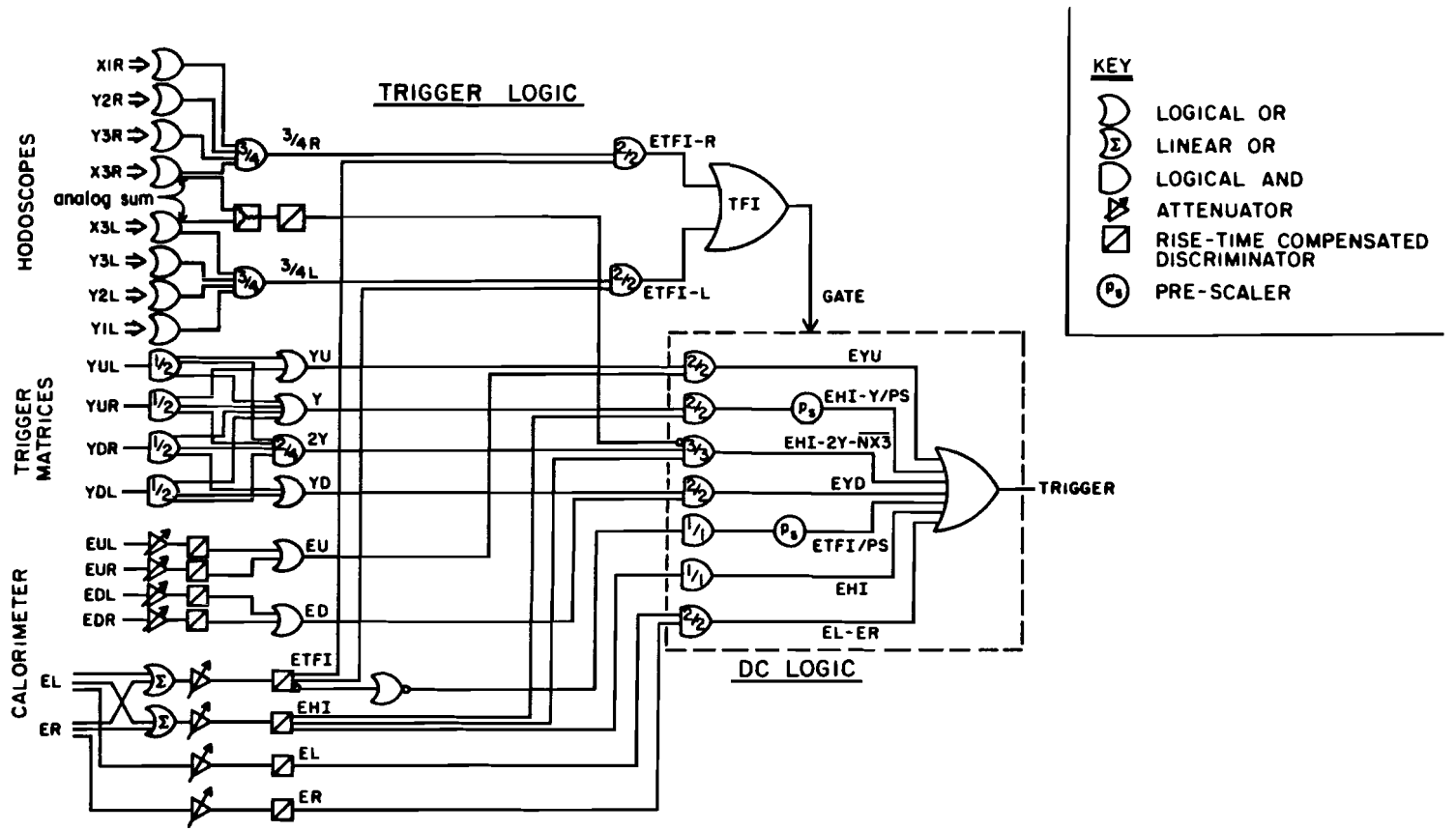

Figure 6. Trigger Logic

IV. Data Reduction

IV. A. Trigger Selection

Only certain triggers were selected for analysis. For the 400(800) *Gev/c* running, EYU, EYD and EHI(EYU, EYD, EHI∧Y/PS, and EL∧ER) were chosen in addition to the low threshold calorimeter trigger, ETFI/PS.[30]

IV. B. Tracking

The following algorithm — with the modifications noted in the next two sections — was used to find and fit the trajectories of charged tracks in the wire chambers:

1) In each drift chamber station 'triplets' and 'doublets' of wires were formed. A 'triplet' of over-lapping wires contained at least one wire in each view (U,V and Y) with at least one correlated pair[31] of hits in one view. A 'doublet' was defined to be four overlapping wires, a correlated pair in each of two views, not

[30] ∧ = "AND" and /PS = pre-scaled.

[31] For example, if the sum of the drift times of a hit on a Y2 wire and a hit on an adjacent Y2' wire were consistent with a trajectory with a Y-angle relative to the Z-axis of less than 70 *mrad* then the pair of hits was 'correlated'.

contained in the list of triplets.

2) 'Drift chamber tracks' were selected from the doublets and triplets at stations 2 and 3. Each doublet or triplet at station 2 was checked with each doublet or triplet at station 3 to see if their positions were consistent with a straight line pointing to the SM3 aperture.

3) A list of 'wire chamber tracks' was formed with the wire hits in the station 1 MWPC's and the drift chamber tracks using a single bend plane approximation for the SM3 magnetic field.

4) Each accepted track required at least 4 out of 6 hits in each drift chamber station and at least 3 out of 6 hits in station 1.

IV. C. Masking

To reduce the processing time and increase the ability to find target tracks, the lists of wire hits were initially 'masked' with the calorimeter or Y2 hodoscopes. A 'mask' is defined to be an allowed range of X or Y coordinates at a wire chamber Z-position. The size and centroid of isolated energy clusters in the electromagnetic and hadron calorimeter supplied the masking dimensions at station 3. Possible trajectories were projected from the calorimeter cluster centroids to the Y2 hodoscopes to define the masks at station 2.

IV. D. Target Trajectory Selection

For a station 2 spatial coordinate defined by a doublet or triplet, only a small range of station 3 spatial positions was consistent with a particle trajectory originating in the target for a given set of SM0, SM12 and SM3 magnet currents. This information was employed to eliminate some station 2 – station 3 wire hit combinations from consideration as a drift chamber track. In addition, each drift chamber track incorporates sets of wire hits that were consistent with a select range of signed particle momenta. Thus, the possible MWPC hits that needed to be considered at station 1 were restricted.

Careful studies of the effects of masking and target trajectory selection showed that no target tracks were eliminated when these techniques were incorporated into the tracking algorithm.

IV. E. Particle Identification

The requirements for a reconstructed track to be considered a hadron were

1) at least 6 % of the total energy in the calorimeter in the hadron part,

2) the energy deposited in the calorimeter matched the reconstructed track momentum to within 3.0 standard deviations of the calorimeter energy resolution, see Figure 7, and

3) less than 4 out of 5 hits in the station 4 detector elements (X4, Y4 hodoscopes and PTY, PTX, PTY′ proportional tubes).

The first requirement rejected electrons. Approximately .2 % of the hadron trigger data was rejected by this cut. The electron identification efficiency was estimated to be at least 95%;[32] thus, electron contamination of the hadron triggers was,at most, a negligible .01%. Tracks incorrectly associated with calorimeter energy deposits were rejected by the second criterion. A cut of ±3.0 standard deviations eliminated .3% of the tracks. A correction was applied to account for the data lost by these two cuts. The third criterion rejected muons that deposited appreciable energy in the calorimeter. Muon contamination was calculated to be at most .02%,[33] which is negligible. Rejection of hadrons by the last cut was also negligible — less than .03% of well-identified kaons and protons failed.

IV. F. Traceback

A grid, with approximately 2.5 *cm* spacing, of the X-component of the magnetic field in the SM0 and SM12 magnets was made from the ZIPTRACK measurements. The particle trajectory at the SM3 bend plane was stepped upstream through this grid using the momentum determined by the tracking algorithm. If the resulting trajectory was within 7.5 *cm* of the X and Y position of the target

[32] Y. Sakai, Ph.D. Thesis, Kyoto University (1984).
[33] *Ibid.*

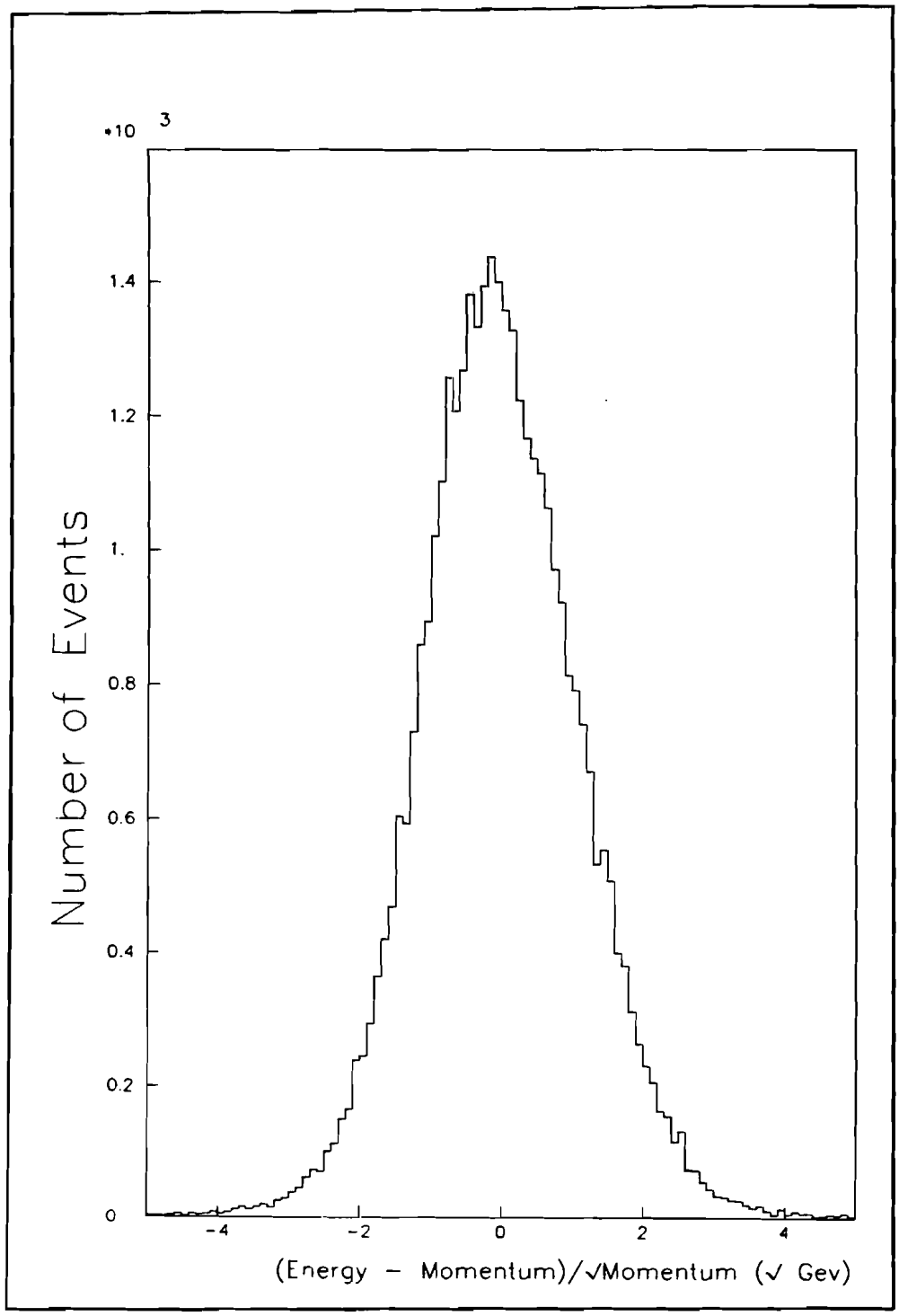

Figure 7. Calorimeter Energy Resolution

center at the nominal Z-position (Z = -3.302 m), and the trajectory passed loose position cuts at the downstream end of the tungsten collimator, the edge of the dump taper, the downstream end of the dump and the most downstream lead-tungsten baffle in the SM12 magnet, then the trajectory was treated as a potential target track. Each potential target track was re-traced using the momentum determined by the previous traceback with the constraint that the track came from the nominal target center in Z. The process was repeated until the Y-target position was within ± .25 mm of the nominal target center in Y. Typically, three or four iterations sufficed.

IV. F. 1. Momentum Resolution

The same traceback algorithm was used to reconstruct high mass dimuon data taken concurrently with a Be target that was .5 mm thick in the Y-dimension.[34] A fit to the resulting mass spectrum yielded a mass resolution of 25 Mev/c^2 for the upsilon as shown in Figure 8.

The resolution in $p_\perp$ for single hadrons from the 20 cm long liquid target is somewhat worse than the unlike-sign pair mass resolution. According to hand calculations using trajectories in the $X = 0$ plane, the main contributions to $p_\perp$ measurement inaccuracy are the target length and beam divergence as shown in Figure 9.

[34] R. Gray, Ph.D. thesis, University of Washington, 1987.

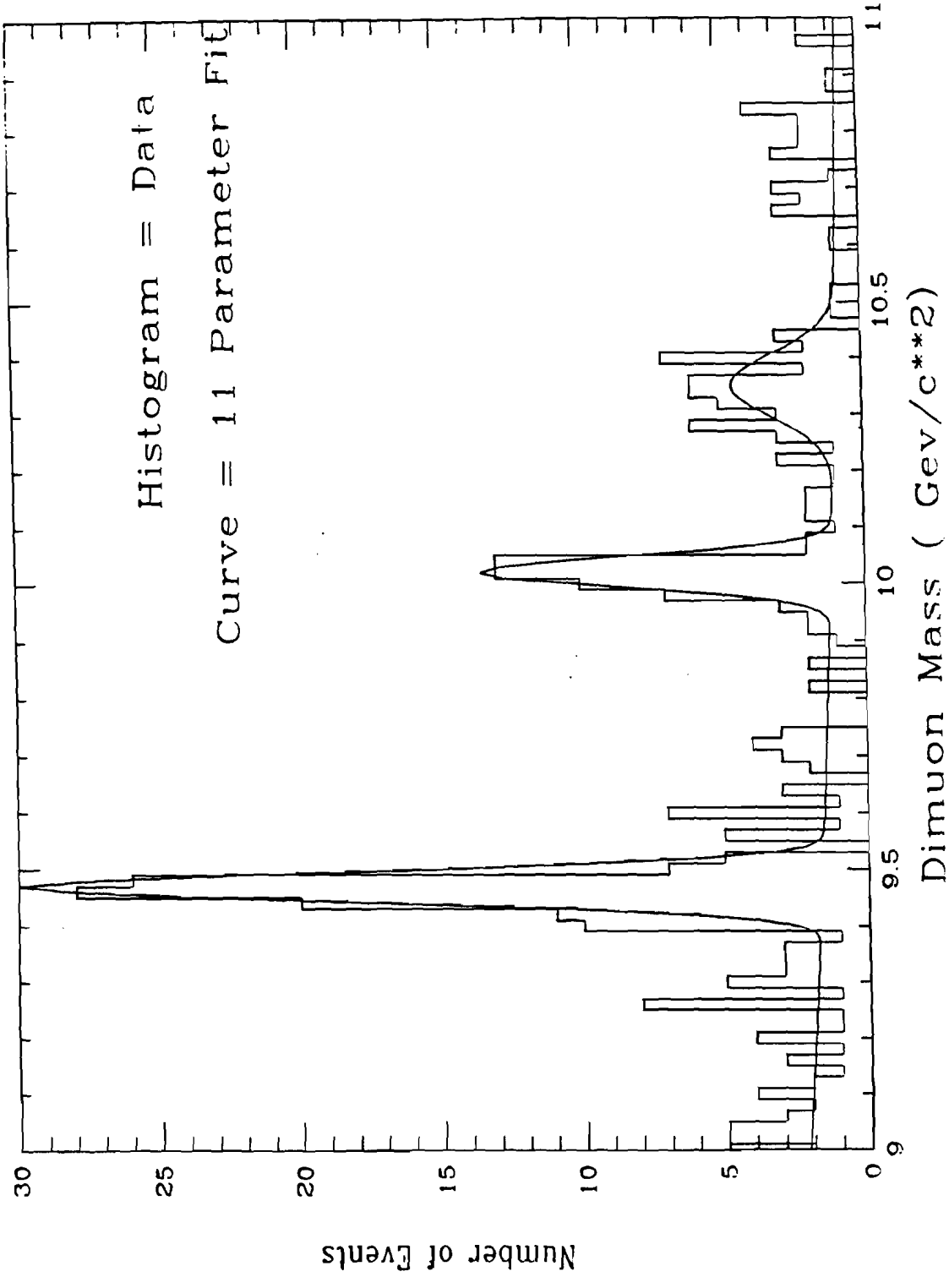

Figure 8. Dimuon mass spectrum

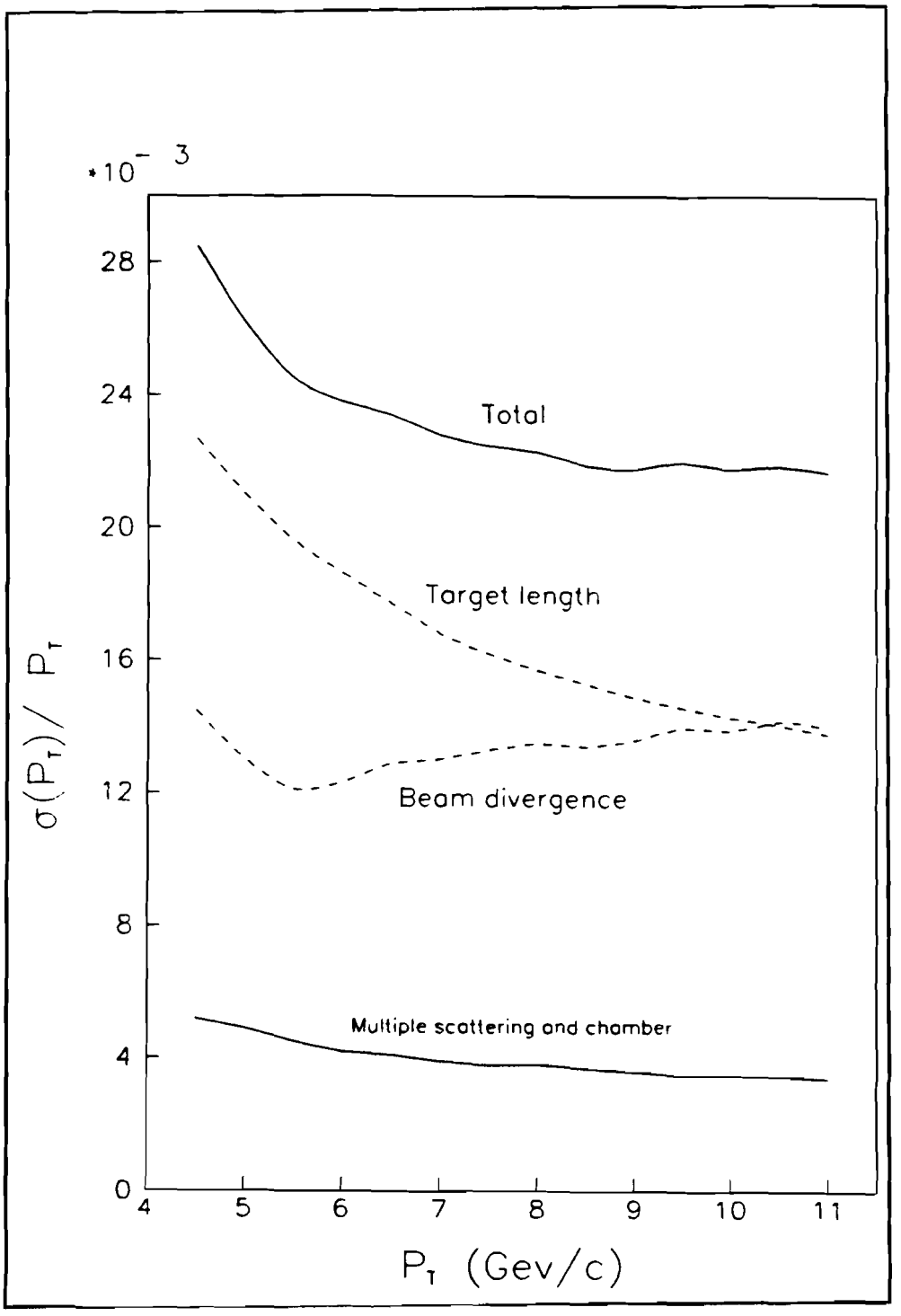

Figure 9. Calculated transverse momentum resolution

IV. F. 2. Target Track Cuts

The final set of 'target tracks' was selected by a series of cuts on the trajectory and target X and Y coordinates of each track. Two cuts were made on the final trajectory inside the SM0-SM12 magnets.

One cut was made on the Y position at the downstream end of the tungsten collimator mounted on the front of the SM12 magnet yoke. The Y-position of this aperture point was determined using high mass electron pair data[35] as shown in Figure 10. Electrons provide an accurate guide to locate the collimator, because the tungsten collimator effectively absorbs all electrons that strike it. This criterion set the minimum angle acceptance and removed most of the tertiary hadrons that interacted in the dump or collimator.

[35] T. Yoshida, Ph.D. thesis, Kyoto University, 1986.

The second cut was made on the Y position of the track at the last lead-tungsten baffle in the SM12 magnet. This cut tracks that emerged from the roof or floor of the SM12 magnet.

These cuts were made two standard deviations (according to the resolution of the traceback) wider than the determined aperture points. Increasing these cuts to five standard deviations did not significantly change the measured cross sections or particle fractions.

Even with these trajectory cuts, some background events remained in the final target distribution. Each distribution was fitted with a gaussian plus third order polynomial to ascertain the relative signal to background rate. Figure 11 shows the results of one such fit. The background contributions based on a 4(3) standard deviation cut for the 800(400) *Gev* data are shown in Table 5.

Table 5: Background Fraction at Target

Data set	Negative particles	Positive particles
800 *Gev pp*	$.041 \pm .003$	$.038 \pm .002$
400 *Gev pp* (norm)	$.071 \pm .018$	$.074 \pm .009$
400 *Gev pp* (rev)	$.096 \pm .024$	$.096 \pm .024$
400 *Gev pd*	$.033 \pm .004$	$.104 \pm .006$

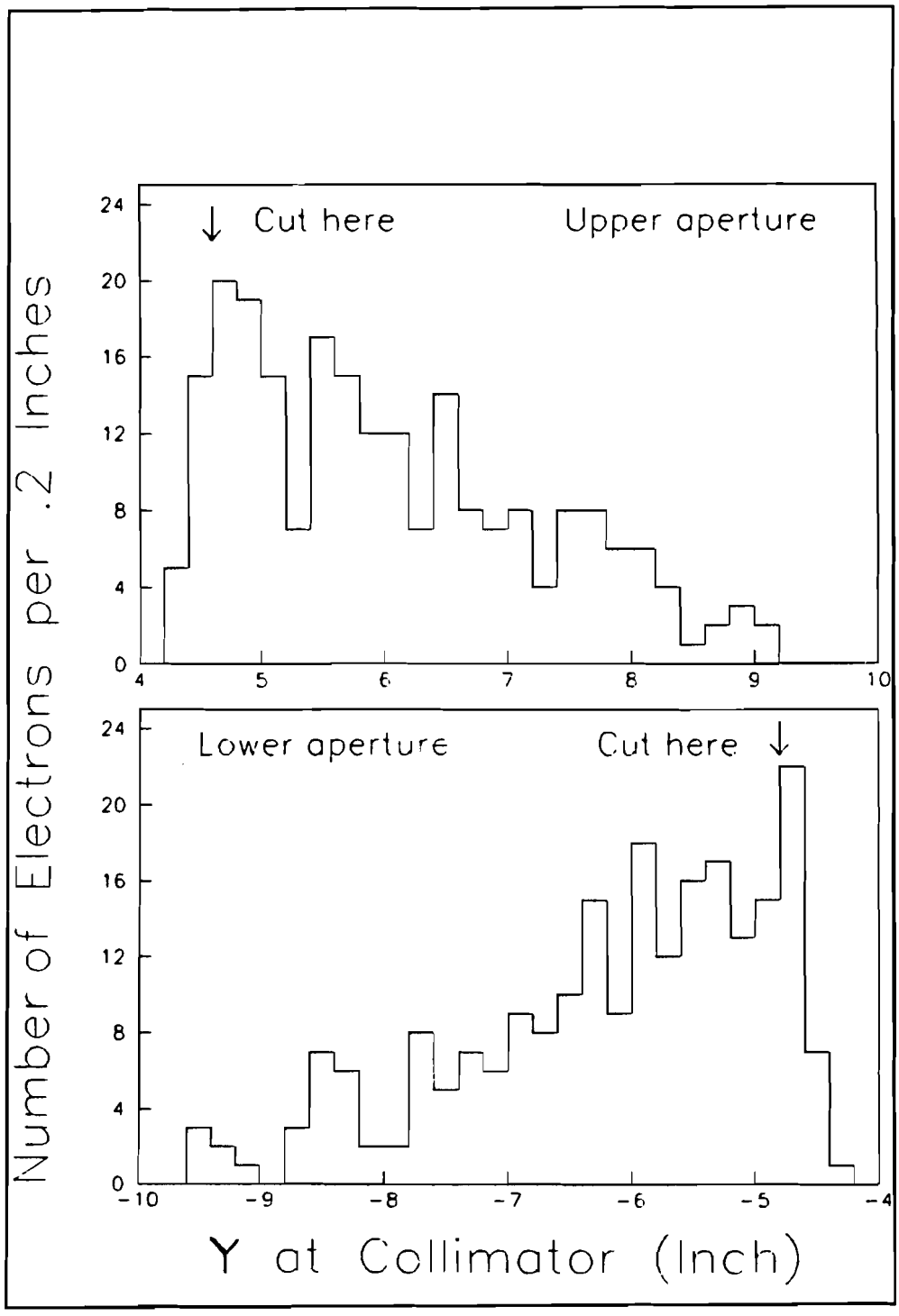

Figure 10. Dielectron Y-position at the Collimator

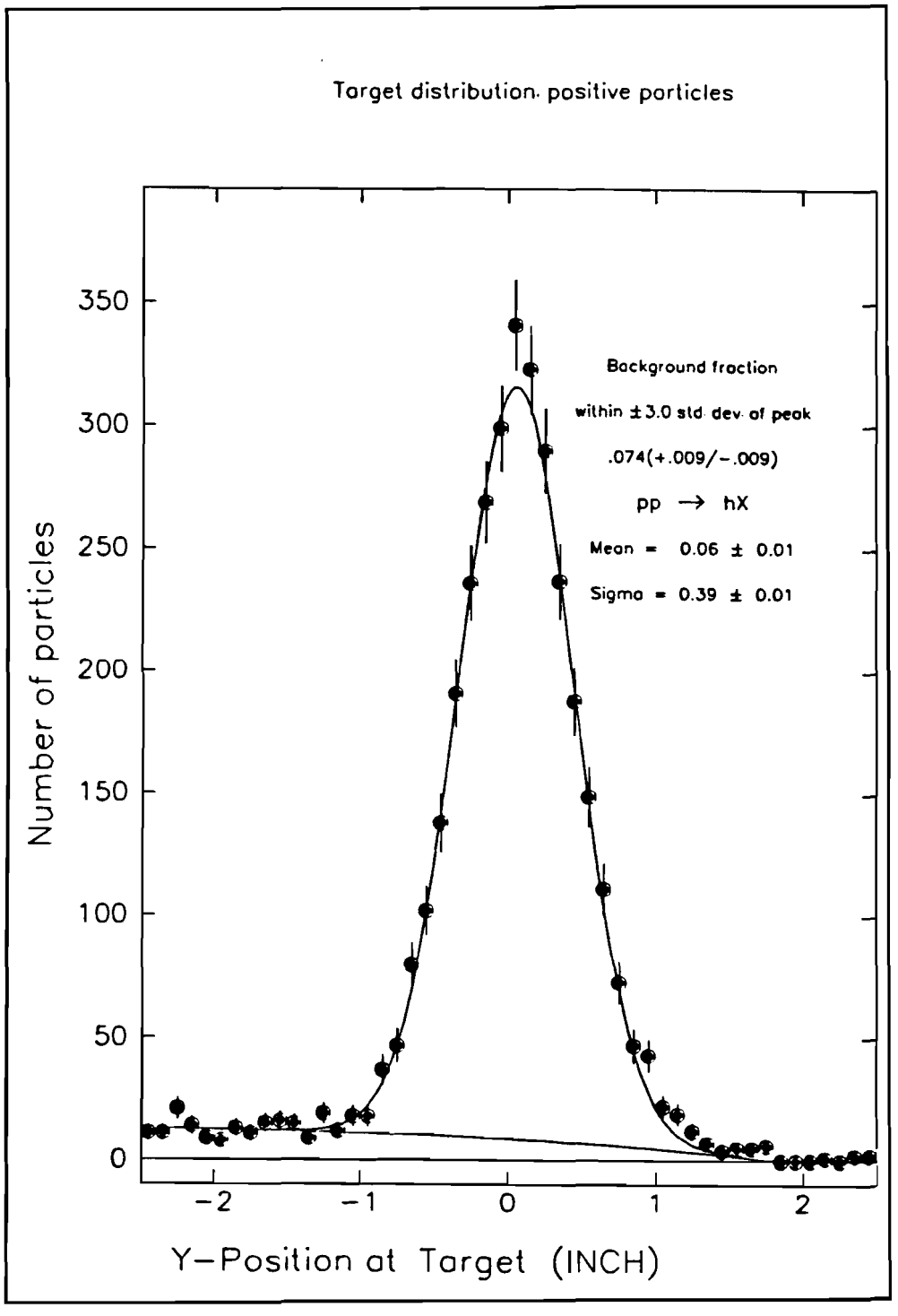

Figure 11. Y-target distribution and fit

The next two tables show the details of the number of events passing each stage of analysis for the different data sets. In Table 6 the "doublets and triplets" cut refers to the requirement of at least one triplet or two doublets at each drift chamber(DC) station. The two "Y_{coll}" cuts are for tracks above and below the beam dump, respectively.

Table 6: Number of Events Passing Analysis Cuts

Cut	800 *Gev/c pp*	400 *Gev/c pp*	400 *Gev/c pd*
Total events	4896608	1508335	2617182
Event length	4871537	1508169	2606190
Trigger format	4871478	1507732	2594723
Select trigger	1931054	1073053	1980033
Event format	1930863	1067334	1958055
Doublets and triplets	1854962	851412	1749522
Triplet bank length	1852820	849283	1746548
≥ 1 DC track	450234	418102	1001820
≥ 1 track	204407	308099	574664
≥ 1 target track	39420	15559	27468

Table 7: Number of Tracks Passing Fiducial Cuts

Cut	Full	Empty	Full	Empty
	400 *Gev/c pp* Magnets reversed		400 *Gev/c pp* Magnets normal	
	3409	44	11702	404
$\|Y\| < 114.3$ *cm* at Stn. 3	2999	38	10389	366
$.002 < \|\Theta_X\| < .023$ *mrad*	2579	31	8624	293
$Y_{coll} > 11.684$ *cm*	2438	31	6920	225
$Y_{coll} < -12.192$ *cm*	1716	26	5927	178
$Y_{target} < 3\sigma$	1449	20	5136	145
≥ 4 hodoscopes	1442	20	5126	145
Hadron identification	1410	18	5053	140
≥ 3 chambers at Stn. 1	1377	16	4489	131
	400 *Gev/c pd*		800 *Gev/c pp*	
	27170	298	38103	1317
$\|Y\| < 114.3$ *cm* at Stn. 3	24540	284	35632	1250
$.002 < \|\Theta_X\| < .023$ *mrad*	20854	221	31046	1074
$Y_{coll} > 11.684$ *cm*	17495	171	28349	983
$Y_{coll} < -12.192$ *cm*	13838	121	20542	723
$Y_{target} < 3\sigma$	11665	97	19927	698
≥ 4 hodoscopes	11408	95	19731	696
Hadron identification	11162	91	19670	689
≥ 3 chambers at Stn. 1	10557	89	19670	689

IV. G. Spill Cuts

Each spill was subjected to three criteria to insure 100% targeting and high detector efficiency:

1) During periods of accelerator start-up, the incident proton beam stability was frequently poor and the beam intensity low. A minimum beam intensity cut eliminated these spills.

2) The accidental coincidence rate between two uncorrelated hodoscope counters (R_{12}) is expected to be proportional to the square of the beam-target interaction rate[36] measured by AMON.[37] If the structure of a spill has large bucket-to-bucket variations, R_{12} will be proportional to AMON^n, where $n > 2$, due to increased rates in intense buckets. Such spills were removed by setting limits on R_{12}/AMON as a function of AMON as shown in Figure 12.

3) Cuts on the ratio of AMON to SEM removed spills with inadequate targeting due to incorrect beam position at the target.

IV. H. Hadron Identification

For each event with at least one target track, Čerenkov hadron species identification was attempted. Predicted Čerenkov ring centers

[36] H. Jöstlein et al., Phys. Rev. D20, 53 (1979)
[37] AMON is described in Section V. B.

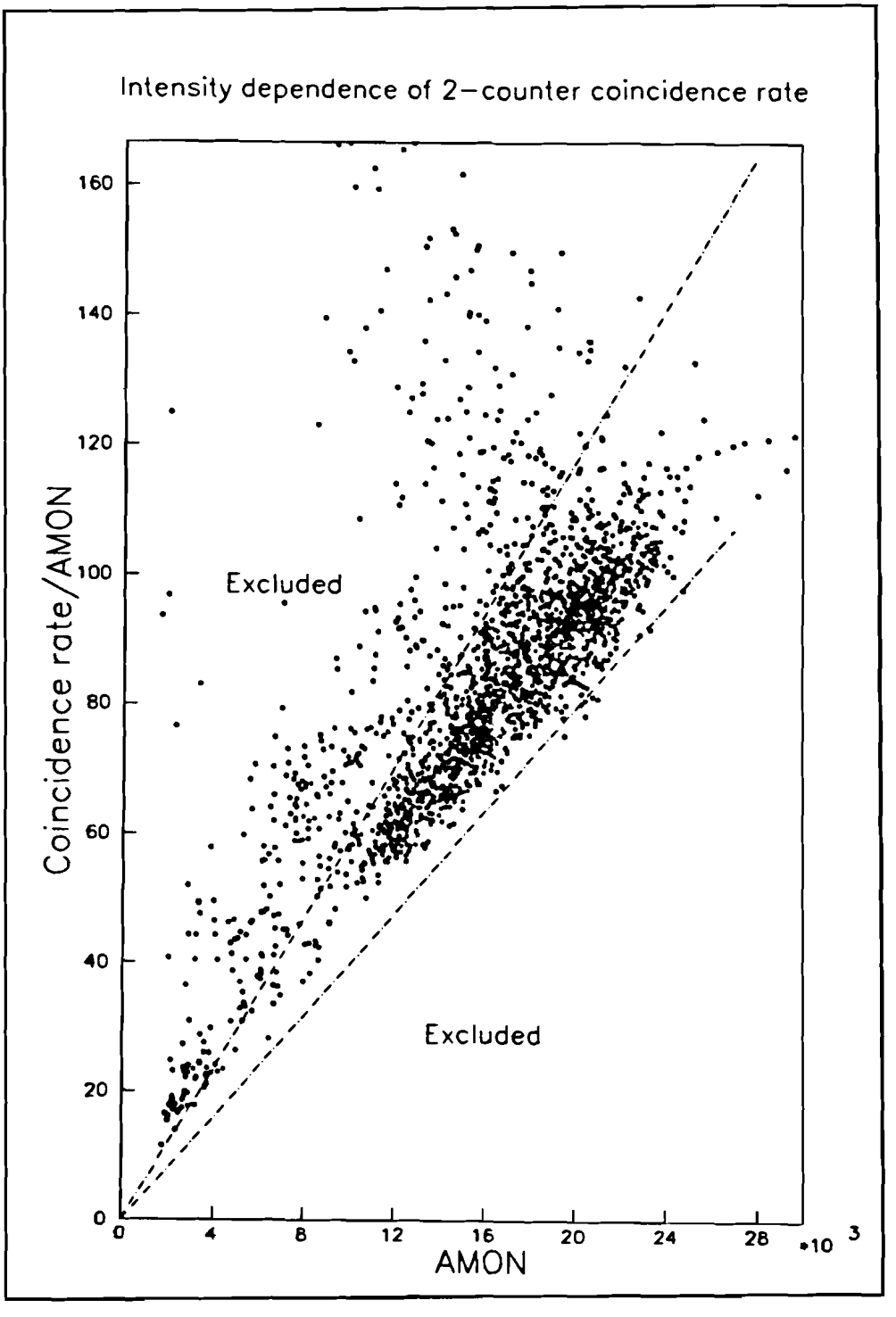

Figure 12. Accidental coincidence rate R_{12}/AMON *vs.* AMON

were computed by reflecting each particle trajectory from every mirror that could have intercepted a photon to the appropriate detector.

Photon-produced clusters in each view(U, V and X) of each Čerenkov photon detector were defined as groups of wires with pulse heights greater than a selected threshold. The coordinate for each cluster was calculated by the center of gravity method.

The radius of each photon was calculated as the distance from the predicted ring center to the photon. Each photon was then corrected for spherical aberration — the distortion of the circular ring image into an oval shape — using the known mirror angles and photon detection angle. Other factors that contributed to the radius resolution were

1) chromatic dispersion due to the variation in the index of refraction of the radiator gas over the range of detectable photon energy,
2) the lack of knowledge of the Z-location of photon emission,
3) momentum resolution of the spectrometer,
4) mirror position uncertainty, and
5) the position resolution of the photon detection chamber.

The uncertainty in the photon radius caused by these effects was accounted for on a photon–by–photon basis in the species identification algorithm.

The purpose of the species identification algorithm, described

in detail in Appendix D,[38] was to provide the relative probability, f^{α}, that each track was an $\alpha = \pi, K$ or p assuming equal incident fluxes of each species. In determining f^{α} a number of different factors were taken into account:

1) the particle velocity, β^{α}, since the number of Čerenkov photons is proportional to the Čerenkov angle — $\sin^2\theta_{\check{C}} = 1-(1/n\beta)^2$, n = index of refraction,

2) the ring radius, because the detector resolution of individual photons decreases as the radius decreases (nearby photons can become merged),

3) the probability that the detector was inefficient for a given event due to sparking of the Čerenkov photon detector, and

4) the possibility that non-Čerenkov photons are detected.

For events with two tracks a similar relative probability, $f^{\alpha\gamma}$ was determined taking into account the additional complication of the photons from both tracks striking the same detector.

[38] also see P.B. Straub, Ph.D. Thesis, University of Washington, in preparation.

V. Cross Section Calculations

V. A. Definition of Statistical and Systematic Uncertainty

Throughout this dissertation the *statistical* uncertainty of N events was estimated by assuming Poisson statistics so that one standard deviation error in N was $\sqrt{N}$. The *systematic* uncertainty in a quantity x arose from two possible sources:

1) If x was a function of terms, n_i (a number of events), then the *systematic* error in x was derived by propagation of the individual *statistical* errors $\sqrt{n_i}$.

2) If the determination of x was based on an algorithm containing adjustable parameters, a_i, then the *systematic* uncertainty in x was estimated by judicious variation of the a_i. The magnitude of this type of systematic uncertainty was estimated as representing a single standard deviation in the measured quantity *as if* the source of systematic uncertainty followed Poisson statistics.

For example the tracking efficiency for a given track was determined using the tracking algorithm (see Section IV. B–D) and the measured wire chamber efficiencies (see Appendix B). Thus the

statistical uncertainty in each wire chamber efficiency measurement was the source of *systematic* uncertainty as outlined in 1) above, while the *systematic* error of type 2) was determined by varying the size of the masks at stations 2 and 3.

V. B. Single Hadron Cross Section

In any frame one can express the single hadron cross section in terms of the integrated luminosity and number of events:

$$N_i = LA_i \int_{\Omega_i} (E\frac{d^3\sigma}{dp^3})\ \frac{d^3p}{E}$$

where,

i denotes a bin in the 3-momentum($\vec{p}$),

Ω_i denotes the volume of the i^{th} bin,

L $\equiv$ integrated luminosity per nucleus,

N_i $\equiv$ number of particles produced into the i^{th} bin,

$E\frac{d^3\sigma}{dp^3}$ $\equiv$ inclusive single particle, Lorentz invariant cross section per nucleus,

E = energy,

d^3p = volume element in momentum space, and

A_i = geometrical acceptance for the i^{th} bin determined by a monte carlo with the same magnetic field map and aperture cuts used in the data analysis. A_i is defined as the fraction of particles

produced in a given bin whose trajectories pass through the experimental aperture. Figures 13-16 show the computed monte carlo acceptance as a function of transverse momentum for each aperture and beam momentum. The horizontal error bars show the bin width.

If $\left\langle E\frac{d^3\sigma}{dp^3}_i \right\rangle$ denotes the average of the invariant cross section in the i^{th} bin, defined by

$$\left\langle E\frac{d^3\sigma}{dp^3}_i \right\rangle \equiv \int_{\Omega_i} (E\frac{d^3\sigma}{dp^3})\ \frac{d^3p}{E} \Big/ \int_{\Omega_i} d^3p/E.$$

then

$$\left\langle E\frac{d^3\sigma}{dp^3}_i \right\rangle = \frac{N_i}{LA_i} \Big/ \int_{\Omega_i} d^3p/E.$$

The integral in the denominator can be calculated analytically since the limits of the bin are known by definition. The quantity N_i/L is given by (neglecting corrections for target vessel effects)

$$\frac{N_i}{L} = \frac{\left(\sum_j^{spills} \sum_k^{n_j} w^i_{k,t}\right)}{\left(\sum_j^{spills} \mathcal{L}_j \times l_j\right)}$$

where

$\mathcal{L}_j \equiv$ integrated luminosity of spill j,

$l_j \equiv$ live-time fraction for spill j,

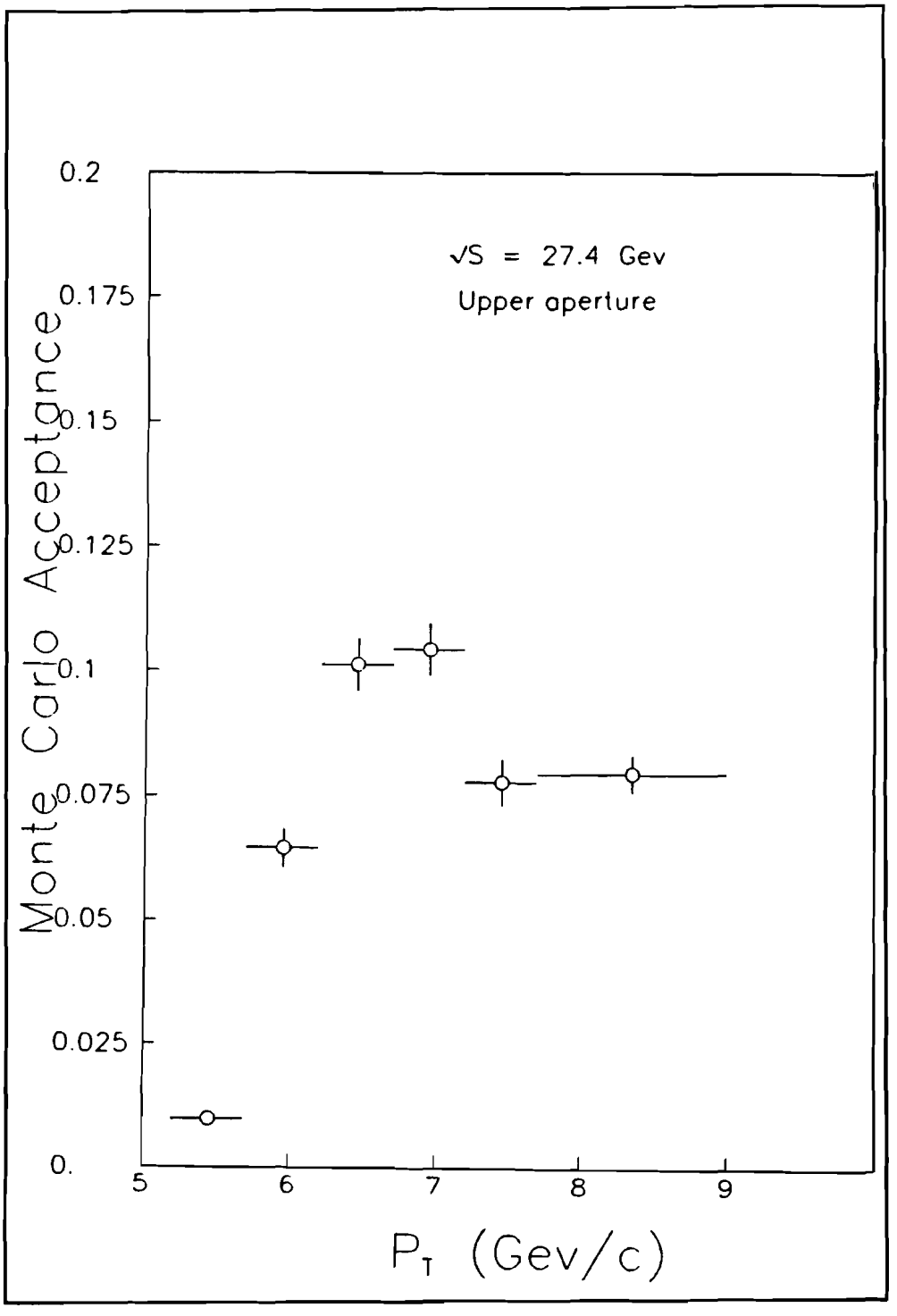

Figure 13. Monte carlo acceptance, 400 *Gev/c*, upper aperture

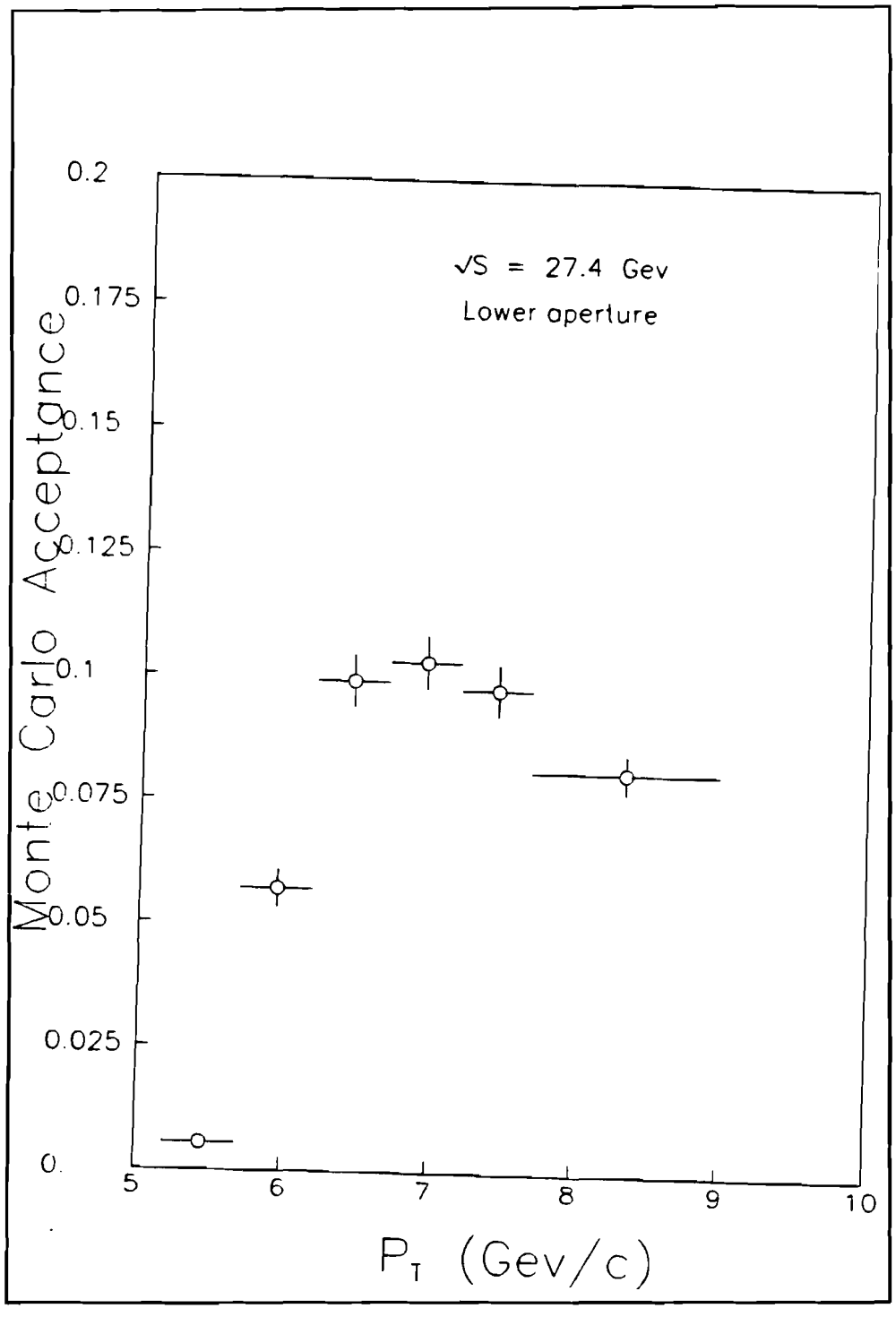

Figure 14. Monte carlo acceptance, 400 *Gev/c*, lower aperture

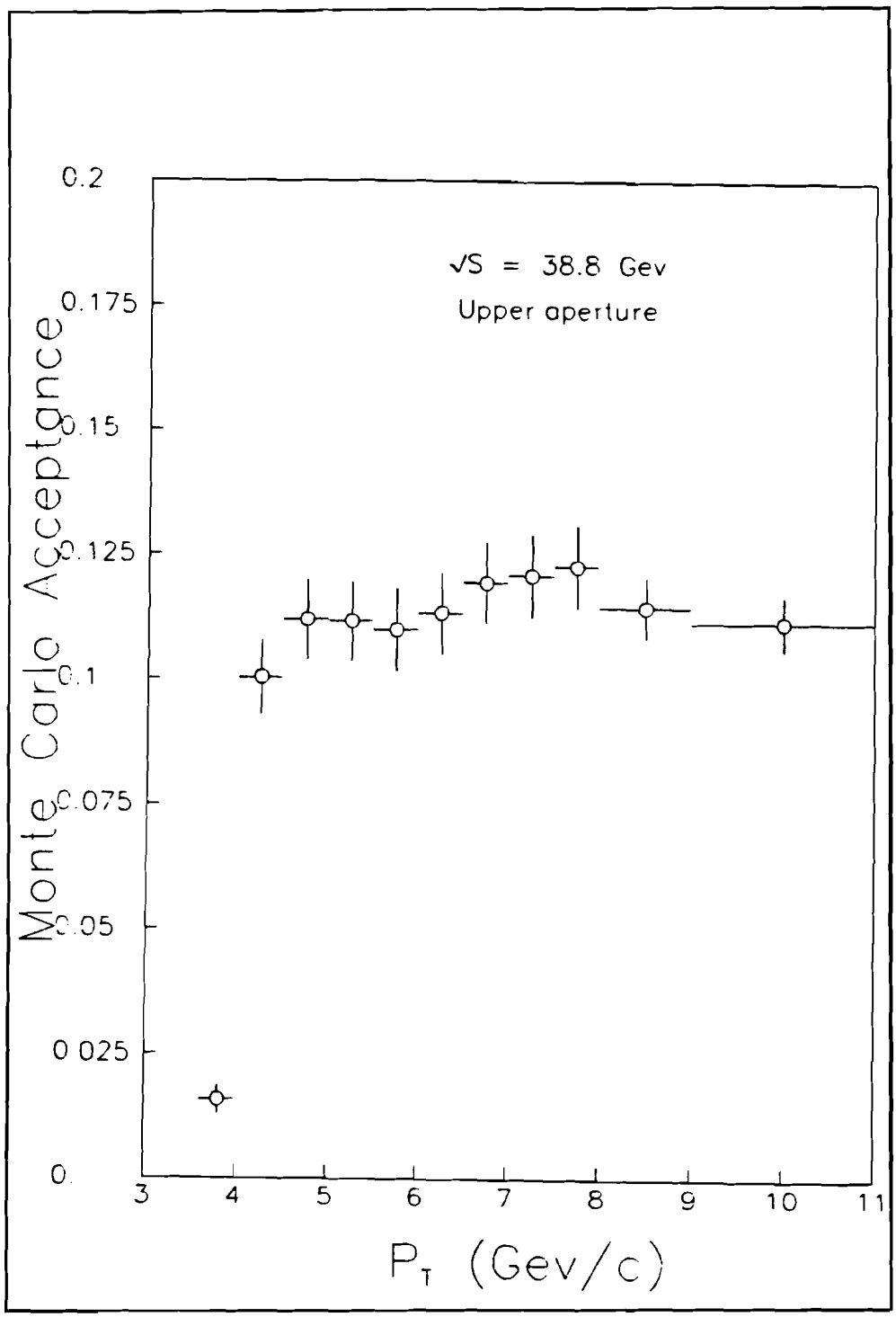

Figure 15. Monte carlo acceptance, 800 *Gev/c*, upper aperture

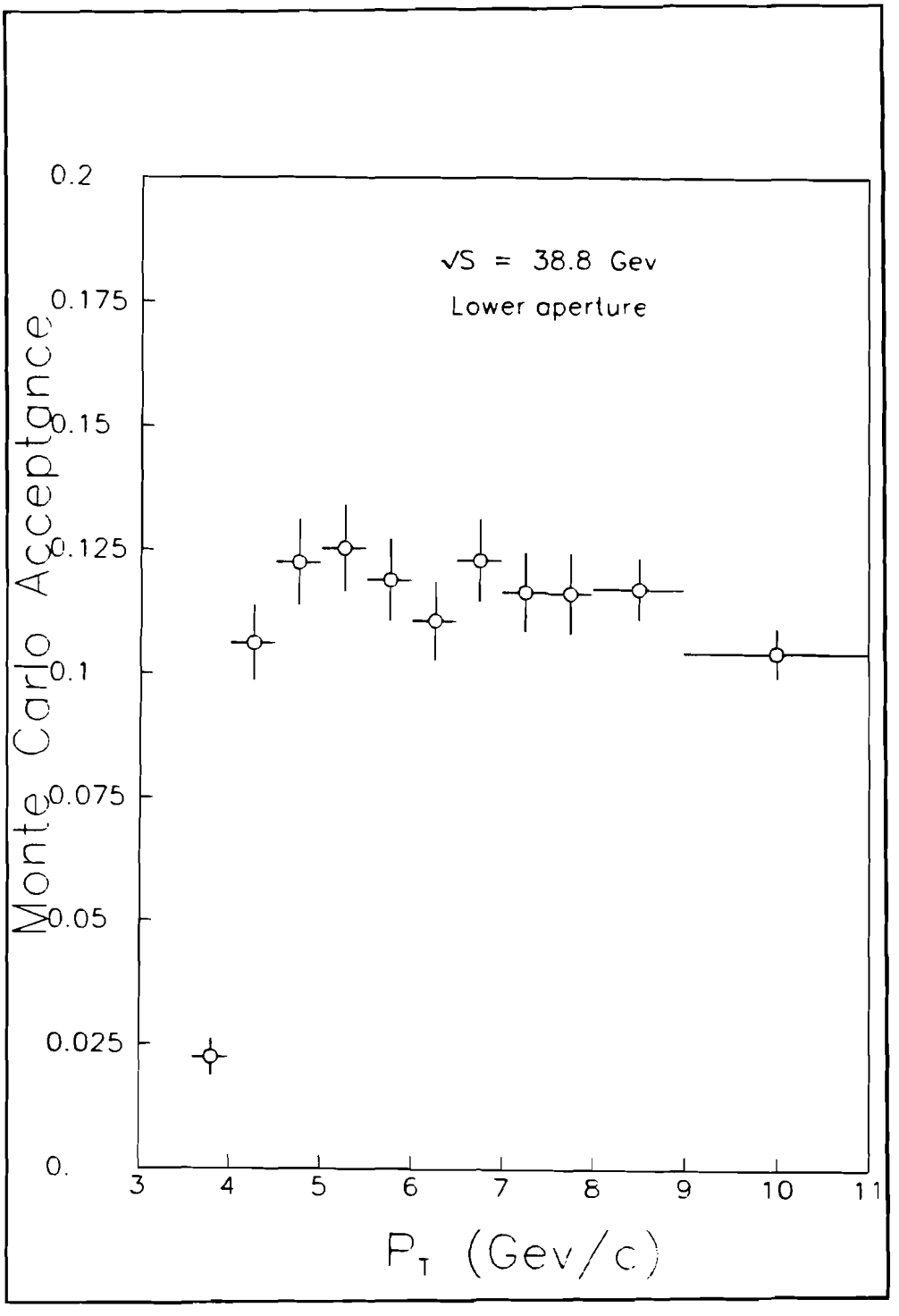

Figure 16. Monte carlo acceptance, 800 *Gev/c*, lower aperture

$n_j \equiv$ number of particles in the j^{th} spill, and

$w^i_{k,t} \equiv$ weight assigned to the k^{th} particle in the i^{th} bin for trigger t.

A four counter telescope pointed at the target perpendicular to the incident beam and monitored the interaction rate in the target. The rate of four-fold coincidences (dubbed AMON), normalized by the SEM, measured the amount of beam interacting in the target. Typically AMON/SEM $\approx$ .05 when neither the metal target holder nor the liquid target vessel was near the beam, while AMON/SEM rate was about 75(200) when the beam was focussed on a 1.0 *mm* high Be(Cu) target, thus the ratio of AMON/SEM for target-in to target-out was at least 1000.[39] In addition the vertical and horizontal beam profiles show that the lateral dimensions of the beam were much smaller than that of the liquid target vessel (see Figures 3 and 4); hence, it was assumed that 100% of the incident beam passed through the liquid target vessel.

The above observations allow the live-time per spill to be computed directly with the gated and ungated target monitor rates:

$$l_j = \frac{\text{AMON (gated by the readout system)}}{\text{AMON(ungated)}} \equiv \frac{\text{AMON} \wedge \text{g}}{\text{AMON}}.$$

The uncertainty in the calculated live time, assuming that the quantities AMON$\wedge\bar{\text{g}}$ and AMON$\wedge$g are uncorrelated, is given by

[39] This large ratio was facilitated by keeping the targets in vacuum.

$$\sigma_{l_j}^2 = (1 - l_j) l_j / \text{AMON} .$$

The integrated luminosity per nucleus of a single spill ,$\mathcal{L}_j$, is given by

$$\mathcal{L}_j = i_j L_{tgt} \rho N_A / A$$

where

$i_j \equiv$ number of protons on target $= f \times$ SEM, $f =$ number of incident protons per SEM count, as described earlier,

$L_{tgt} =$ the length of the target vessel,

$N_A =$ Avogadro's number $= 6.022 \times 10^{23}\ mole^{-1}$,

$A =$ atomic weight of the target material, and

$\rho =$ density of the target material, see the following table.

Table 8: Target Material Properties[40]

Material	Density g/cm^3	Atomic weight
Liquid hydrogen	.0710 ± .0002	1.01
Gaseous hydrogen	.001338 ± .000002	1.01
Liquid deuterium	.161 ± .004	2.0144
Gaseous deuterium	.00230 ± .00005	2.0144
Stainless steel	7.87 ± .03	55.85 ± .60

[40] Liquid Cryogens Vol. 2, Editors, K.D. Williamson, Jr. and F.J. Edeskaty (CRC Press Inc.), p. 3; The density and atomic weight of stainless steel are well-approximated by iron, see Handbook of Chemistry and Physics 64th ed., R.C. Weast, ed. (CRC Press Inc.), p. F-112 and Encyclopedia of Engineering Materials and Processes, H.R. Clauser, ed. (Rheinhold Publ. Co.), p.634.

Assuming that the above quantities are uncorrelated, the systematic uncertainty in the live-time corrected luminosity, $\mathcal{L} \times l$, is

$$\left(\frac{\sigma_{\mathcal{L}\times l}}{\mathcal{L}\times l}\right)^2 = \left(\frac{\sigma_{L_{tgt}}}{L_{tgt}}\right)^2 + \left(\frac{\sigma_\rho}{\rho}\right)^2 + \left(\frac{\sigma_f}{f}\right)^2 + \left(\frac{\sigma_{\mathrm{SEM}}}{\mathrm{SEM}}\right)^2 + \left(\frac{\sigma_l}{l}\right)^2 \quad .$$

The uncertainties in the other quantities were given in section II.B. and II.C.

The weight for each track, $w^i_{k,t}$ is a product of two terms:

$$w^i_{k,t} = w^i_{k,t}(\text{track}) \times w^i_t(\text{event}),$$

$w^i_{k,t}(\text{track})$ refers to contributions that differ for each track while contributions that depend on all the tracks in an event are found in $w^i_t(\text{event})$. Explicitly,

$$w^i_{k,t}(\text{track}) = g^i_\alpha \frac{1}{\epsilon_{hodo}} \frac{1}{\epsilon_{trk}} \frac{1}{\epsilon^k_{abs}} \frac{1}{\epsilon^k_{decay}}$$

and

$$w^i_t(\text{event}) = \frac{1}{\epsilon_{cal,t}} \frac{1}{\epsilon_{processing,t}} \frac{1}{\epsilon^i_{TM,t}} f_{ps,t}$$

where the factors in $w^i_{k,t}(\text{track})$ are

$g^i_\alpha =$ the fractional yield of $\alpha = \pi$, K or p in the i^{th} bin as determined by the Čerenkov hadron species identification program and the following method:[41]

[41] P.B. Straub, Ph.D. thesis.

1) Define g_α^i as the relative fraction of particle type α in the i^{th} bin. For example, $N_\pi^i = g_\pi^i \times N^i$; the number of pions in the i^{th} bin is the particle fraction times the total number of particles in that bin.

2) The normalized probability that the k^{th} particle is type α is then given by

$$\frac{f_k^\alpha g_\alpha}{\sum_{\beta=1}^{3} f_k^\beta g_\beta}$$

3) Combining 1) and 2) yields

$$N_\alpha^i = \sum_{k=1}^{N_i} \frac{g_\alpha^i f_k^\alpha}{\sum_{\beta=1}^{3} g_\beta^i f_k^\beta},$$

where f_k^α was defined in Section IV.H. as the probability that track k is an π, K or p assuming equal incident fluxes.

4) Using the maximum likelihood method, iterate to find the best set of g_α^i that satisfy the equation in 3) with the constraint that $g_\pi^i + g_K^i + g_p^i = 1$.

5) The uncertainties in the set of g_α^i are obviously correlated — only 2 g's are independent. The 'information matrix' that follows from the maximum likelihood method can be used to obtain the error matrix containing the variances and correlations of errors in the g_α^i's.[42]

[42] See Appendix E.

In the computation of the invariant cross section, only the diagonal elements of the resulting error matrix are used. The off-diagonal elements are used in evaluating the uncertainties in the like-sign particle ratios to be shown in section VI.

6) By varying input parameters in the species identification algorithm, the systematic uncertainties in the hadron fractions were determined. The estimated limit of variation in $n^2 - 1$ was $\pm$ 1%, in N_{REAL} was $\pm$ 5%, in N_{JUNK} was $\pm$ 5% and in P_{off} was $\pm$ 10% where n is the index of refraction, N_{REAL} (N_{JUNK}) is the calculated number of Čerenkov(non-Čerenkov) photons per ultrarelativistic track and P_{off} is the probability that the photon detector was inefficient due to sparking. Each of these quantities was determined on a run-by-run basis using well-identified muon tracks. The estimated variations quoted above were an attempt to account for both the statistical precision of the fit for each quantity and the accuracy of the algorithm.

ϵ_{hodo} = efficiency that 4 out of the 5 hodoscopes in stations 1, 2 and 3 fired on the track. The systematic uncertainty in ϵ_{hodo} was determined using the statistical uncertainties of the efficiencies for the individual hodoscope counters,[43]

[43] See Appendix B.

ϵ_{trk} = tracking efficiency. The tracking efficiency and the systematic uncertainty in ϵ_{trk} is calculated from the individual wire chamber efficiencies and errors and the track finding algorithm. Generally $\epsilon_{trk} > 0.90$,

$\epsilon^k_{abs} = 1 - P^k_{abs}$, P^k_{abs} is the species dependent probability that the k^{th} particle was absorbed in the detector or target material before triggering the apparatus. Uncertainties in the exact thickness and composition of the detector materials gives rise to an systematic error on ϵ^k_{abs} of .9 %,

$\epsilon^k_{decay} = 1 - P^k_{decay}$, where P^k_{decay} is the probability that the k^{th} particle decayed before triggering the detector. $P^k_{decay} = \exp(-ms/pc\tau)$, where m = mass, p = total momentum, c = speed of light, τ = proper lifetime and s = track length from the target to the calorimeter of the k^{th} particle. All purely leptonic decay modes of the π and K will not trigger the apparatus, while a negligible fraction ($< .001$ at $p = 100$ Gev/c) of the non-leptonic decays of kaons can both trigger the apparatus and be reconstructed as a target track. The correction for particle decays for π's(K's) is $\approx 1\%(7\%)$ at $p =$ 100 Gev/c. The imprecision of the momentum determination of each track due to the length of the liquid target yields a 1.4% systematic uncertainty in ϵ^k_{decay}.

The terms in w^i_t(event) are

$\epsilon_{cal,t}$ = calorimeter trigger efficiency of the event for trigger t. To

determine the efficiency of calorimeter trigger, t, events were gathered with a lower pulse height threshold using the ETFI trigger. These lower threshold triggers were processed with this algorithm:[44]

1) Given the track positions at the calorimeter, the modules that contain the hadronic showers were determined.

2) The total charge, Q,(corrected for light attenuation in the calorimeter scintillator) deposited in the analog-to-digital converters for those modules was determined.

3) The number of times trigger t fired in coincidence with the lower threshold trigger *versus* Q and the number of times the lower threshold trigger fired *versus* Q were histogrammed.

4) The ratio of the two histograms was fit with an error function,

$$erf(Q; Q_0, \sigma) = \frac{1}{\sqrt{2\pi}\sigma} \int_{-\infty}^{Q} dx \, \exp\left(-\left(\frac{x - Q_0}{\sigma}\right)^2/2\right).$$

where Q_0 was dubbed the trigger threshold and σ the jitter in the threshold. In the next figure, the efficiencies for the seven calorimeter trigger bits described in Section III.B. are shown.

[44] J.A. Crittenden, Ph.D. thesis, Columbia University (1986)

Thus the efficiency for trigger t, with Q^t determined as described in 1) and 2) above, was $erf(Q^t; Q_0^t, \sigma^t)$. The systematic uncertainty in the calorimeter trigger efficiency, $\sigma_{\epsilon_{cal,t}}$, was estimated by noting the range of Q_0^t, σ^t for various subsets of the lower threshold trigger data. For the 800 *Gev*(400 *Gev*) data, the accuracy of the measurement of the threshold and jitter was ±.5% and ±4.6% (±1.0% and ±9.2%), respectively. Finally, the efficiency of the ETFI trigger was determined by extrapolating the EHI efficiency curve using the relative thresholds of the two triggers. The thresholds of the other triggers were sufficiently higher than the ETFI threshold so that the ETFI trigger was fully efficient for those triggers thus validating the use of the ETFI trigger in the determination of the calorimeter trigger efficiencies.

$\epsilon^i_{TM,t}$ = trigger matrix efficiency for the i^{th} bin for trigger t.[45] If trigger t did not require the trigger matrix, $\epsilon^i_{TM,t} = 1.0$. The trigger matrix efficiency for a given $p_\perp$ bin was determined, using the ETFI triggers, as the number of events accepted in bin i with trajectories that could have satisfied the trigger matrix divided by the total number of accepted events in that bin. The systematic uncertainty, $\sigma^i_{\epsilon_{TM,t}}$, was assumed to be due to the statistical uncertainty in the number of events per bin. Figures

[45] The trigger matrix efficiency depended on particle momentum due to a FORTRAN error in the monte carlo program that generated the allowed hodoscope hit patterns for each trigger matrix.

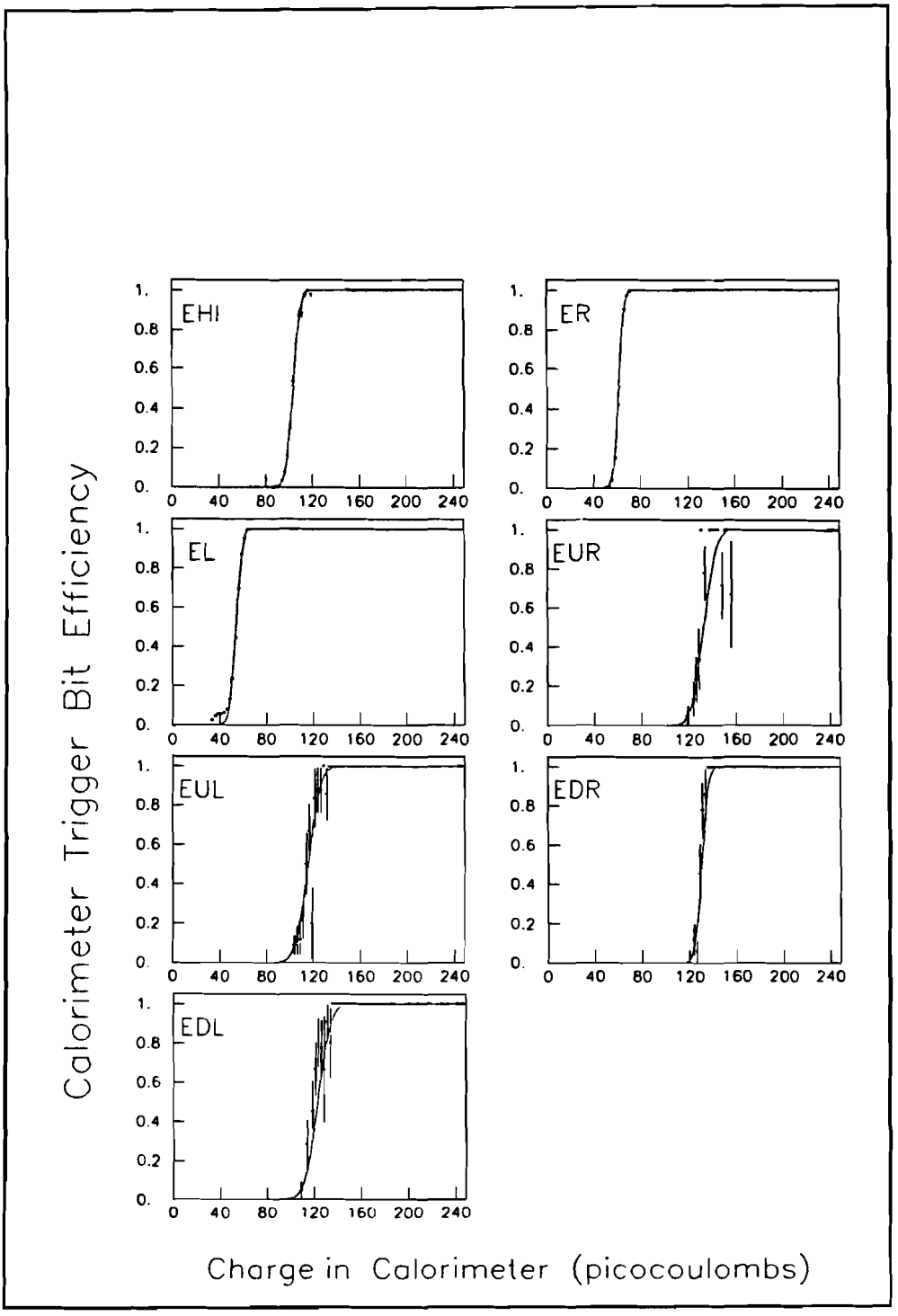

Figure 17. Calorimeter Trigger Bit Efficiencies

18-21 show the measured trigger matrix efficiency for the 400 and 800 *Gev/c* running conditions. The bin width is shown by the horizontal error bars.

$\epsilon_{processing,t}$ = 'efficiency' of the read-out electronics and analysis program for trigger t. Due to software and hardware problems, not all triggers could be analyzed. Triggers were lost when the data format of an event on magnetic tape was corrupted, the length of an event exceeded the buffer allocated or an excessive number of triplet or track candidates were found. Presumably none of these difficulties are correlated with the invariant cross section because the spill cuts described in Section IV.G. and the requirement of a large calorimeter energy deposit in the trigger insured that the number of events was directly proportional to the interaction rate; therefore, events were corrected based on $\epsilon_{processing,t}$ for each run. The processing efficiency was defined to be the number of triggers of type t analyzed divided by the number of t triggers recorded by a scaler gated by the read-out system. The systematic uncertainty in this factor was taken to be due to the statistical uncertainties of the number of triggers analyzed and recorded on the scaler. Runs with $.85 < \epsilon_{processing,t} < 1.00$ were accepted for analysis and the mean, weighted processing efficiency exceeded .985 for all triggers.

$f_{ps,t}$ = prescaling factor for trigger t.

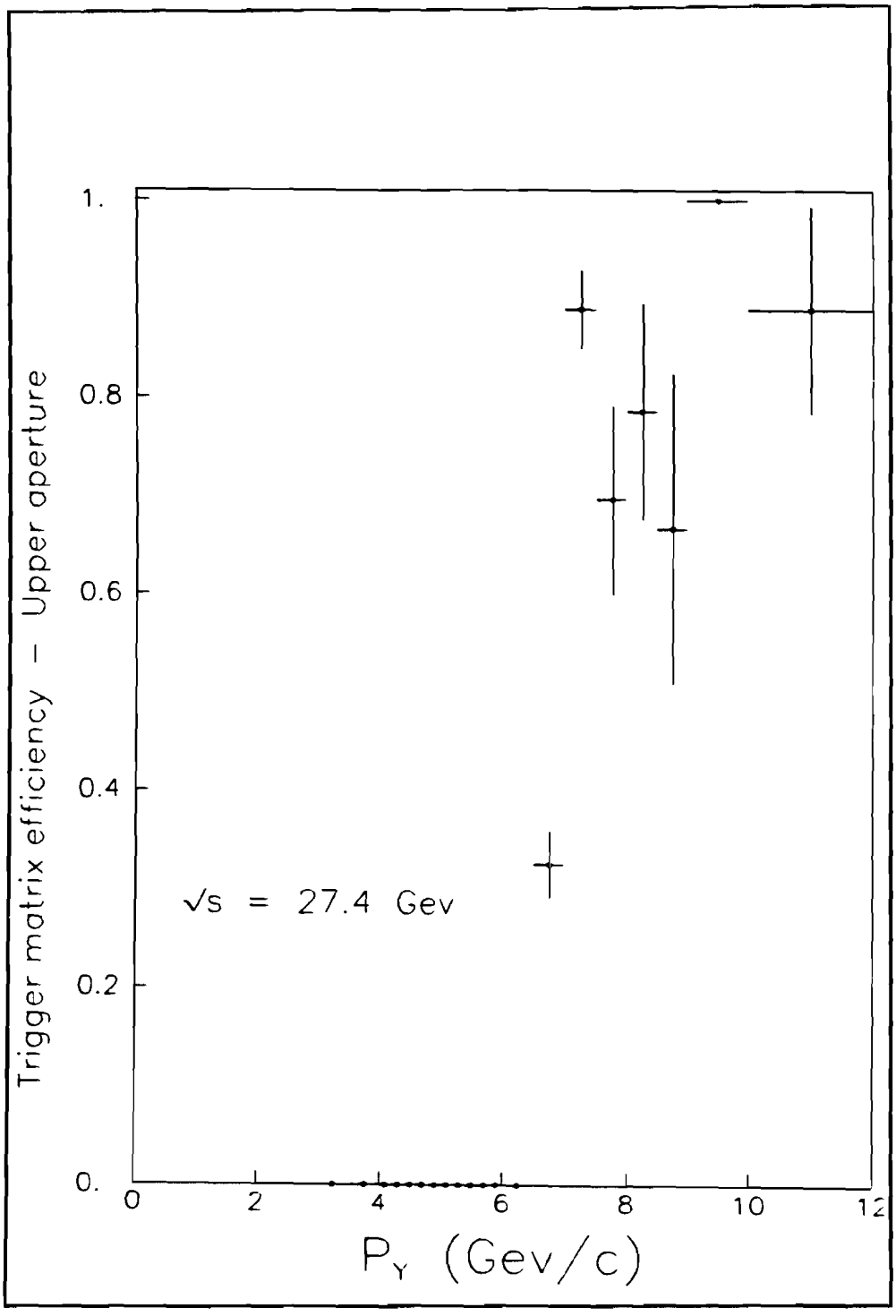

Figure 18. Trigger Matrix Efficiency, 400 *Gev/c*, Upper Aperture

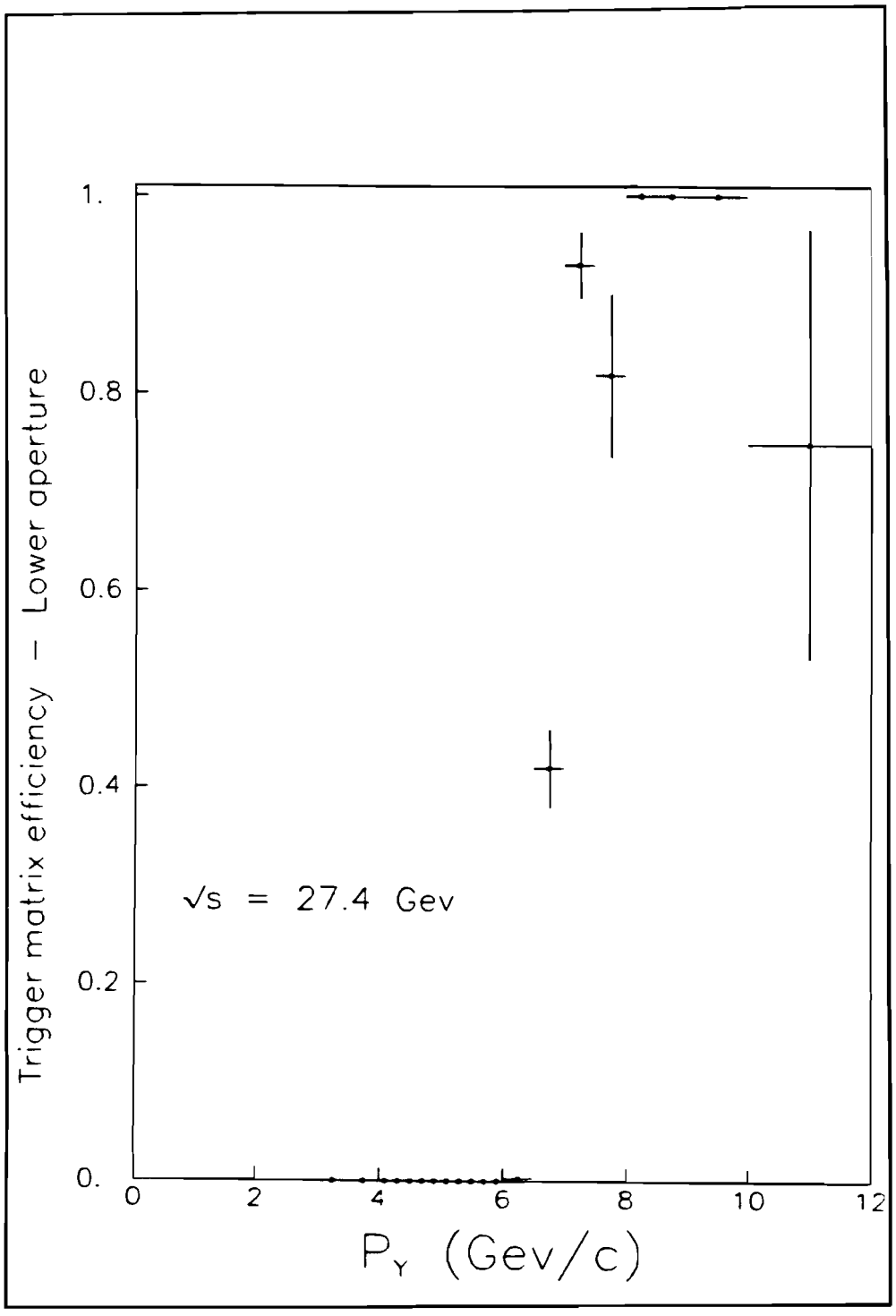

Figure 19. Trigger Matrix Efficiency, 400 *Gev/c*, Lower Aperture

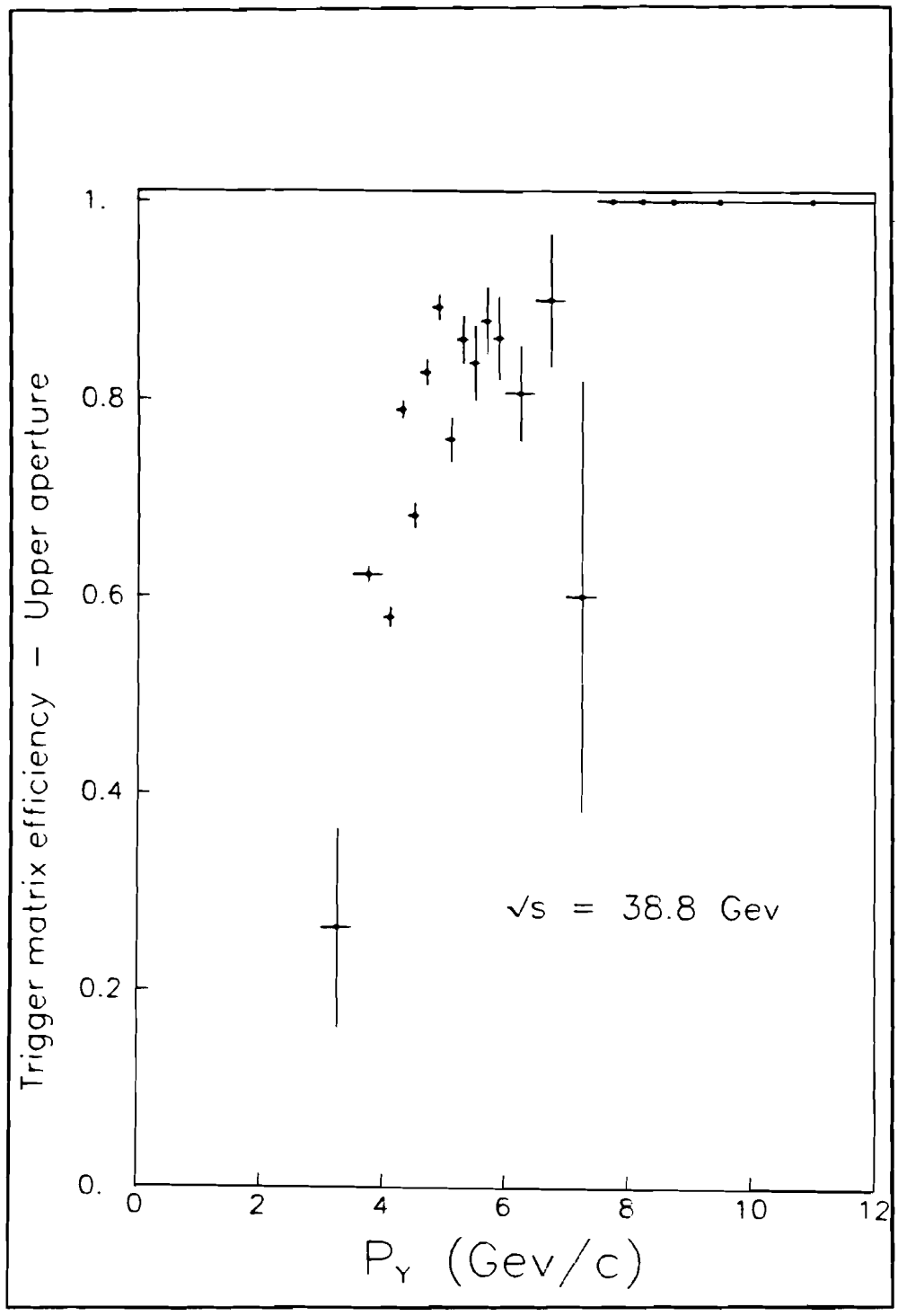

Figure 20. Trigger Matrix Efficiency, 800 *Gev/c*, Upper Aperture

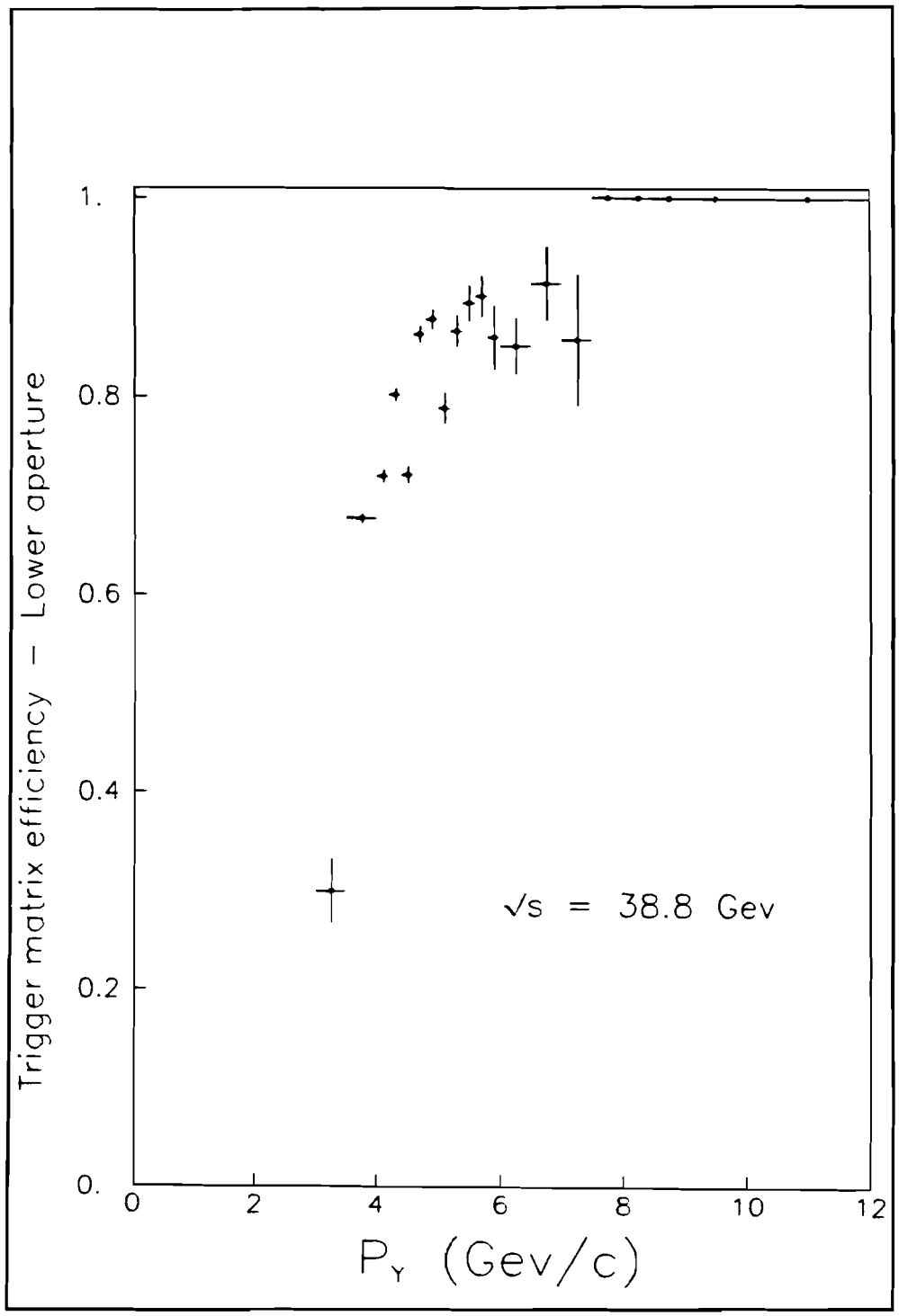

Figure 21. Trigger Matrix Efficiency, 800 *Gev/c*, Lower Aperture

Since the contributions to each particle's weight are assumed to be uncorrelated, the systematic uncertainty in the weight for each particle was

$$\left(\frac{\sigma_w}{w}\right)^2 = \left(\frac{\sigma_w}{w}\right)^2_{\text{event}} + \left(\frac{\sigma_w}{w}\right)^2_{\text{track}}$$

$$\left(\frac{\sigma_w}{w}\right)^2_{\text{event}} = \left(\frac{\sigma_{\epsilon^i_{TM}}}{\epsilon^i_{TM}}\right)^2 + \left(\frac{\sigma_{\epsilon_{processing,t}}}{\epsilon_{processing,t}}\right)^2 + \left(\frac{\sigma_{\epsilon_{cal,t}}}{\epsilon_{cal,t}}\right)^2$$

and

$$\left(\frac{\sigma_w}{w}\right)^2_{\text{track}} = \left(\frac{\sigma_{g^k_\alpha}}{g^k_\alpha}\right)^2 + \left(\frac{\sigma_{\epsilon^k_{abs}}}{\epsilon^k_{abs}}\right)^2 + \left(\frac{\sigma_{\epsilon^k_{decay}}}{\epsilon^k_{decay}}\right)^2 + \left(\frac{\sigma_{\epsilon_{trk}}}{\epsilon_{trk}}\right)^2 + \left(\frac{\sigma_{\epsilon_{hodo}}}{\epsilon_{hodo}}\right)^2.$$

In addition the statistical uncertainty in total weight for each bin, assuming Poisson statistics, was the square root of the sum of the squares of the weights of each particle.

One additional effect to be considered was the effect of the target vessel which can be remedied by noting that

$$L_m\langle\sigma^m_i\rangle = N_{i,m}/A_i,$$

where

L_m = integrated luminosity for material m,

$\left\langle \sigma_i^m \right\rangle \equiv \left\langle E\frac{d^3\sigma}{dp^3}_i \right\rangle \int_{\Omega_i} d^3p/E$ for material m.

The above equation was used to write two equations in two unknowns for the weighted number of events for the i^{th} bin when the target was emptied and filled:

$$N_{i,e}/A_i = L_{H_2,e}\left\langle \sigma_i^{H_2} \right\rangle + L_{ss,e}\langle \sigma_i^{ss} \rangle$$

$$N_{i,f}/A_i = L_{H_2,f}\left\langle \sigma_i^{H_2} \right\rangle + L_{ss,f}\langle \sigma_i^{ss} \rangle$$

$L_{H_2,e(f)}$ denotes the integrated luminosity on the hydrogen gas(liquid) during the emptied(filled) target runs; similarly, $L_{ss,e(f)}$ denotes the integrated luminosity on the stainless steel windows and target vessel. These two equations were solved to yield $\left\langle \sigma_i^{H_2} \right\rangle$ on a bin-by-bin basis.

V. C. Dihadron Cross Section[46]

The doubly differential two particle cross section can be written in terms of the integrated luminosity and number of hadron pairs, (only unlike sign hadron pairs were considered)

$$N_{12i} = LA \int_{\Delta_i} (E_1E_2\frac{d^6\sigma}{dp_1^3dp_2^3})\ \frac{d^3p_1}{E_1}\frac{d^3p_2}{E_2}$$

where,

i denotes a bin in the 6-dimensional space of the two particle 3-momenta($\vec{p_1}$ and $\vec{p_2}$),

[46] Although the dihadron cross section was not measured directly, the correlation function in section V.E. is defined in terms of the two particle cross section.

Δ_i denotes the volume of this bin in momentum space, and

$N_{12i} \equiv$ number of dihadrons produced into the i^{th} bin.

A = the dihadron acceptance for this bin, which is the product of the single particle acceptances, A_1 and A_2.

Following the notation and definitions of the previous section,

$$\left\langle E_1 E_2 \frac{d^6\sigma}{dp_1^3 dp_{2i}^3} \right\rangle = \frac{N_{12i}}{LA} \Big/ \int_{\Delta_i} \frac{d^3p_1}{E_1} \frac{d^3p_2}{E_2}.$$

The number of dihadrons in the i^{th} bin was once again the sum of weights

$$N_{12i} = \sum_{j}^{spills} \sum_{k}^{n_i} w_{k,t}^i$$

where the weight of an event was now given by

$$w_{k,t}^i = w_t^i(\text{event}) \times w_{k,t}^i(\text{track 1}) \times w_{k,t}^i(\text{track 2})$$

where w_t^i(event) and $w_{k,t}^i$(track) were defined in the previous section with the notable exception that the quantity g_α^i for each track was replaced by $g_{\alpha\beta}^i$ for the pair of tracks. For example the number of $K^+\pi^-$ in the i^{th} bin is $N_{12i} g_{K^+\pi^-}^i$. Similarly, $f_{\alpha\beta}$ replaced f_α as the hadron identification probability density for the pair $\alpha\beta$.

The $g_{\alpha\beta}^i$ were found as before by solving the following equation

$$N_{12i} g_{\alpha\beta}^i = \sum_{k=1}^{N_{12i}} \frac{g_{\alpha\beta}^i f_{\alpha\beta}^k}{\sum_{\gamma\delta=1}^{9} g_{\gamma\delta}^i f_{\gamma\delta}^k}$$

with the constraint $\sum_{\alpha\beta=1}^{9} g^{i}_{\alpha\beta} = 1$.

V. D. Binning

In any experiment only a finite number of events can be accumulated; hence, in order to obtain statistically significant results, kinematically similar events must be counted together in the same bin. Bins were defined with a limited range of $p_{\perp}$ and $\cos\Theta^{*}$ and spanned the full azimuthal range. The following table shows the bins selected for the single pion cross section calculations at 400 and 800 *Gev/c*.

Table 9: Single Hadron Bin Limits

(400 *Gev/c*) $-.3 < \cos\Theta^* < .3$		(800 *Gev/c*) $-.2 < \cos\Theta^* < .2$	
Lower $p_\perp$ limit(*Gev/c*)	Upper $p_\perp$ limit(*Gev/c*)	Lower $p_\perp$ limit(*Gev/c*)	Upper $p_\perp$ limit(*Gev/c*)
5.2	5.7	3.6	4.0
5.7	6.2	4.0	4.5
6.2	6.7	4.5	5.0
6.7	7.2	5.0	5.5
7.2	7.7	5.5	6.0
7.7	9.0	6.0	6.5
		6.5	7.0
		7.0	7.5
		7.5	8.0
		8.0	9.0
		9.0	11.0

The CMS bin limits were chosen to assure an adequate number of events in each bin and a reasonable acceptance as determined by the monte carlo. The hadron species identification program required at least 100 events per bin for a statistically significant measurement since the proton fraction is about .05. The monte carlo acceptance for a bin was required to be greater than .5 % to avoid regions of phase space near the edges of the acceptance with possible large systematic uncertainty. Because the monte carlo only determined the geometric acceptance and not the overall efficiency of the E605 apparatus, any bin with an event with an efficiency less than .05 was rejected. The minimum average efficiency for all bins that passed this cut was 37%. This criteria essentially eliminated bins at the limits of the overall detector acceptance.

Since the particle fractions and like-sign particle ratios were determined without a need to consider the trigger efficiency, the results presented generally span the entire range in $p_\perp$ except for measurements consistent with zero at one standard deviation which were excluded. On the other hand, the measurement of the single pion cross-sections and unlike-sign particle ratios involved the trigger efficiency, hence certain bins for these measurements were eliminated by the minimum efficiency cut described above.

V. E. The Correlation Function

The hadron pair correlation function, R, is defined in terms of the cross sections for single and dihadron production[47]

$$R = \frac{E_1 E_2 \frac{d^6\sigma}{dp_1^3 dp_2^3}/\sigma_{in}}{\left(E_1 \frac{d^3\sigma_1}{dp_1^3}/\sigma_{in}\right)\left(E_2 \frac{d^3\sigma_2}{dp_2^3}/\sigma_{in}\right)}$$

where $\sigma_{in} \equiv$ inelastic proton-proton cross section. Re-writing the above expression in terms of the weighted number of events per bin yields

$$R = \frac{N_{1,2}^{real}(p_1, p_2)/N_{int}}{(N_1(p_1)/N_{int})\,(N_2(p_2)/N_{int})},$$

where

N_{int} = total number of interacting protons,

$N_i(p_i)$ = weighted number of single hadrons in the bin denoted by 3-momentum p_i, and

$N_{1,2}^{real}$ = weighted number of <u>real</u> hadron pairs produced into the bin denoted by momenta $\vec{p}_1$ and $\vec{p}_2$.

[47] H. Jöstlein *et. al.*

To obtain the number of real hadron pairs, $N_{1,2}^{real}$, from the total number of pairs observed, $N_{1,2}^{tot}$, the number of accidental pairs, $N_{1,2}^{acc}$, must be determined. As shown in Appendix C, $N_{1,2}^{acc} = N_1 N_2 / N_{eff}$ (N_{eff} = effective total number of RF buckets). Thus the correlation function becomes

$$R = N_{int}\left(\frac{N_{1,2}^{tot}(p_1,p_2)}{N_1(p_1)N_2(p_2)} - \frac{1}{N_{eff}}\right)$$

utilizing the relation $N_{1,2}^{tot} - N_{1,2}^{acc} = N_{1,2}^{real}$.

In addition, the correlation function for the production of two specific hadron species α and β, relative to R is

$$r_{\alpha\beta} = \frac{N_{int}\left(\frac{N_{1,2}^{tot(\alpha\beta)}(p_1,p_2)}{N_1^{\alpha}(p_1)N_2^{\beta}(p_2)} - \frac{1}{N_{eff}}\right)}{N_{int}\left(\frac{N_{\alpha\beta}^{tot}(p_1,p_2)}{N_1(p_1)N_2(p_2)} - \frac{1}{N_{eff}}\right)}$$

or, in terms of the single and diparticle fractions, g_α, g_β and $g_{\alpha\beta}$, described in the previous sections

$$r_{\alpha\beta} = \frac{\frac{N_{12}}{N_1 N_2}\frac{g_{\alpha\beta}}{g_\alpha g_\beta} - \frac{1}{N_{eff}}}{\frac{N_{12}}{N_1 N_2} - \frac{1}{N_{eff}}}.$$

Thus in the limit of no accidental pairs, $r_{\alpha\beta} = g_{\alpha\beta}/(g_\alpha g_\beta)$.

The systematic uncertainty for the relative correlation function $r_{\alpha\beta}$ depends on the uncertainty in $g_{\alpha\beta}$. Complicating the hadron species identification for pairs are events where the Čerenkov photons from both tracks overlap on a single photon detector. An estimate of the uncertainty in the dihadron identification was made by comparing the $g_{\alpha\beta}$'s for two cases:

1) both tracks' photons share one detector and

2) each track strikes a different detector.

The average magnitude of the difference in the $g_{\alpha\beta}$'s for each case provided the limit of systematic uncertainty for each diparticle fraction. The following table show the calculated fractions and statistical and systematic uncertainties for each pair type for all of the 3531 dihadrons.

Table 10: Dihadron Fractions

Pair	Fraction (g_{ij})	Statistical uncertainty	Estimated systematic uncertainty
$\pi^+\pi^-$	.585	.014	.019
$K^+\pi^-$	.244	.012	.005
$p\pi^-$	.039	.007	.014
π^+K^-	.065	.007	.001
K^+K^-	.039	.006	.003
pK^-	.012	.006	.001
$\pi^+\overline{p}$	.004	.003	.002
$K^+\overline{p}$	.004	.003	.001
$p\overline{p}$	.009	.004	.004

Proton identification was most affected by the photon sharing complication, while the effect on pion and kaon pairs was of comparable or greater magnitude but relatively smaller.

Another complication in the calculation of R is that the dihadron trigger, EL $\wedge$ ER, was not simply the product of two single particle triggers. Hence the weighted number of events must be used to compute R. To minimize the uncertainty in R due to single hadrons, only the ETFI/PS trigger was used.

VI. Results

VI. A. Single Pion Invariant Cross Section

In Figures 22-27 the average over each CMS bin of the single pion invariant cross section is plotted *versus* the weighted mean transverse momentum, $\langle p_\perp \rangle$, per bin. The point-to-point errors shown are the statistical and systematic uncertainties added in quadrature. Lists of the results are given in Tables 11-13. Note that the $p_\perp$ that corresponds to the measured average cross section is not identical to $\langle p_\perp \rangle$. However, the difference between $\langle p_\perp \rangle$ and $p_\perp$ of the average cross section is less than .15 *Gev/c* for all the measurements shown and does not appreciably affect the shape of the cross section versus $p_\perp$.

Shown for comparison at $\sqrt{s} = 27.4$ *Gev* are the results of the Chicago-Princeton (CP) collaboration[48] obtained at $< \Theta^* >= 96°$ ($< \cos\Theta^* >= -.105$). In addition extrapolations of results of the CP and CERN-Columbia-Rockefeller-Saclay (CCRS)[49] collaborations based on fits of the form $E\frac{d^3\sigma}{dp^3} = Af(x_\perp)p_\perp^{-N}$ are shown with the measurements of this experiment at $\sqrt{s} = 38.8$ *Gev* for comparison.

All results confirm the steep dependence of the single pion

[48] D. Antreasyan et al, Phys. Rev. D19, 764 (1979)
[49] F.W. Büsser et al., Nuclear Physics B106, 1 (1976)

cross section on $p_\perp$. The $\sqrt{s} = 27.4$ cross sections for both $\pi^+$and π^-in *pp* and *pd* collisions show very good agreement with the CP measurements in the region where the measurements overlap while the $\sqrt{s} = 38.8$ *Gev pp* cross sections are consistent with the re-scaled CP data and systematically higher than the CCRS fit.

The results of fits to the proton-proton data over the entire $x_\perp$range ($.19 < x_\perp < .66$) with the scaling form $E\frac{d^3\sigma}{dp^3} = Af(x_\perp)p_\perp^{-N}$ with two forms of $f(x_\perp)$ are shown in Table 14.[50] The fits were performed on the cross section as a function of the bin and not $\langle p_\perp \rangle$ to avoid the problem noted previously. Also shown in the table are results of fits by CP and CCRS to their data. In the measurements of this experiment only the diagonal elements of the error matrix are shown. There is, however, a strong correlation between b and N, perhaps due to only two values of $\sqrt{s}$ available in this experiment compared to three values used by CP and CCRS. Both fits give similar values of N for $\pi^+$and π^-production and show an almost identical dependence on $p_\perp$as observed by CCRS or CP. Fits restricted to a high $x_\perp$range ($x_\perp > .35$) did not yield significantly different results for N.

[50] In the table DOF is the number of degrees of freedom.

Table 11: Single pion cross section $\sqrt{s} = 27.4$ *Gev pp*

$p_\perp$ bin	$\langle p_\perp \rangle$	$E\frac{d^3\sigma}{dp^3}$ $(pp \rightarrow \pi^- X)$
Gev/c	*Gev/c*	$[\mathrm{pb}/(Gev^{\,2}/c^3)]$
5.2 – 5.7	5.60	$(\ 2.37 \pm 1.03 \pm 0.19) \times 10^1$
5.7 – 6.2	5.97	$7.33 \pm 2.12 \pm 0.46$
6.2 – 6.7	6.35	$1.97 \pm 0.84 \pm 0.16$
$p_\perp$ bin	$\langle p_\perp \rangle$	$E\frac{d^3\sigma}{dp^3}$ $(pp \rightarrow \pi^+ X)$
Gev/c	*Gev/c*	$[\mathrm{pb}/(Gev^{\,2}/c^3)]$
5.2 – 5.7	5.52	$(\ 3.41 \pm 1.78 \pm 0.41) \times 10^1$
5.7 – 6.2	5.95	$(\ 1.53 \pm 0.31 \pm 0.09) \times 10^1$
6.7 – 7.2	6.92	$1.05 \pm 0.56 \pm 0.09$
7.2 – 7.7	7.56	$(\ 2.15 \pm 1.32 \pm 0.45) \times 10^{-1}$
7.7 – 9.0	8.10	$(\ 1.52 \pm 0.94 \pm 0.67) \times 10^{-2}$

Table 12: Single pion cross section $\sqrt{s} = 27.4$ *Gev pd*

$p_\perp$ bin *Gev/c*	$\langle p_\perp \rangle$ *Gev/c*	$E\frac{d^3\sigma}{dp^3}$ $(pp \rightarrow \pi^- X)$ [pb/(Gev $^2/c^3$)]
5.2 – 5.7	5.57	(8.73 ±2.12 ±0.58) $\times 10^1$
5.7 – 6.2	5.96	(1.46 ±0.20 ±0.08) $\times 10^1$
6.2 – 6.7	6.44	3.67 ±0.61 ±0.23
6.7 – 7.2	6.83	1.16 ±0.32 ±0.08
7.2 – 7.7	7.43	(4.60 ±1.07 ±0.30) $\times 10^{-1}$
7.7 – 9.0	8.04	(1.66 ±0.40 ±0.30) $\times 10^{-2}$
$p_\perp$ bin *Gev/c*	$\langle p_\perp \rangle$ *Gev/c*	$E\frac{d^3\sigma}{dp^3}$ $(pp \rightarrow \pi^+ X)$ [pb/(Gev $^2/c^3$)]
5.2 – 5.7	5.57	(7.87 ±1.56 ±0.77) $\times 10^1$
5.7 – 6.2	5.95	(2.15 ±0.24 ±0.13) $\times 10^1$
6.2 – 6.7	6.41	7.07 ±0.90 ±0.47
6.7 – 7.2	7.02	(9.23 ±3.29 ±0.98) $\times 10^{-1}$
7.2 – 7.7	7.46	(4.77 ±0.87 ±0.27) $\times 10^{-1}$
7.7 – 9.0	8.13	(2.97 ±0.64 ±0.61) $\times 10^{-2}$

Table 13: Single pion cross section $\sqrt{s} = 38.8$ *Gev pp*

$p_\perp$ bin *Gev/c*	$\langle p_\perp \rangle$ *Gev/c*	$E\frac{d^3\sigma}{dp^3}$ $(pp \rightarrow \pi^- X)$ [pb/(*Gev* $^2/c^3$)]
3.6 – 4.0	3.87	(1.00 ±0.18 ±0.08) $\times 10^4$
4.0 – 4.5	4.23	(3.26 ±0.27 ±0.24) $\times 10^3$
4.5 – 5.0	4.71	(9.92 ±0.83 ±0.77) $\times 10^2$
5.0 – 5.5	5.17	(2.83 ±0.31 ±0.27) $\times 10^2$
5.5 – 6.0	5.63	(1.06 ±0.14 ±0.09) $\times 10^2$
6.0 – 6.5	6.29	(3.58 ±0.78 ±0.31) $\times 10^1$
7.0 – 7.5	7.22	1.85 ±0.68 ±0.16
7.5 – 8.0	7.71	1.60 ±0.44 ±0.12
8.0 – 9.0	8.50	(4.52 ±1.73 ±0.43) $\times 10^{-1}$
$p_\perp$ bin *Gev/c*	$\langle p_\perp \rangle$ *Gev/c*	$E\frac{d^3\sigma}{dp^3}$ $(pp \rightarrow \pi^+ X)$ [pb/(*Gev* $^2/c^3$)]
3.6 – 4.0	3.89	(1.62 ±0.33 ±0.13) $\times 10^4$
4.0 – 4.5	4.23	(4.62 ±0.38 ±0.33) $\times 10^3$
4.5 – 5.0	4.73	(1.40 ±0.12 ±0.11) $\times 10^3$
5.0 – 5.5	5.20	(4.42 ±0.40 ±0.39) $\times 10^2$
5.5 – 6.0	5.64	(1.66 ±0.19 ±0.14) $\times 10^2$
6.0 – 6.5	6.14	(5.87 ±0.88 ±0.45) $\times 10^1$
6.5 – 7.0	6.64	(1.35 ±0.16 ±0.08) $\times 10^1$
7.0 – 7.5	7.26	5.72 ±0.81 ±0.36
7.5 – 8.0	7.82	2.64 ±0.68 ±0.16
8.0 – 9.0	8.44	(6.78 ±1.87 ±0.58) $\times 10^{-1}$
9.0 –11.0	9.65	(5.87 ±4.20 ±1.00) $\times 10^{-2}$

Table 14: $Ed^3\sigma/dp^3 = Af(x_\perp)p_\perp^{-N}$ Scaling Fit Results for pp

	This experiment ($.19 < x_\perp < .66$)			
$f(x_\perp)$	b	N	χ^2/DOF	
$(1-x_\perp)^b$	10.6 ± 0.6	8.4 ± 0.1	9.4/9	π^+
$(1-x_\perp)^b$	10.8 ± 0.3	8.4 ± 0.1	16.1/13	π^-
	CP collaboration ($.35 < x_\perp < .64$)			
$f(x_\perp)$	b	N	χ^2/DOF	
$(1-x_\perp)^b$	9.0 ± 0.5	8.2 ± 0.5	17/8	π^+
$(1-x_\perp)^b$	9.5 ± 0.5	8.5 ± 0.5	5.8/7	π^-
	This experiment ($.19 < x_\perp < .66$)			
$f(x_\perp)$	b	N	χ^2/DOF	
$e^{-bx_\perp}$	17.2 ± 1.0	7.7 ± 0.2	10.4/9	π^+
$e^{-bx_\perp}$	$20.4 \pm .4$	7.0 ± 0.1	21.5/13	π^-
	CCRS collaboration($.11 < x_\perp < .36$)			
$f(x_\perp)$	b	N	χ^2/DOF	
$e^{-bx_\perp}$	15.4 ± 1.2	$7.5 \pm .17$	72/63	π^+
$e^{-bx_\perp}$	16.1 ± 1.2	7.86 ± 0.30	70/64	π^-

VI. B. Single Hadron Like-sign Ratios

Tables 15-20 contain the single hadron production fractions and like-sign ratios measured for $\sqrt{s} = 27.4$ and $\sqrt{s} = 38.8$ *Gev* pp and pd interactions. Each entry in the table gives the fractions

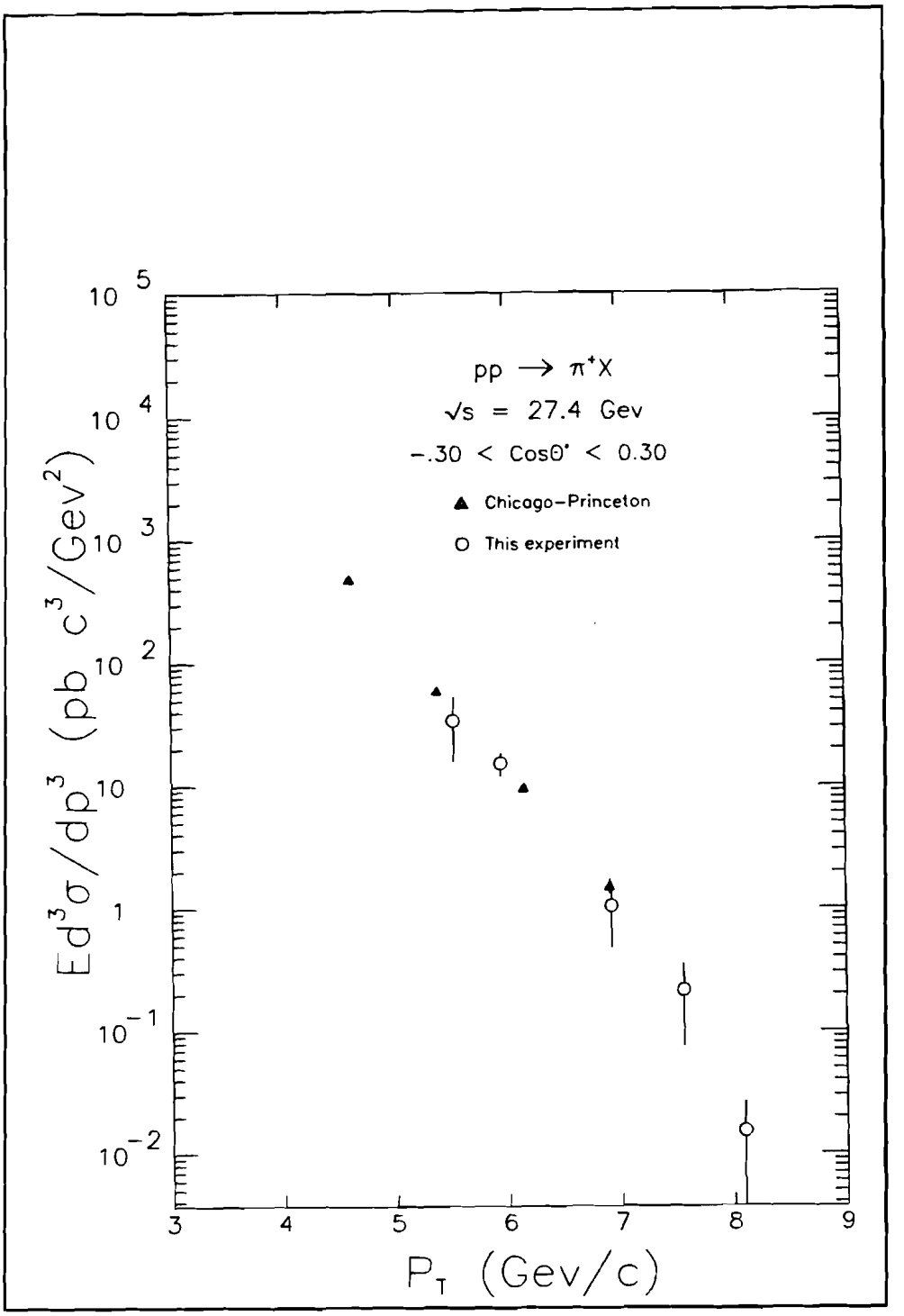

Figure 22. $E\frac{d^3\sigma}{dp^3}$ $(pp \rightarrow \pi^+ X)$ *versus* $p_\perp(Gev/c)$ at $\sqrt{s} = 27.4$ *Gev*

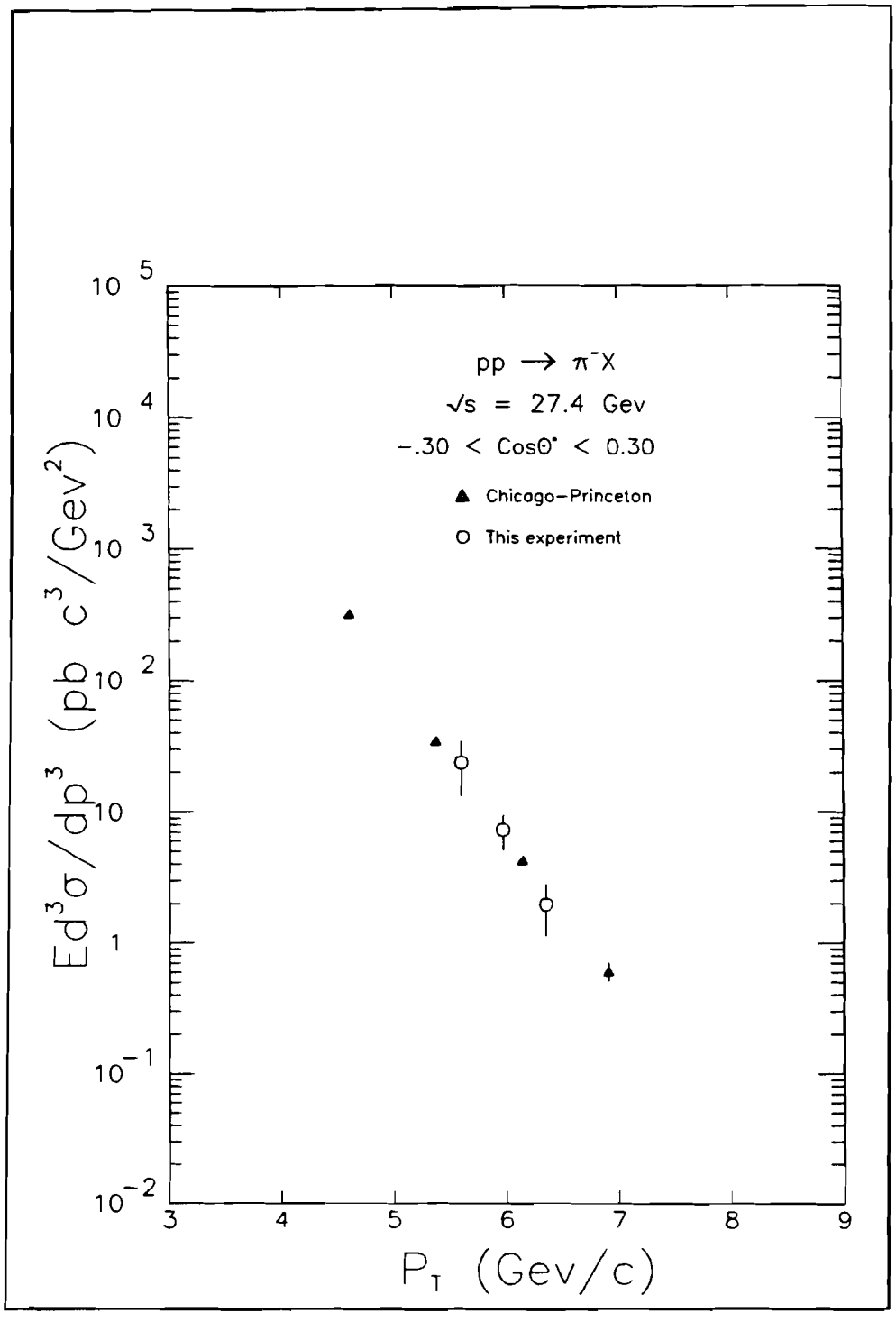

Figure 23. $E\frac{d^3\sigma}{dp^3}$ $(pp \rightarrow \pi^- X)$ *versus* $p_\perp (Gev/c)$ at $\sqrt{s} = 27.4$ *Gev*

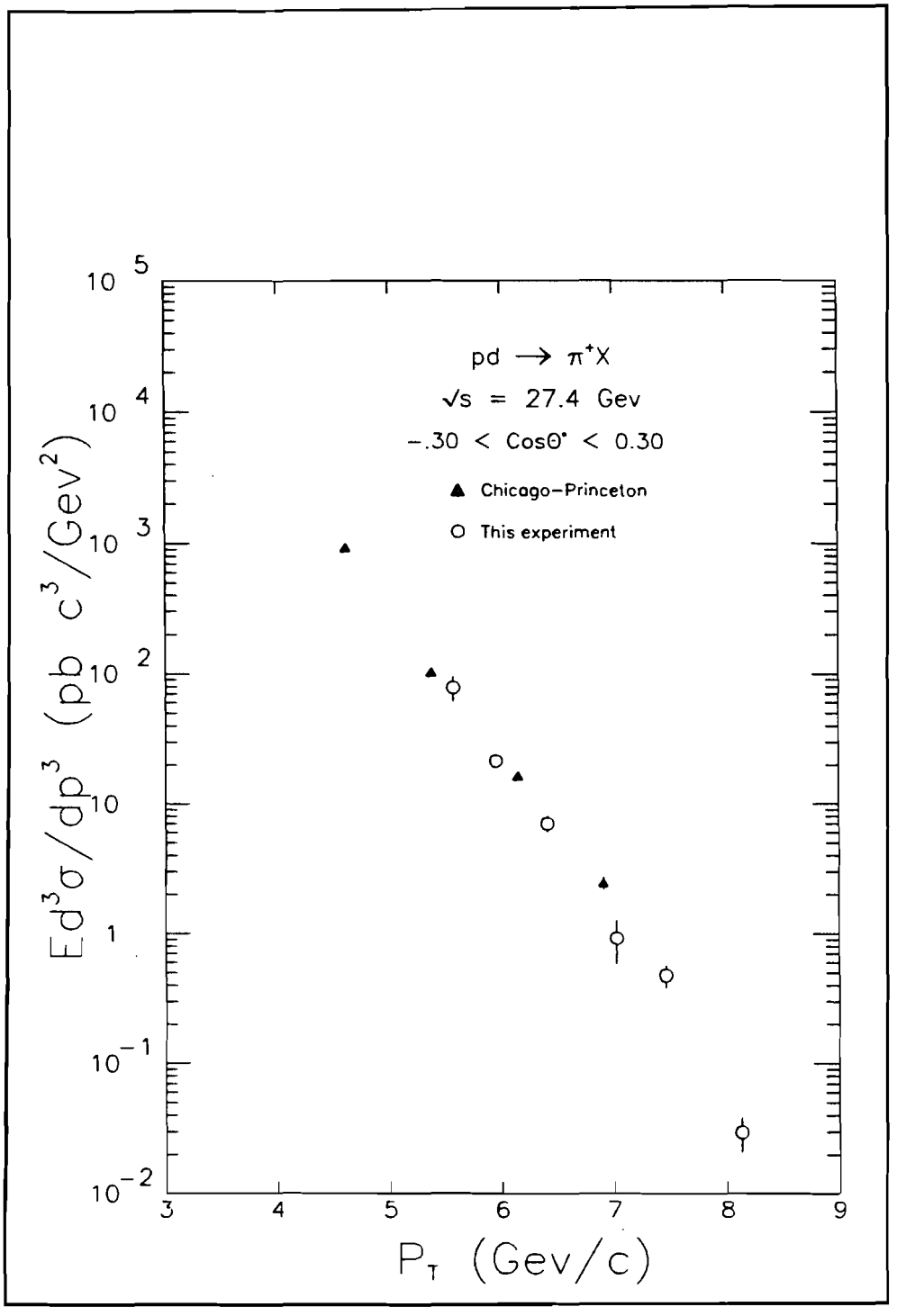

Figure 24. $E\frac{d^3\sigma}{dp^3}$ $(pd \rightarrow \pi^+ X)$ *versus* $p_\perp (Gev/c)$ at $\sqrt{s} = 27.4$ *Gev*

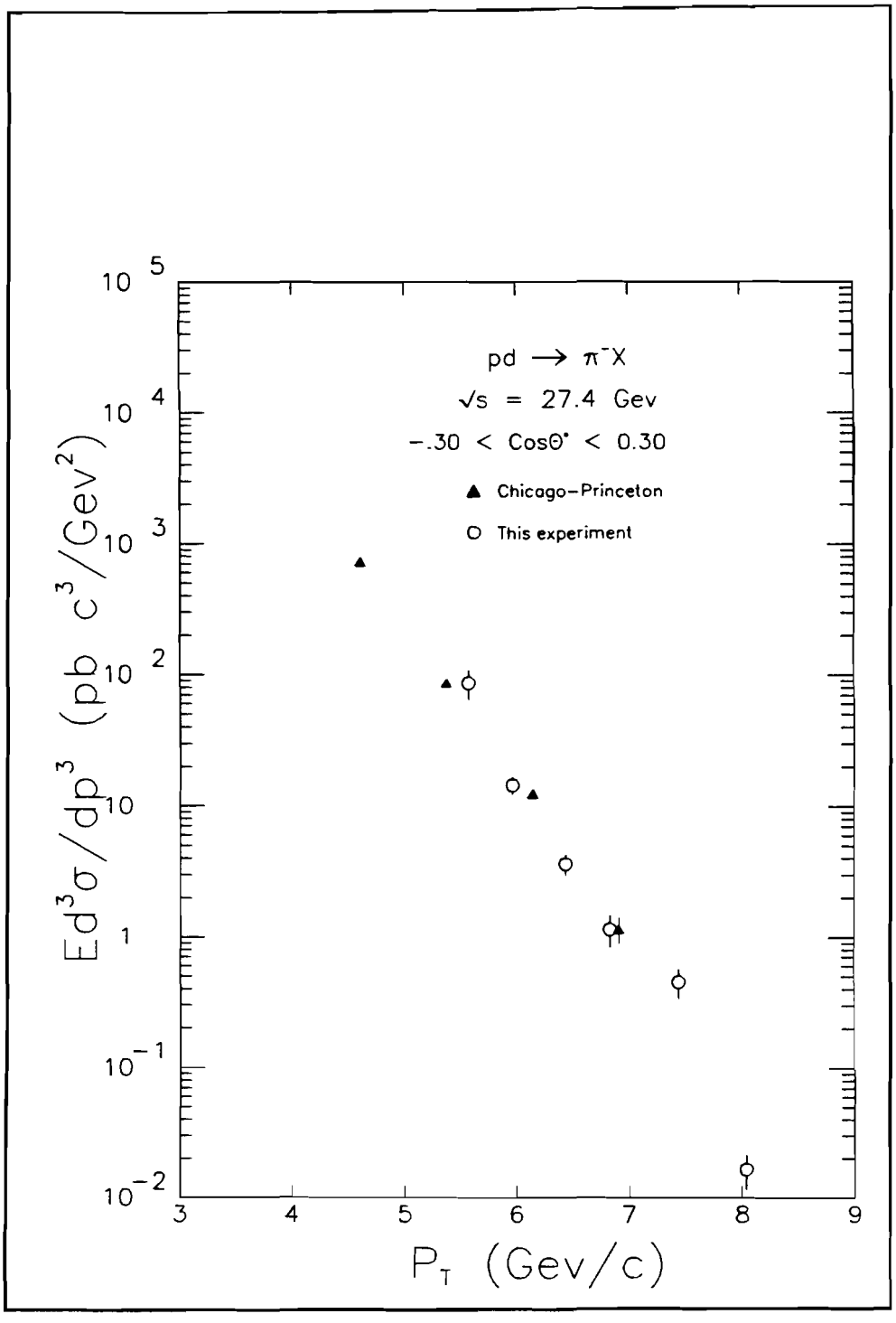

Figure 25. $E\frac{d^3\sigma}{dp^3}$ $(pd \rightarrow \pi^- \mathrm{X})$ *versus* $p_\perp(\mathrm{Gev/c})$ at $\sqrt{s} = 27.4$ *Gev*

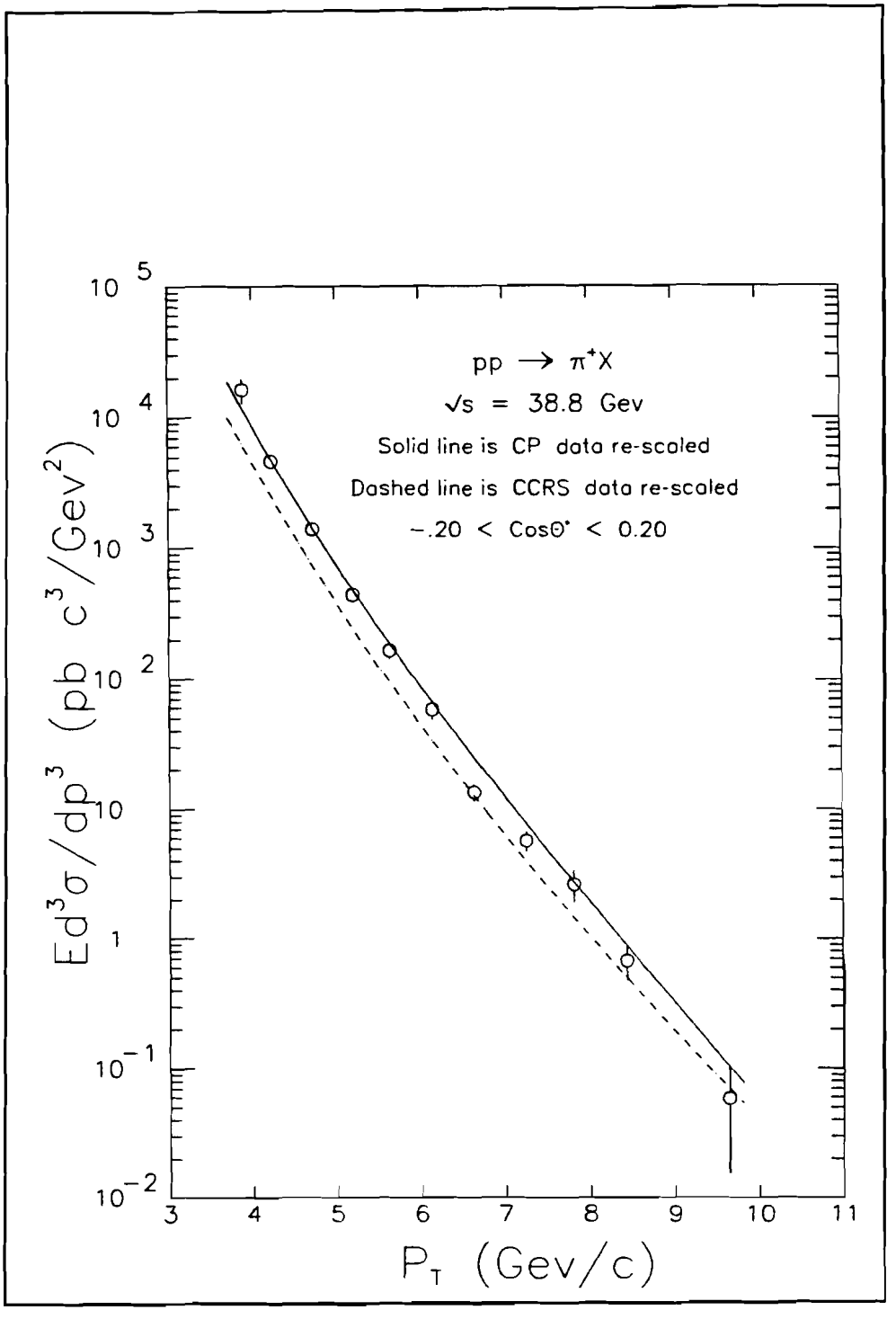

Figure 26. $E\frac{d^3\sigma}{dp^3}$ $(pp \rightarrow \pi^+ X)$ *versus* $p_\perp (Gev/c)$ at $\sqrt{s} = 38.8$ *Gev*

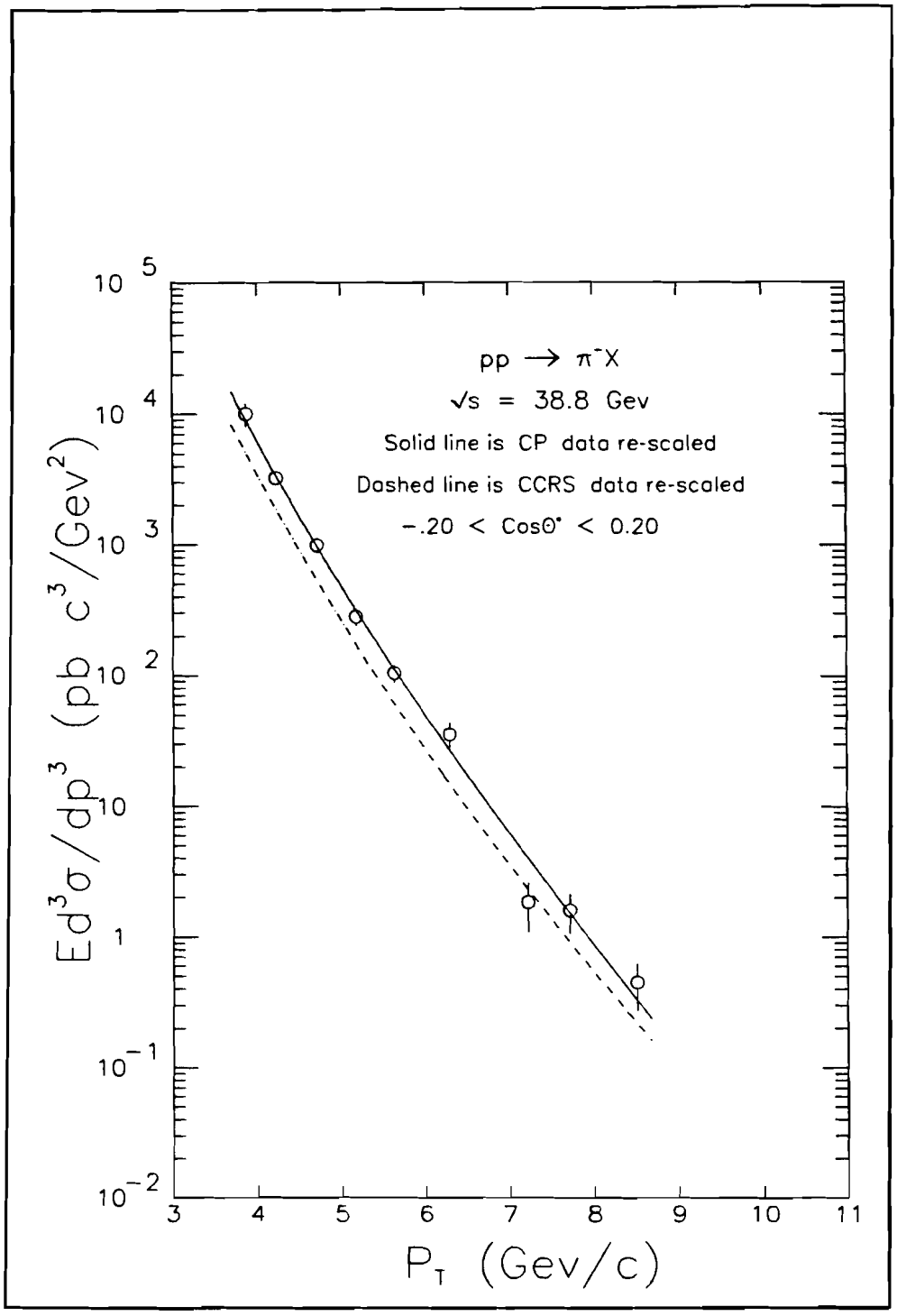

Figure 27. $E\frac{d^3\sigma}{dp^3}$ $(pp \rightarrow \pi^- X)$ *versus* $p_\perp (Gev/c)$ at $\sqrt{s} = 38.8$ *Gev*

or ratios with the statistical and systematic error. The estimated systematic uncertainty in the particle fractions is signed because the measurements are correlated. Also shown are the number of tracks for each $p_\perp$ bin and the mean $p_\perp$ for that set of tracks. In addition the particle ratios are shown in Figures 28-47 with the CP measurements and Lund monte carlo predictions,[51] which, as noted previously, can be considered to be a representation of e^+e^- measurements. The uncertainties shown in the figures are statistical only. To obtain the Lund model results for *pd* interactions, the predicted hadron production rates in *pn* and *pp* collisions were simply summed.

The K^+/π^+ measurements of this experiment are consistent with the results of CP; however, there is a marked discrepancy with the predictions of the Lund monte carlo. The mean K^+/π^+ for $p_\perp > 3$ *Gev/c* ratios are .49 ± .04, .47 ± .06 and .40 ± .04 measured in *pp* ($\sqrt{s} = 38.8$ *Gev*), *pp* ($\sqrt{s} = 27.4$ *Gev*) and *pd* ($\sqrt{s} = 27.4$ *Gev*) collisions, respectively, while the corresponding Lund predictions are .33 ± .02, .32 ± .02 and .32 ± .02. In the simplest view the K^+/π^+ ratio at high $p_\perp$ should reflect the relative probability of s and d quark production in the fragmentation chain, P(s)/P(d), which should be the same in *pp* and e^+e^- collisions. Apparently the Lund monte carlo does not correctly model the physical situation in either *pp*

[51] The standard PYTHIA version 4.2 and JETSET version 6.2 of the Lund program were used. In the figures the horizontal error bars on the Lund points show the bin width. In these versions, the strangeness suppression factor, P(s)/P(d), is .3 and the diquark suppression factor, P(qq)/P(q), is .1

or e^+e^- interactions. One explanation[52] of this discrepancy is that the production of some resonances decaying to pions is inadequately modelled by Lund. This biases the P(s)/P(d) determined in e^+e^- experiments to low z. High $x_\perp$ neutral pions have been shown[53] to carry a large fraction of the parton momentum, and, in particular, for $x_\perp > .15$ ($p_\perp > 3$ *Gev/c* at $\sqrt{s} = 38.8$ *Gev*), neutral pions carry at least 80% of the parton momentum; hence, the value of P(s)/P(d) measured in *pp* interactions should be biased towards high z. Further elucidation comes from semi-inclusive hadron production in $\mu p \rightarrow \mu h X$ by the European Muon Collaboration.[54] Their measured particle fractions, π^+/h^+ and K^+/h^+ versus x_F,[55] show that K^+/π^+ is approximately .45 at $x_F > .6$ thus independently confirming the hypothesis that high $p_\perp$ hadrons contain a large fraction of the momentum of the primary scattered parton.

Looking next to the proton to positive pion ratio, there is again relatively good agreement with the measurements of CP and disagreement with Lund. The Lund predictions are consistently higher than the measurements. Another observation, drawn from the $pp \rightarrow p/\pi^+$ *vs* $x_\perp$ plot in Figure 36, is the non-scaling behavior

---

[52] A. Seiden, "Comparison of Jet Fragmentation in Various Processes", Invited paper, 6th International Conference on Proton Antiproton Physics, Aachen, Germany, July 1986.

[53] A.L.S. Angelis et al., Nucl. Phys. B209, 284 (1975)

[54] M. Arneodo et al.,Phys. Lett. 150B, 458 (1985)

[55] x_F is defined as twice the longitudinal momentum of the final state hadron divided by the invariant mass of the total hadronic state; hence, in the forward hemisphere, it corresponds directly to the fragmentation variable, z.

of the ratio reflecting the supposition[56] that proton production may arise from the scattering of constituent diquarks which would show dependence on the Q^2 dependence of the diquark form factor. This hypothesis is strengthened by the better agreement of the ratios measured at $\sqrt{s} = 27.4$ and $\sqrt{s} = 38.8$ *Gev* plotted vs $p_\perp$ as in Figure 37 since it can be supposed that ${p_\perp}^2 \propto Q^2$. Finally the roughly constant value of the p/π^+ ratio of $.058 \pm .016$ for $p_\perp > 7$ *Gev/c* in the $\sqrt{s} = 38.8$ *Gev* data could be interpreted as the limit of the intrinsic diquark contribution and show the contribution to the proton yield from diquark–anti-diquark production in the fragmentation chain.

Turning to the negative particle ratios, the measurements of K^-/π^- *vs* $p_\perp$ shown in Figures 38-42 are generally compatible with both the Lund predictions and the CP measurements. When the $\sqrt{s} = 27.4$ and $\sqrt{s} = 38.8$ *Gev* $pp \rightarrow K^-/\pi^-$ measurements are viewed *vs* $x_\perp$ as in Figure 41 the x-dependence of the gluon structure function — generally considered to be the source of K^- at low $p_\perp$[57] — is visible. In addition, the average of the K^-/π^- ratios of $.095 \pm .032$ and $.093 \pm .032$ for $x_\perp > .35$ in the $\sqrt{s} = 27.4$ and $\sqrt{s} = 38.8$ *Gev* *pp* measurements are consistent with a QCD-based monte carlo of the Split Field Magnet (SFM) group[58] that predicts (at $\Theta^* \approx 50°$) $K^-/\pi^- \approx .11$ for $x_\perp > .35$.

Finally turning to the $\overline{p}/\pi^-$ ratios, all measurements appear

[56] S. Ekelin and S. Fredriksson, Phys. Lett., 149B, 509 (1984)
[57] A. Breakstone et al., Phys. Lett. 135B, 510 (1984)
[58] *Ibid.*

to be in relatively good agreement with the Lund predictions albeit with poor statistical precision. The $\sqrt{s} = 27.4$ *Gev* measurements, however, are not consistent with the previous results given by the Chicago-Princeton group.

Table 15: Like-sign Ratios $\sqrt{s} = 27.4$ *Gev* pp

$p_\perp$ bin *Gev/c*	$\langle p_\perp \rangle$ *Gev/c*	K^+/π^+	p/π^+	Tracks
5.2- 5.7	5.55	.418±.058±.003	.226±.042±.006	456
5.7- 6.2	5.94	.423±.037±.007	.236±.027±.004	1090
6.2- 6.7	6.41	.407±.047±.008	.133±.029±.004	567
6.7- 7.2	6.94	.383±.061±.017	.087±.033±.023	297
7.2- 7.7	7.40	.487±.127±.021	.208±.076±.011	107
7.7- 9.0	7.97	.725±.248±.230	—	52
		K^-/π^-	$\overline{p}/\pi^-$	
5.2- 5.7	5.57	.114±.034±.002	.165±.043±.005	239
5.7- 6.2	5.94	.125±.024±.005	.085±.024±.003	499
6.2- 6.7	6.41	.081±.025±.007	.042±.026±.003	244
6.7- 7.2	6.93	.095±.044±.014	—	99
7.2- 7.7	7.36	.058±.055±.014	.068±.058±.007	36

Table 16: Particle Fractions $\sqrt{s} = 27.4$ *Gev pp*

$p_\perp$ bin *Gev/c*	π^+	K^+	p
5.2- 5.7	.608 ±.040 ∓0.002	.254 ±.030 ∓0.000	.137 ±.023 ±0.002
5.7- 6.2	.603 ±.025 ∓0.002	.255 ±.019 ±0.002	.142 ±.015 ∓0.000
6.2- 6.7	.649 ±.036 ∓0.003	.264 ±.026 ±0.003	.086 ±.018 ±0.000
6.7- 7.2	.680 ±.051 ±0.004	.260 ±.035 ±0.007	.060 ±.022 ∓0.011
7.2- 7.7	.590 ±.080 ∓0.006	.287 ±.060 ±0.006	.123 ±.041 ∓0.000
7.7- 9.0	.565 ±.115 ∓0.061	.410 ±.103 ±0.068	.025 ±.051 ∓0.007

	π^-	K^-	$\overline{p}$
5.2- 5.7	.782 ±.061 ∓0.002	.089 ±.025 ∓0.000	.129 ±.030 ±0.002
5.7- 6.2	.826 ±.043 ∓0.002	.104 ±.019 ±0.002	.071 ±.019 ∓0.000
6.2- 6.7	.891 ±.063 ∓0.003	.072 ±.022 ±0.003	.037 ±.023 ∓0.000
6.7- 7.2	.910 ±.101 ±0.006	.086 ±.038 ±0.007	.004 ±.040 ∓0.013
7.2- 7.7	.888 ±.161 ∓0.006	.052 ±.047 ±0.006	.060 ±.049 ∓0.000
7.7- 9.0	.655 ±.287 ∓0.056	.184 ±.180 ±0.062	.161 ±.157 ∓0.006

Table 17: Like-sign Ratios $\sqrt{s} = 27.4$ *Gev pd*

$p_\perp$ bin Gev/c	$\langle p_\perp \rangle$ Gev/c	K^+/π^+	p/π^+	Tracks
5.2- 5.7	5.57	.440±.068±.003	.161±.045±.006	300
5.7- 6.2	5.97	.418±.033±.025	.132±.021±.014	1147
6.2- 6.7	6.43	.369±.035±.006	.140±.023±.003	796
6.7- 7.2	6.94	.374±.036±.016	.108±.019±.021	689
7.2- 7.7	7.40	.391±.050±.019	.089±.025±.009	398
7.7- 9.0	8.06	.429±.088±.186	.146±.048±.098	148
		K^-/π^-	$\overline{p}/\pi^-$	
5.2- 5.7	5.55	.079±.017±.002	.066±.020±.004	544
5.7- 6.2	5.95	.092±.012±.005	.067±.014±.003	1225
6.2- 6.7	6.42	.084±.015±.006	.023±.014±.003	622
6.7- 7.2	6.95	.078±.018±.011	—	420
7.2- 7.7	7.39	.028±.016±.013	—	188

Table 18: Particle Fractions $\sqrt{s} = 27.4$ *Gev pd*

$p_\perp$ bin Gev/c	π^+	K^+	p
5.2- 5.7	.625 ±.049 ∓0.002	.275 ±.036 ∓0.000	.100 ±.026 ±0.002
5.7- 6.2	.645 ±.025 ∓0.007	.270 ±.018 ±0.009	.085 ±.013 ∓0.002
6.2- 6.7	.663 ±.030 ∓0.002	.245 ±.020 ±0.002	.092 ±.014 ±0.000
6.7- 7.2	.675 ±.032 ±0.003	.252 ±.021 ±0.007	.073 ±.013 ∓0.011
7.2- 7.7	.676 ±.043 ∓0.006	.264 ±.028 ±0.006	.060 ±.016 ∓0.000
7.7- 9.0	.635 ±.068 ∓0.056	.272 ±.046 ±0.062	.093 ±.029 ∓0.006
	π^-	K^-	$\overline{p}$
5.2- 5.7	.873 ±.042 ∓0.002	.069 ±.014 ∓0.000	.057 ±.017 ±0.002
5.7- 6.2	.863 ±.028 ∓0.002	.079 ±.010 ±0.002	.058 ±.011 ∓0.000
6.2- 6.7	.903 ±.039 ∓0.003	.076 ±.013 ±0.002	.021 ±.012 ±0.000
6.7- 7.2	.920 ±.048 ±0.003	.072 ±.016 ±0.007	.007 ±.014 ∓0.010
7.2- 7.7	.968 ±.073 ∓0.006	.027 ±.015 ±0.006	.004 ±.017 ∓0.000
7.7- 9.0	.931 ±.138 ∓0.059	.028 ±.029 ±0.066	.041 ±.040 ∓0.007

Table 19: Like-sign Ratios $\sqrt{s} = 38.8$ Gev pp

$p_\perp$ bin Gev/c	$\langle p_\perp \rangle$ Gev/c	K^+/π^+	p/π^+	Tracks
3.6- 4.0	3.87	.530±.041±.014	.355±.030±.010	1362
4.0- 4.5	4.23	.481±.023±.013	.206±.016±.009	3259
4.5- 5.0	4.71	.470±.034±.005	.163±.022±.003	1403
5.0- 5.5	5.22	.559±.057±.004	.110±.029±.004	584
5.5- 6.0	5.76	.433±.045±.006	.105±.023±.004	595
6.0- 6.5	6.27	.484±.036±.007	.084±.014±.004	1018
6.5- 7.0	6.73	.467±.035±.019	.050±.011±.011	993
7.0- 7.5	7.24	.562±.051±.036	.095±.018±.023	699
7.5- 8.0	7.74	.447±.050±.033	.053±.015±.017	514
8.0- 9.0	8.42	.453±.051±.112	.064±.017±.058	528
9.0-11.0	9.60	.494±.099±.147	.021±.015±.075	171
		K^-/π^-	$\overline{p}/\pi^-$	
3.6- 4.0	3.87	.296±.029±.010	.063±.021±.007	939
4.0- 4.5	4.23	.279±.019±.010	.051±.014±.007	2019
4.5- 5.0	4.71	.270±.027±.004	—	836
5.0- 5.5	5.22	.175±.029±.003	.030±.017±.003	374
5.5- 6.0	5.79	.172±.029±.004	—	379
6.0- 6.5	6.25	.138±.023±.001	.016±.009±.001	437
6.5- 7.0	6.72	.104±.022±.014	—	380
7.0- 7.5	7.23	.145±.032±.026	—	266
7.5- 8.0	7.73	.081±.026±.039	.033±.016±.020	223
8.0- 9.0	8.39	.087±.031±.084	—	233
9.0-11.0	9.46	.061±.049±.103	—	61

Table 20: Particle Fractions $\sqrt{s} = 38.8$ Gev pp

$p_\perp$ bin Gev/c	π^+	K^+	p
3.6- 4.0	.531 ±.022 ∓0.004	.281 ±.018 ±0.003	.188 ±.014 ±0.001
4.0- 4.5	.593 ±.015 ∓0.004	.285 ±.012 ±0.003	.122 ±.009 ±0.001
4.5- 5.0	.612 ±.022 ∓0.001	.288 ±.017 ±0.002	.100 ±.013 ∓0.000
5.0- 5.5	.599 ±.034 ∓0.002	.335 ±.027 ±0.000	.066 ±.017 ±0.000
5.5- 6.0	.650 ±.035 ∓0.002	.281 ±.024 ±0.002	.068 ±.014 ∓0.000
6.0- 6.5	.638 ±.026 ∓0.002	.309 ±.019 ±0.003	.054 ±.009 ∓0.001
6.5- 7.0	.659 ±.027 ∓0.005	.308 ±.019 ±0.007	.033 ±.007 ∓0.002
7.0- 7.5	.604 ±.031 ∓0.012	.339 ±.024 ±0.010	.057 ±.010 ±0.002
7.5- 8.0	.667 ±.038 ∓0.011	.298 ±.027 ±0.011	.035 ±.010 ±0.000
8.0- 9.0	.659 ±.037 ∓0.035	.299 ±.027 ±0.039	.042 ±.011 ∓0.003
9.0-11.0	.660 ±.067 ∓0.047	.326 ±.051 ±0.050	.014 ±.010 ∓0.002

	π^-	K^-	$\overline{p}$
3.6- 4.0	.736 ±.030 ∓0.004	.218 ±.019 ±0.003	.047 ±.015 ±0.001
4.0- 4.5	.752 ±.021 ∓0.004	.210 ±.013 ±0.003	.038 ±.010 ±0.001
4.5- 5.0	.779 ±.032 ∓0.001	.210 ±.019 ±0.002	.011 ±.015 ∓0.000
5.0- 5.5	.830 ±.049 ∓0.002	.145 ±.022 ±0.000	.025 ±.014 ±0.000
5.5- 6.0	.853 ±.049 ∓0.001	.146 ±.023 ±0.002	.001 ±.022 ∓0.000
6.0- 6.5	.867 ±.045 ±0.000	.119 ±.018 ±0.000	.014 ±.008 ∓0.000
6.5- 7.0	.900 ±.050 ∓0.005	.094 ±.018 ±0.007	.007 ±.007 ∓0.002
7.0- 7.5	.873 ±.059 ∓0.012	.126 ±.026 ±0.010	.001 ±.023 ±0.002
7.5- 8.0	.898 ±.065 ∓0.018	.073 ±.022 ±0.017	.029 ±.015 ±0.000
8.0- 9.0	.913 ±.065 ∓0.037	.080 ±.027 ±0.040	.007 ±.016 ∓0.004
9.0-11.0	.940 ±.127 ∓0.047	.057 ±.045 ±0.050	.003 ±.028 ∓0.002

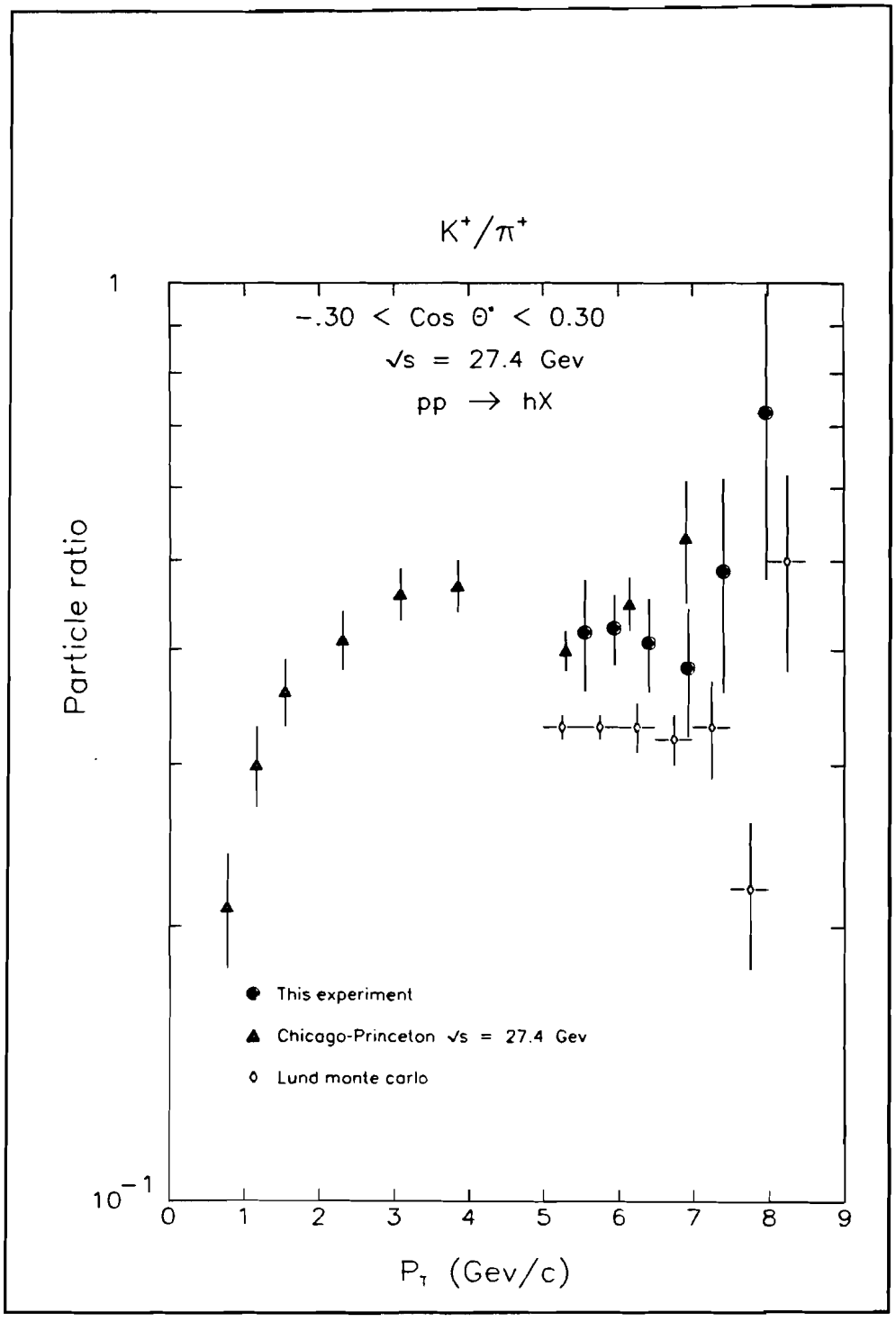

Figure 28. K^+/π^+ ratio *versus* $p_\perp$ in pp at $\sqrt{s} = 27.4$ *Gev*

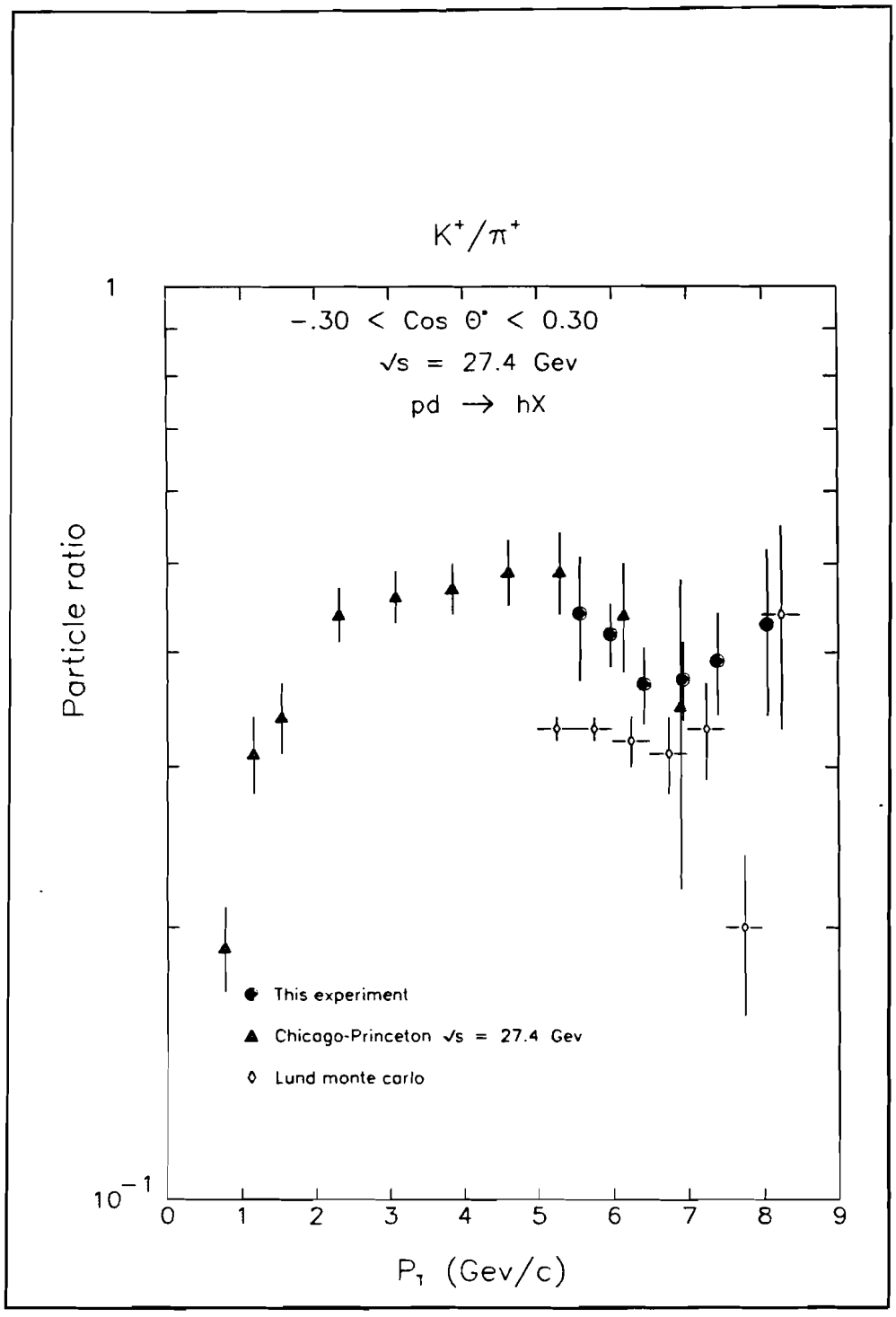

Figure 29. K^+/π^+ ratio *versus* $p_\perp$ in *pd* at $\sqrt{s} = 27.4$ *Gev*

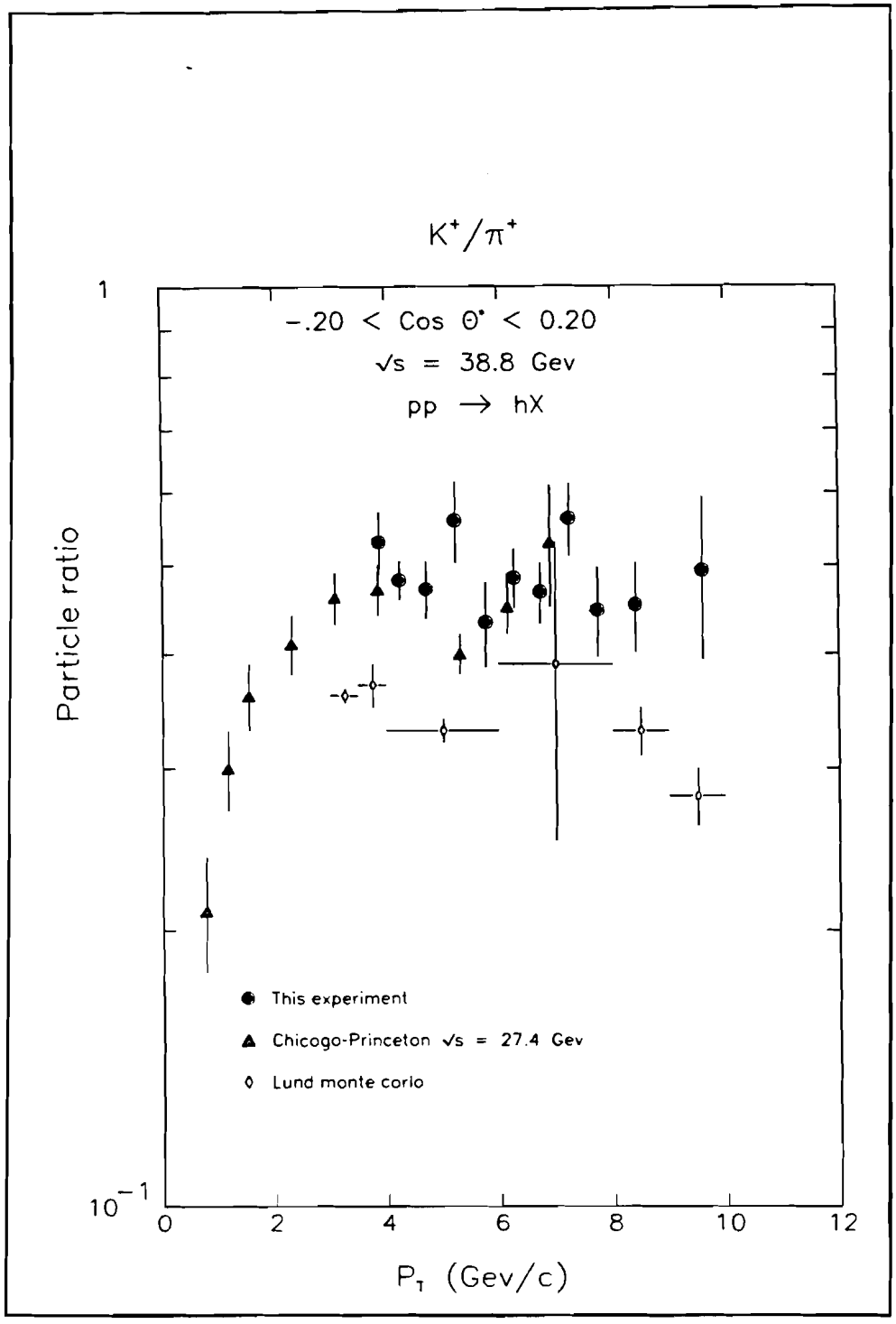

Figure 30. K^+/π^+ ratio *versus* $p_\perp$ in pp at $\sqrt{s} = 38.8$ *Gev*

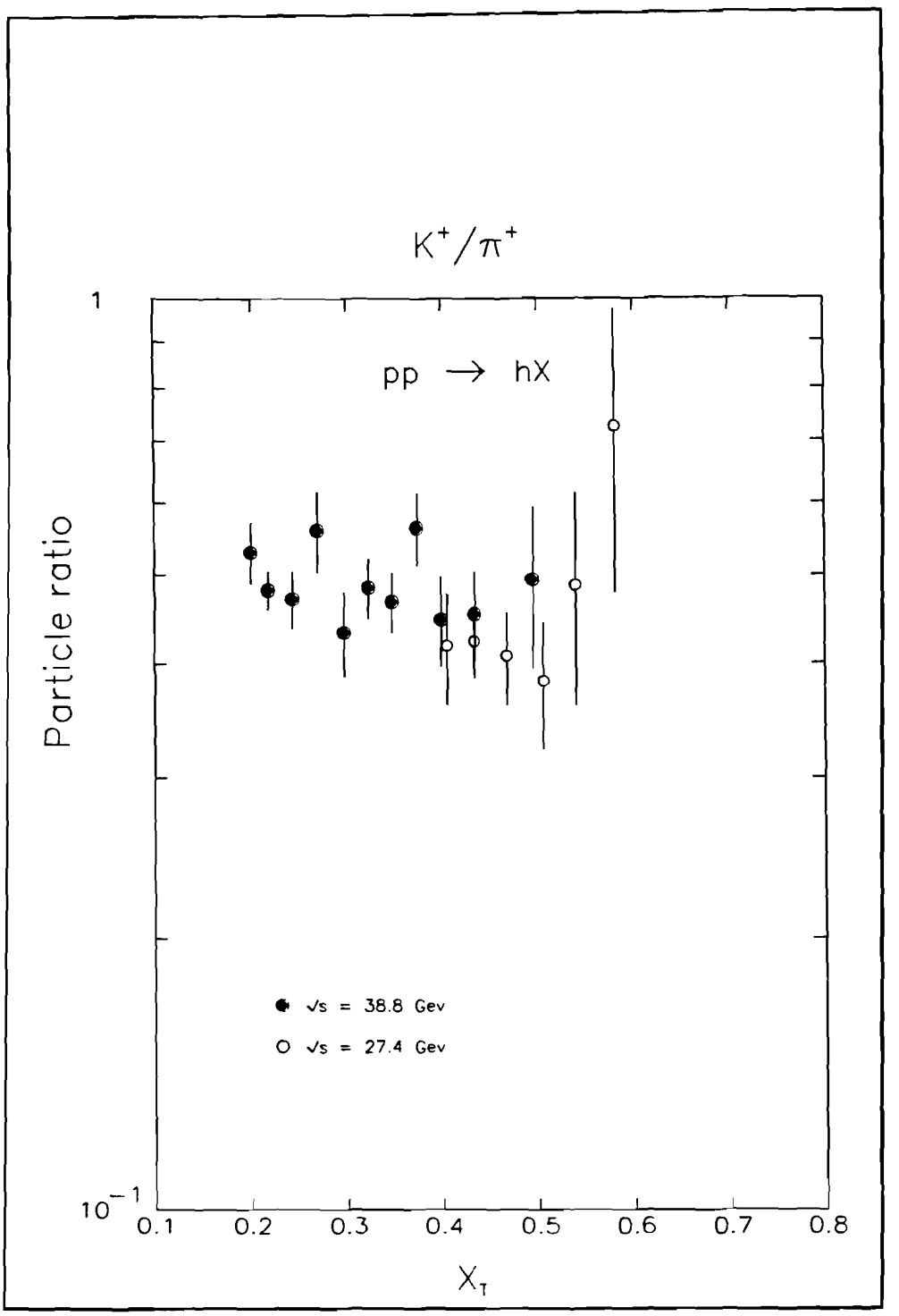

Figure 31. K^+/π^+ ratio *versus* $x_\perp$ in *pp* at $\sqrt{s} = 27.4$ & 38.8 *Gev*

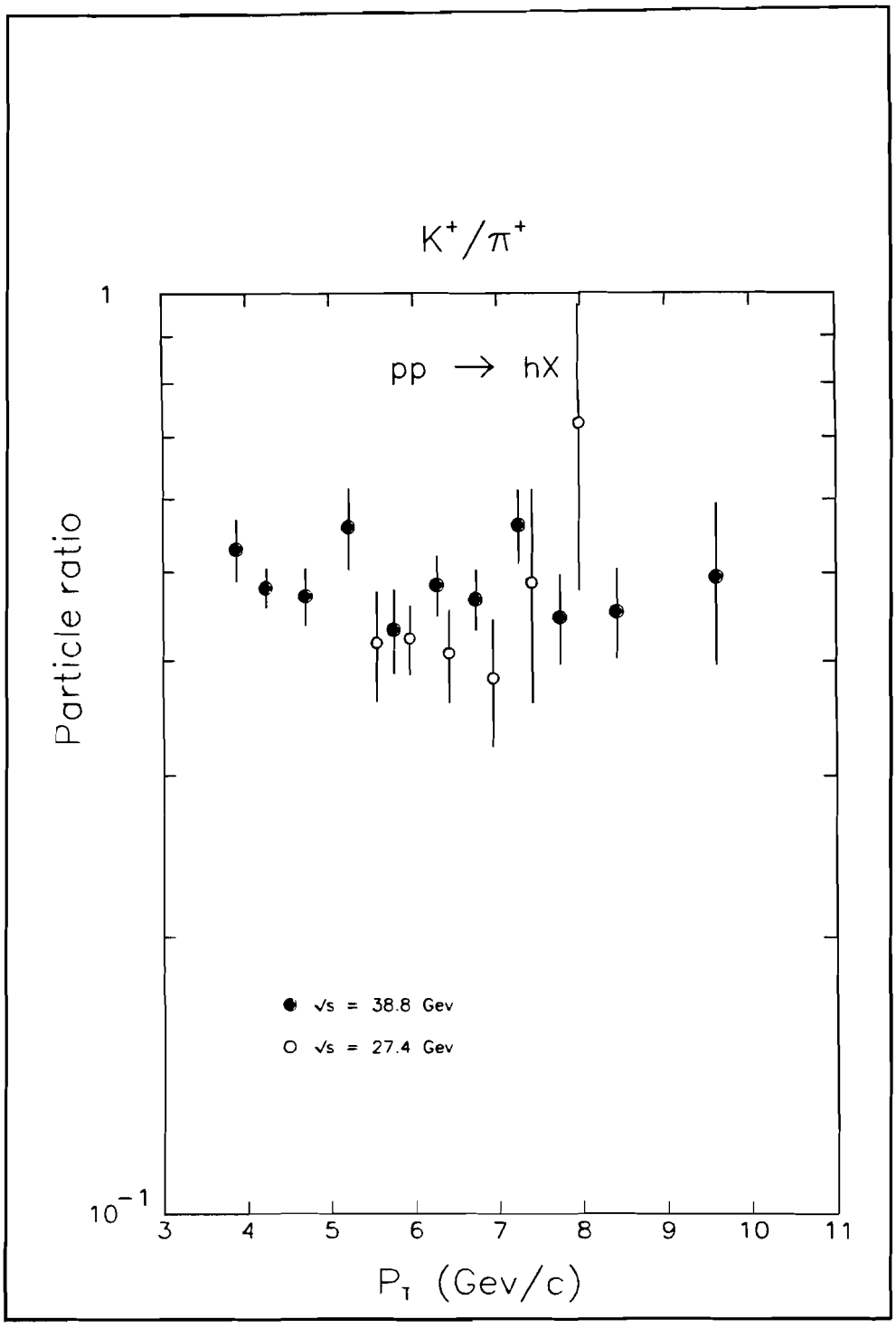

Figure 32. K^+/π^+ ratio *versus* $p_\perp$ in *pp* at $\sqrt{s} = 27.4$ & 38.8 *Gev*

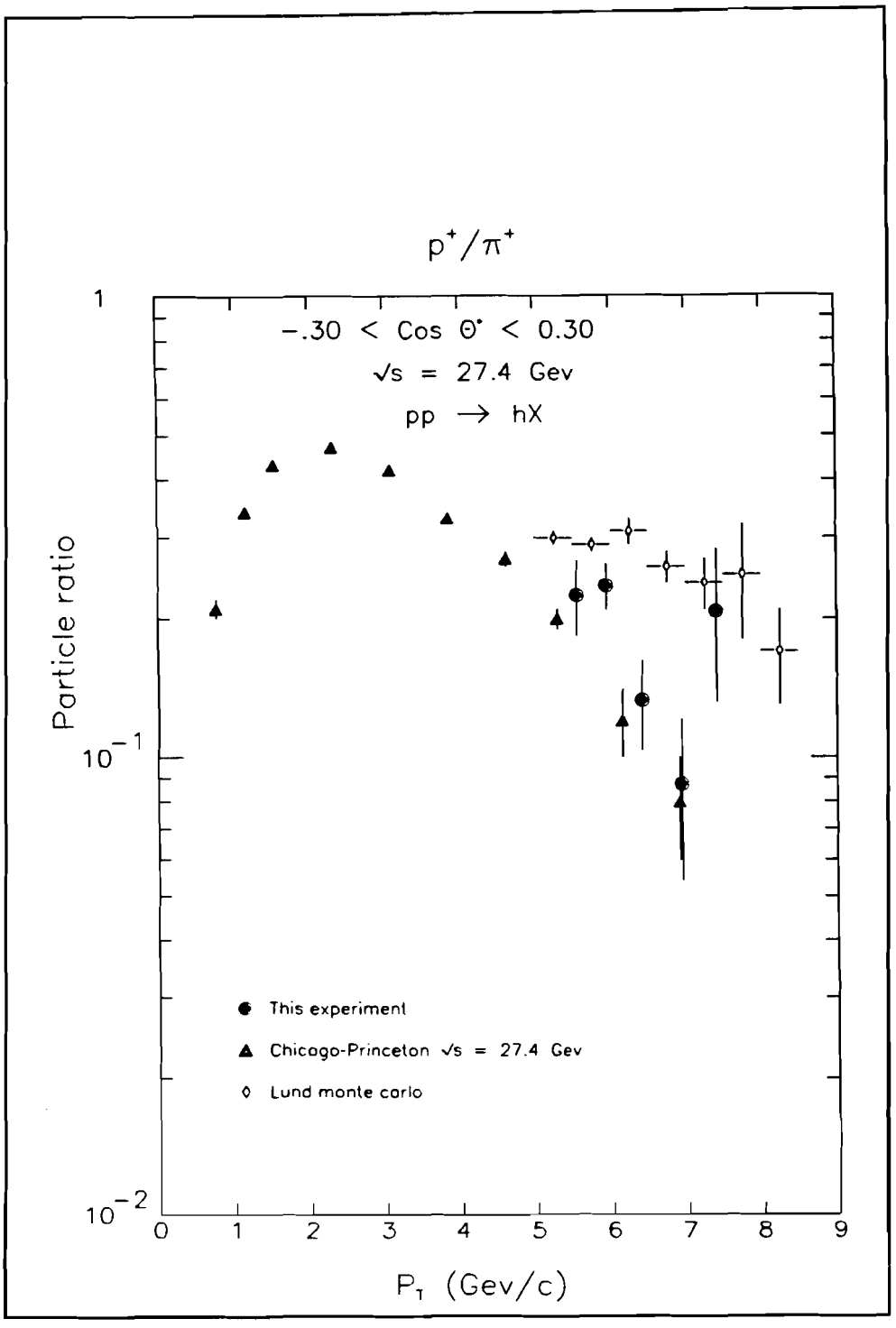

Figure 33. p/π^+ ratio *versus* $p_\perp$ in pp at $\sqrt{s} = 27.4$ *Gev*

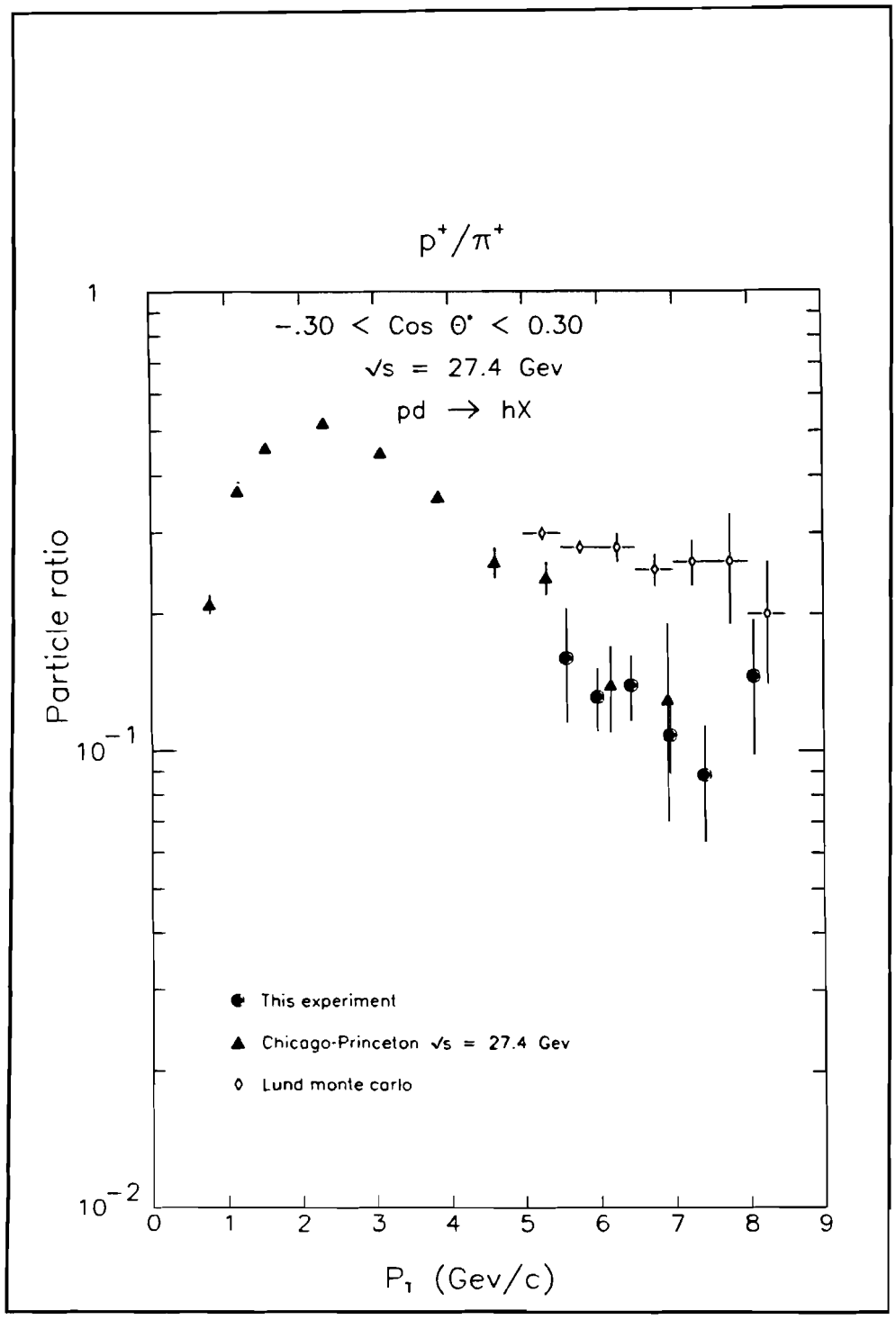

Figure 34. p/π^+ ratio *versus* $p_\perp$ in pd at $\sqrt{s} = 27.4$ Gev

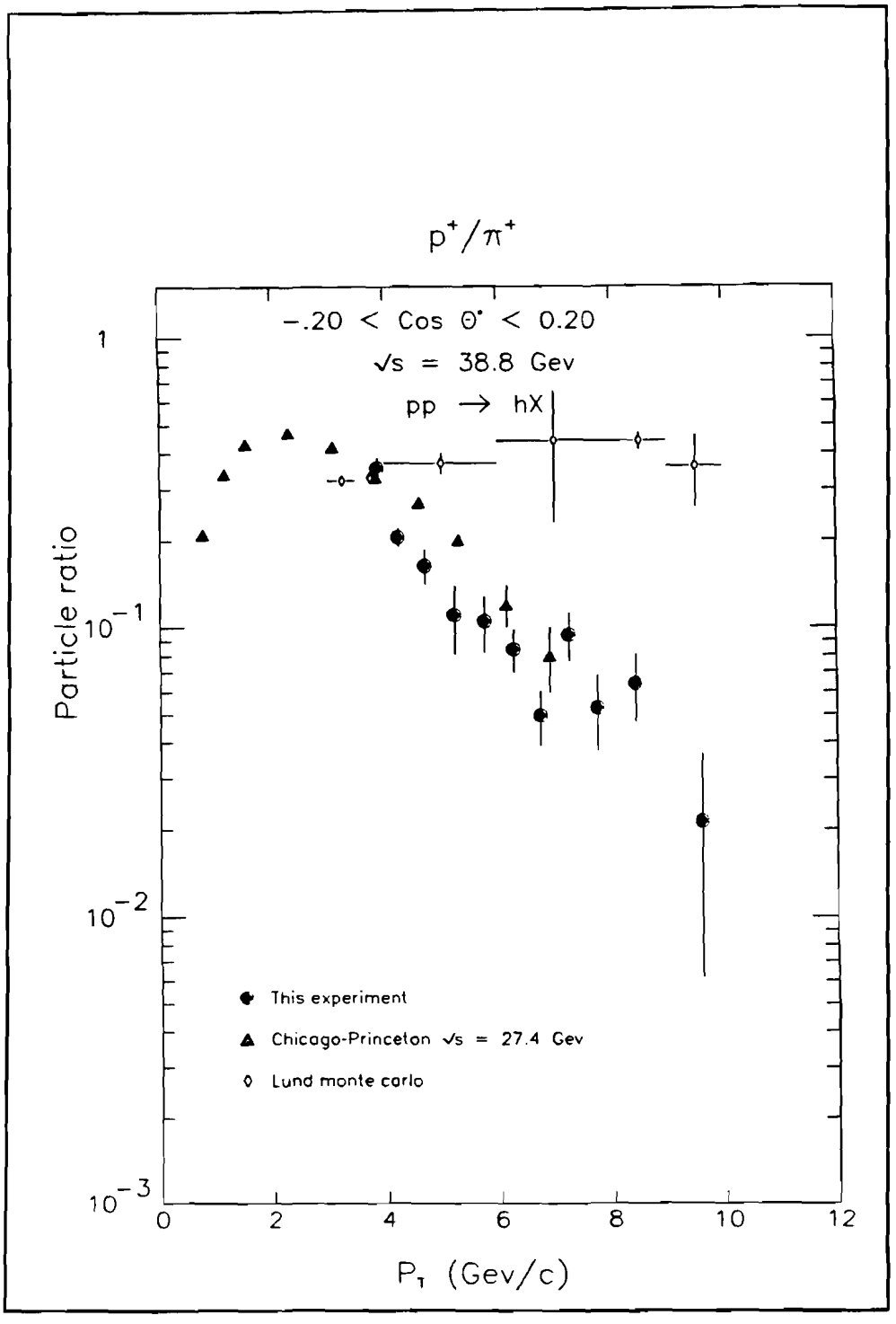

Figure 35. p/π^+ ratio *versus* $p_\perp$ in pp at $\sqrt{s} = 38.8$ *Gev*

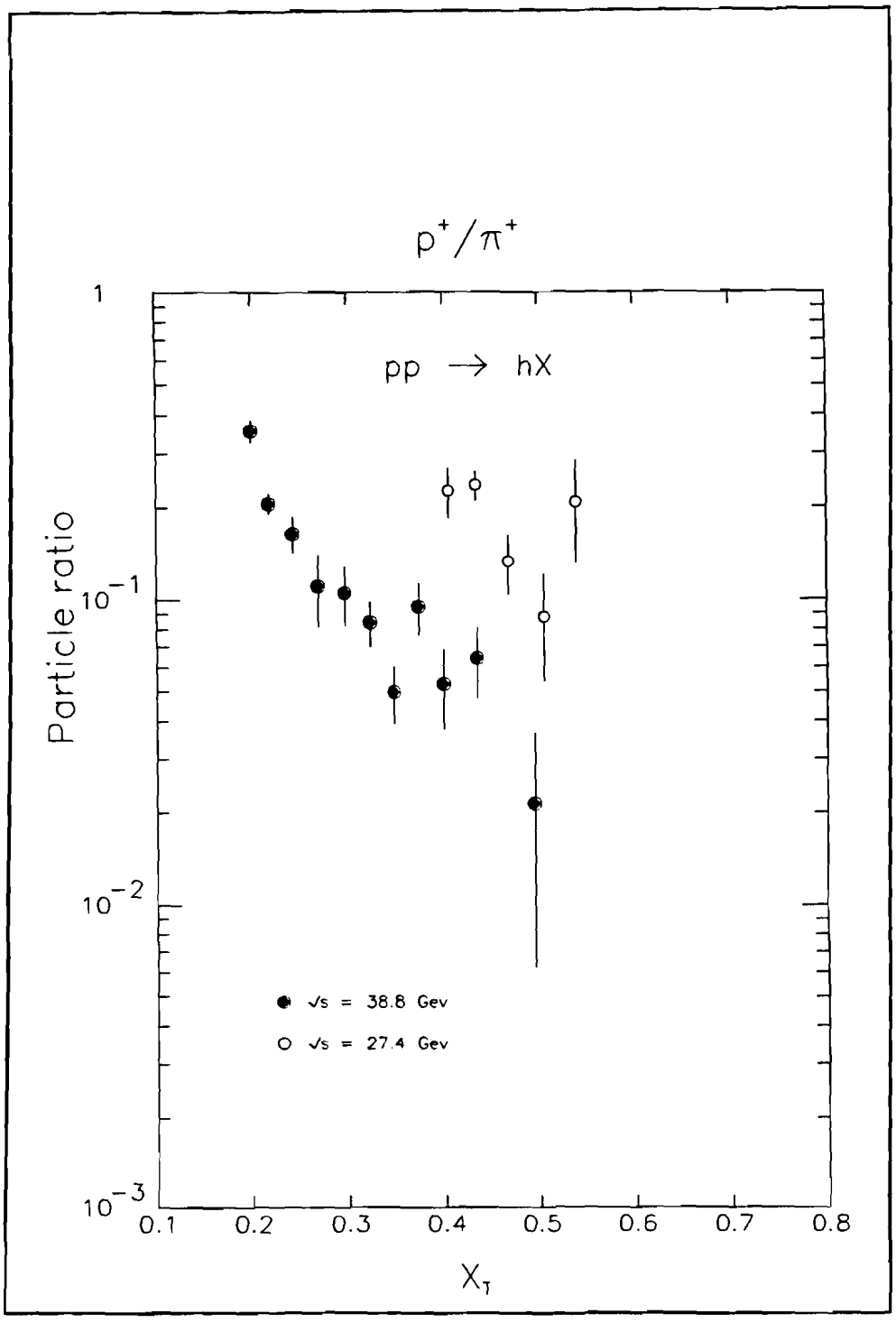

Figure 36. p/π^+ ratio *versus* $x_\perp$ in pp at $\sqrt{s} = 27.4$ & 38.8 Gev

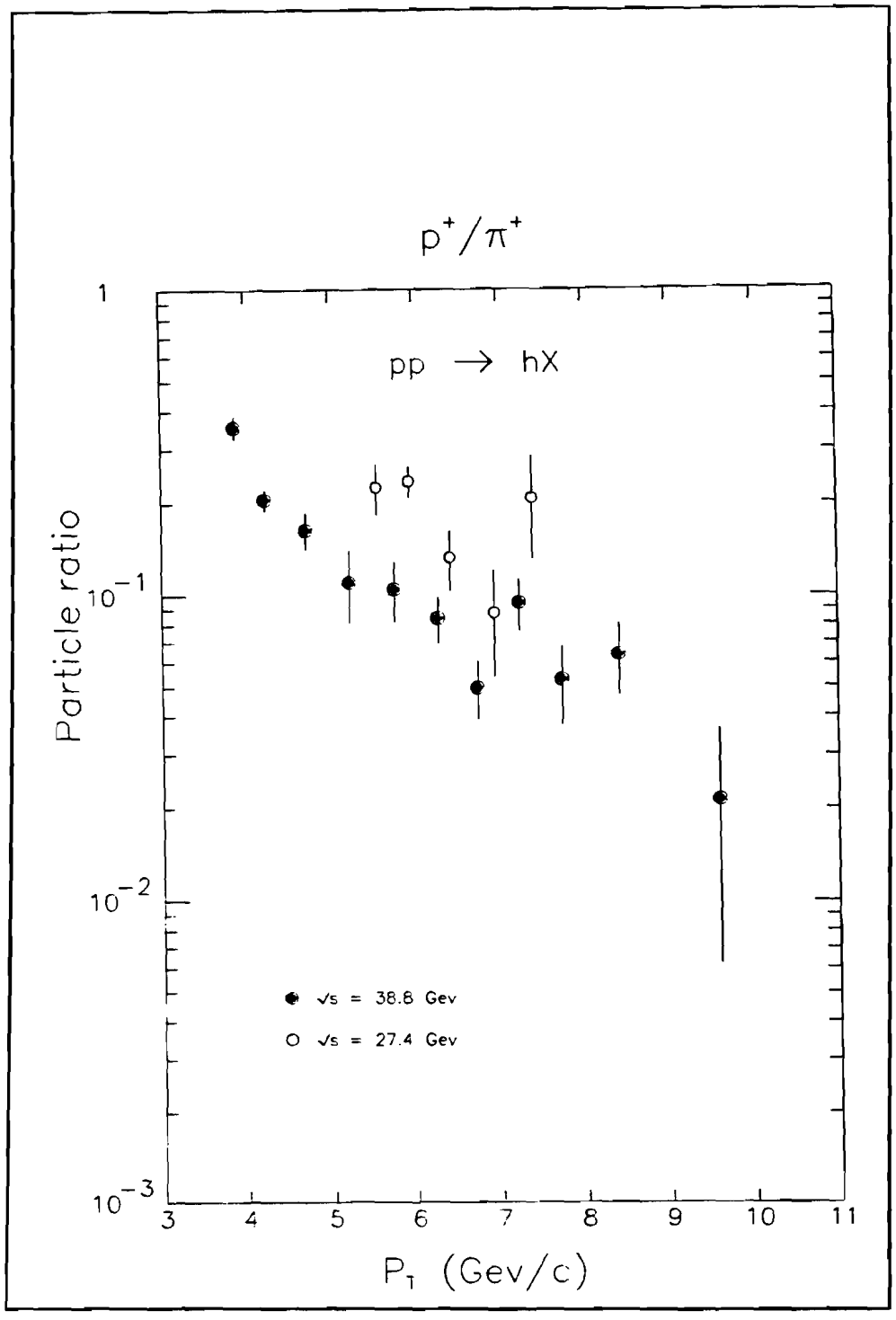

Figure 37. p/π^+ ratio *versus* $p_\perp$ in pp at $\sqrt{s} = 27.4$ & 38.8 *Gev*

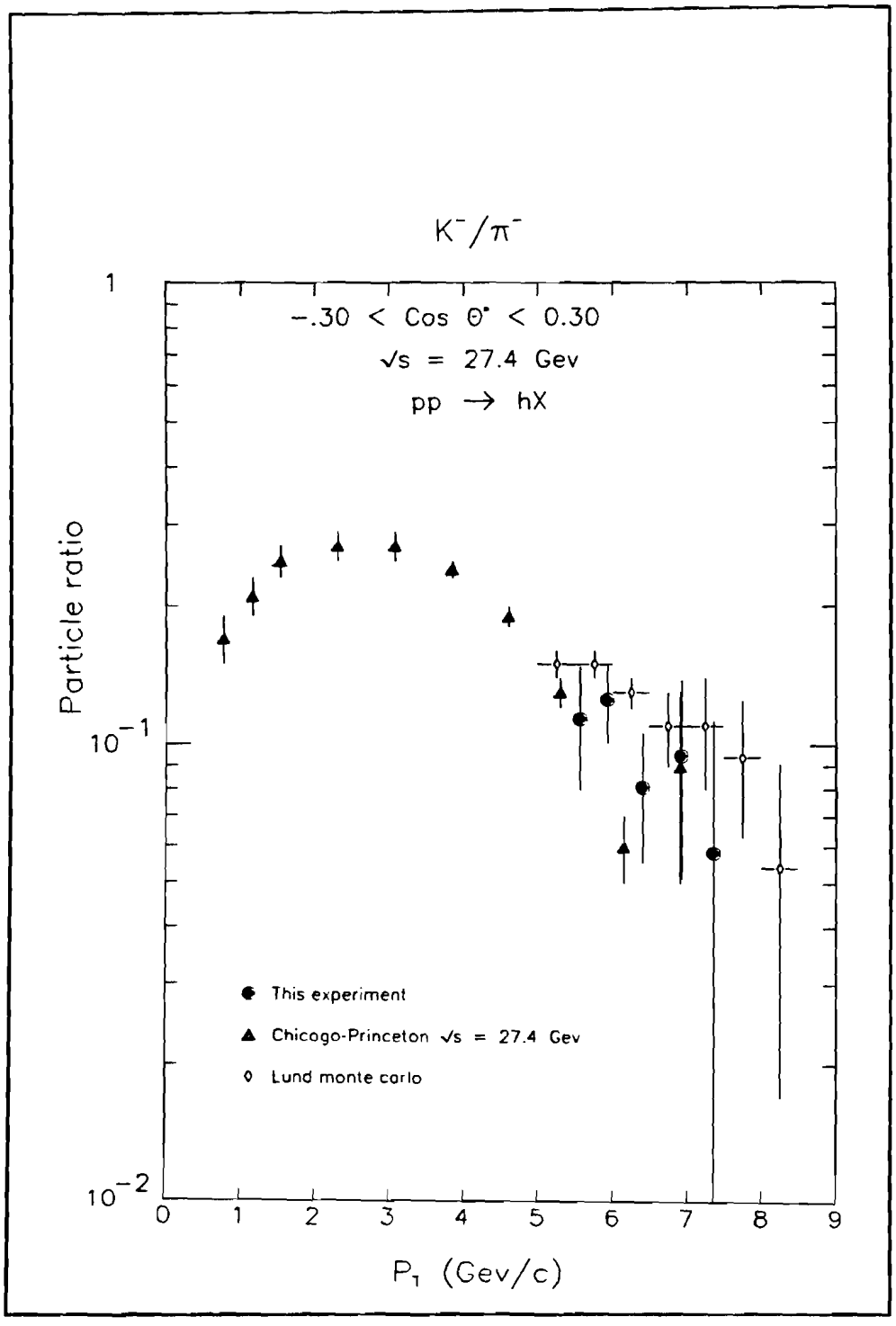

Figure 38. K^-/π^- ratio *versus* $p_\perp$ in pp at $\sqrt{s} = 27.4$ *Gev*

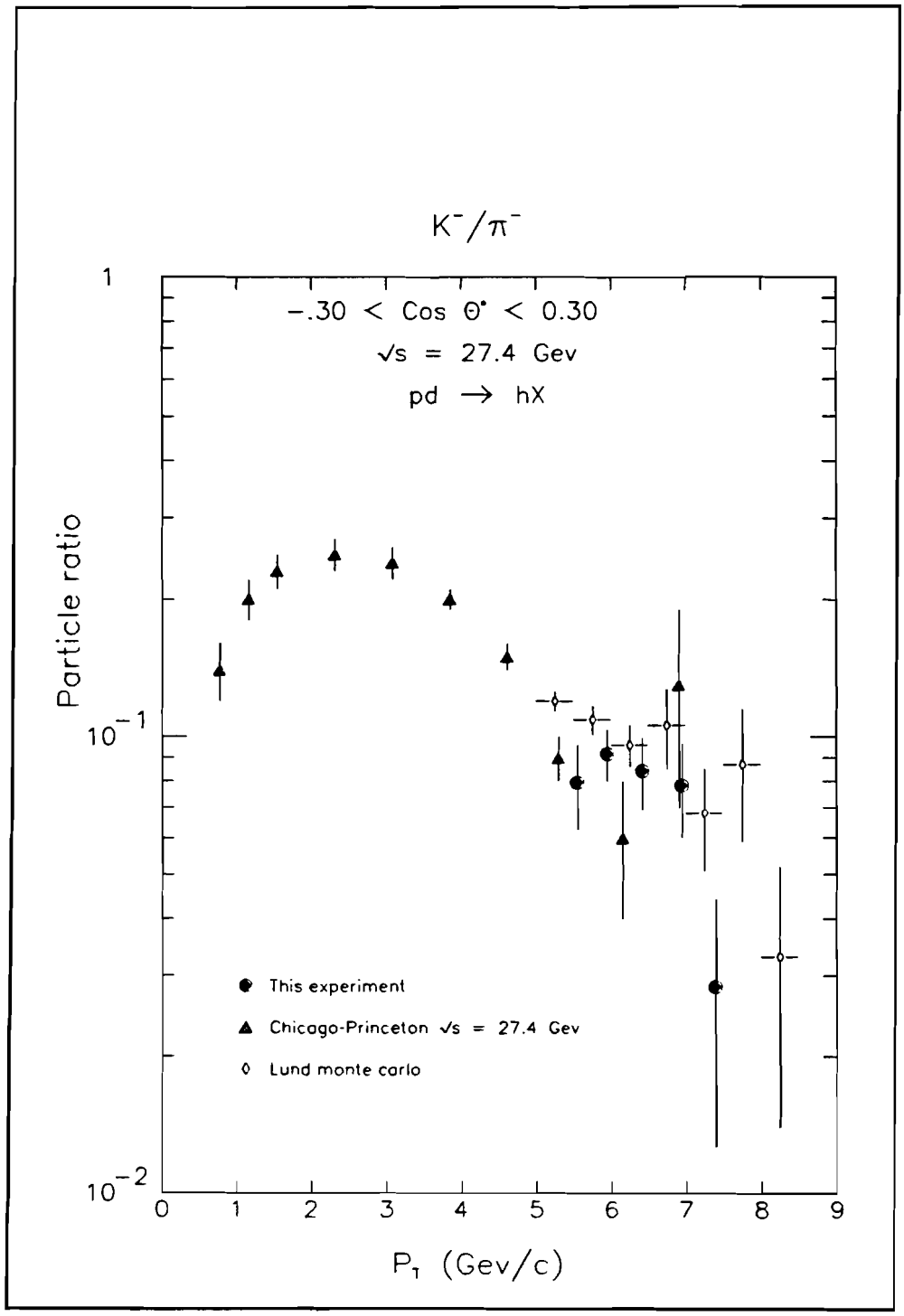

Figure 39. K^-/π^- ratio *versus* $p_\perp$ in *pd* at $\sqrt{s} = 27.4$ Gev

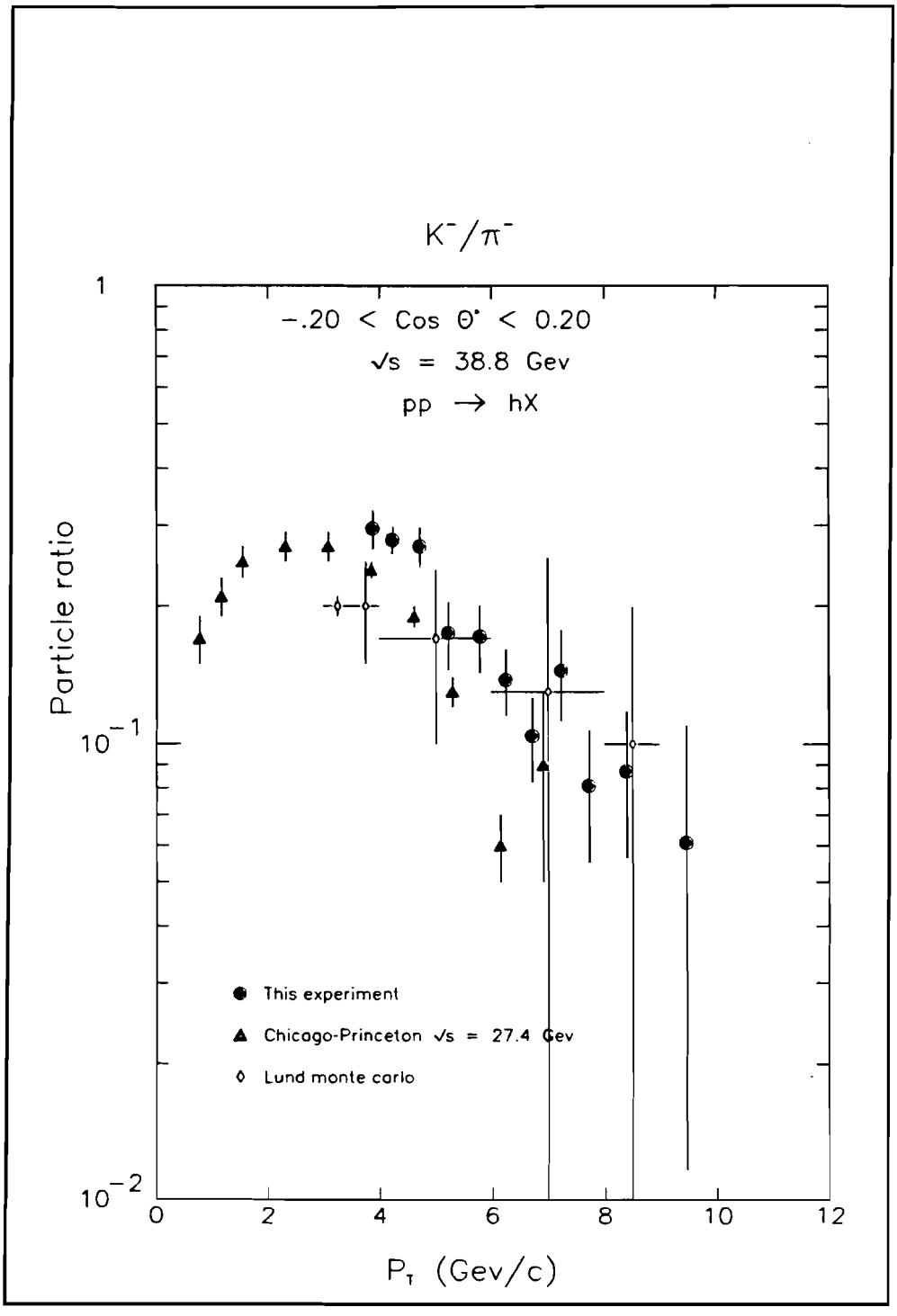

Figure 40. K^-/π^- ratio *versus* $p_\perp$ in pp at $\sqrt{s} = 38.8$ *Gev*

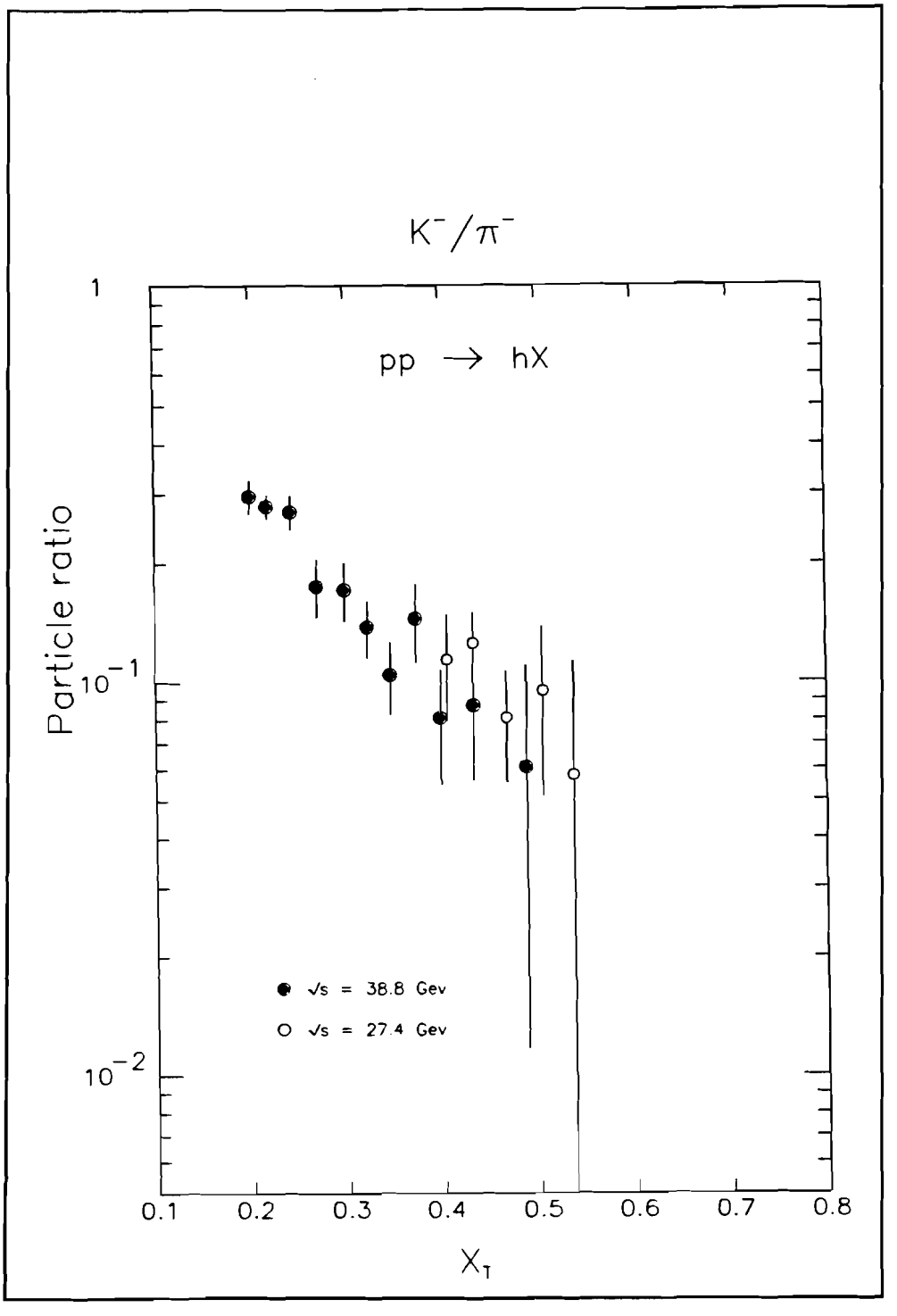

Figure 41. K^-/π^- ratio *versus* $x_\perp$ in *pp* at $\sqrt{s} = 27.4$ & 38.8 *Gev*

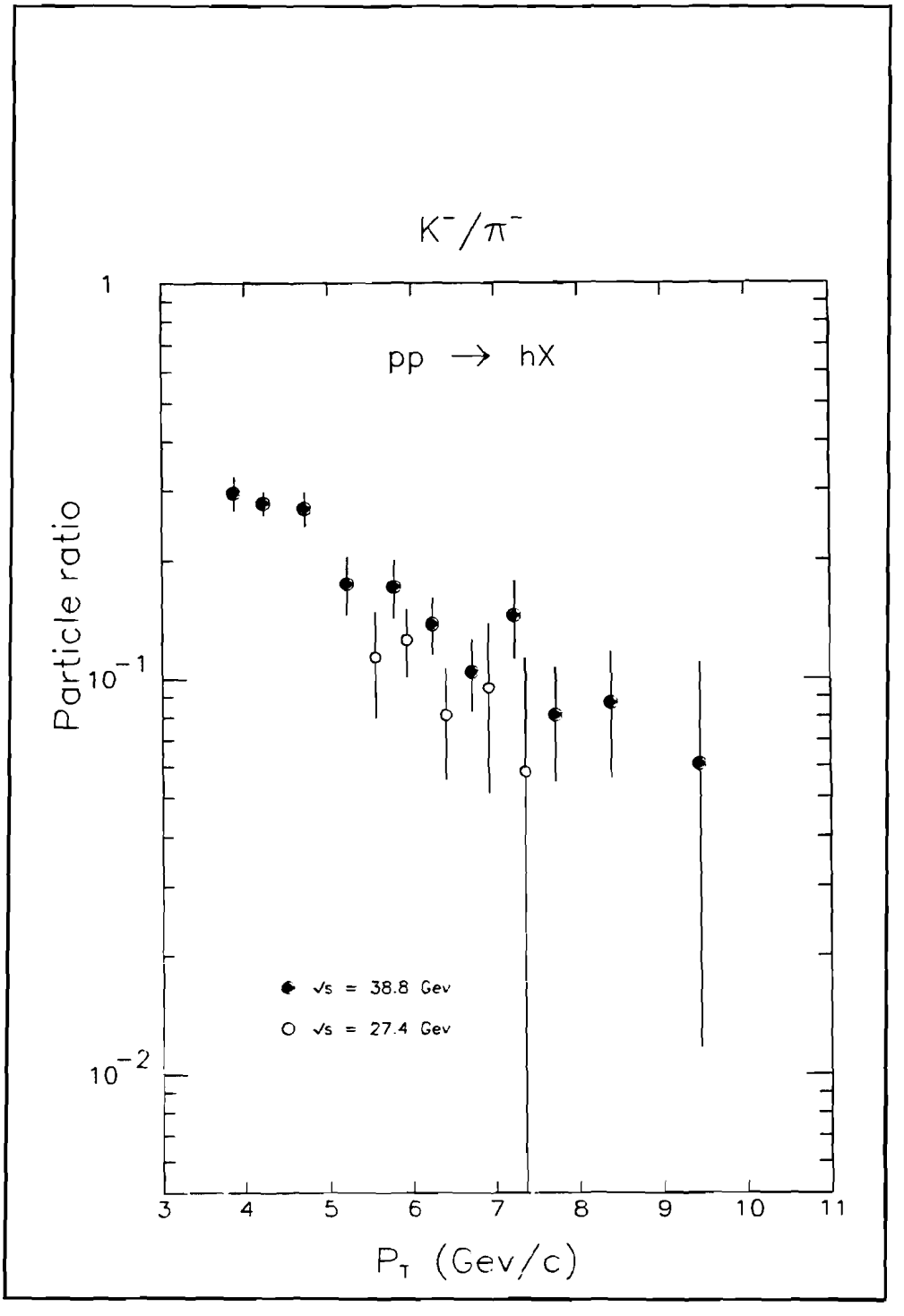

Figure 42. K^-/π^- ratio *versus* $p_\perp$ in *pp* at $\sqrt{s} = 27.4$ & 38.8 *Gev*

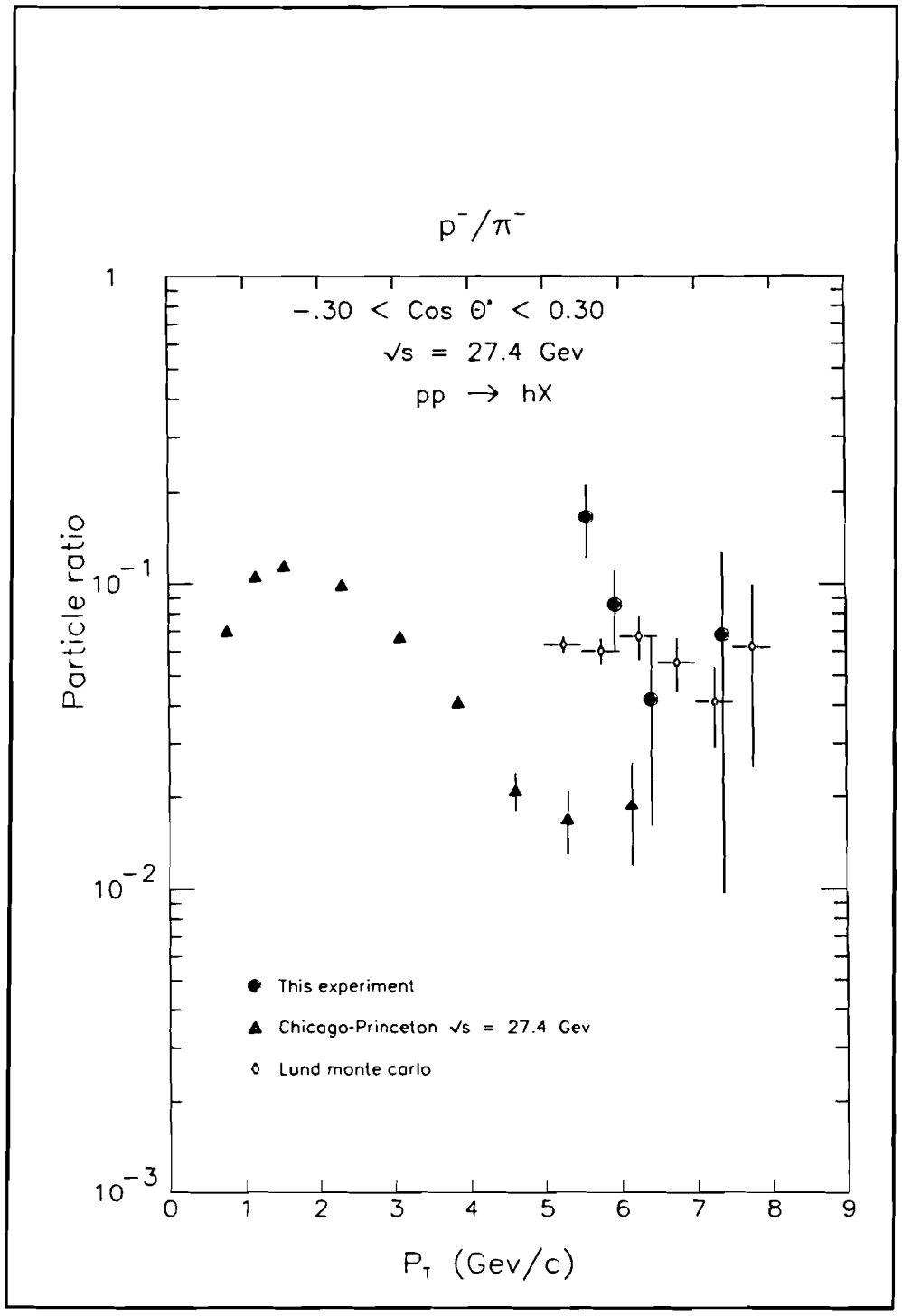

Figure 43. $\bar{p}/\pi^-$ ratio *versus* $p_\perp$ in pp at $\sqrt{s} = 27.4$ *Gev*

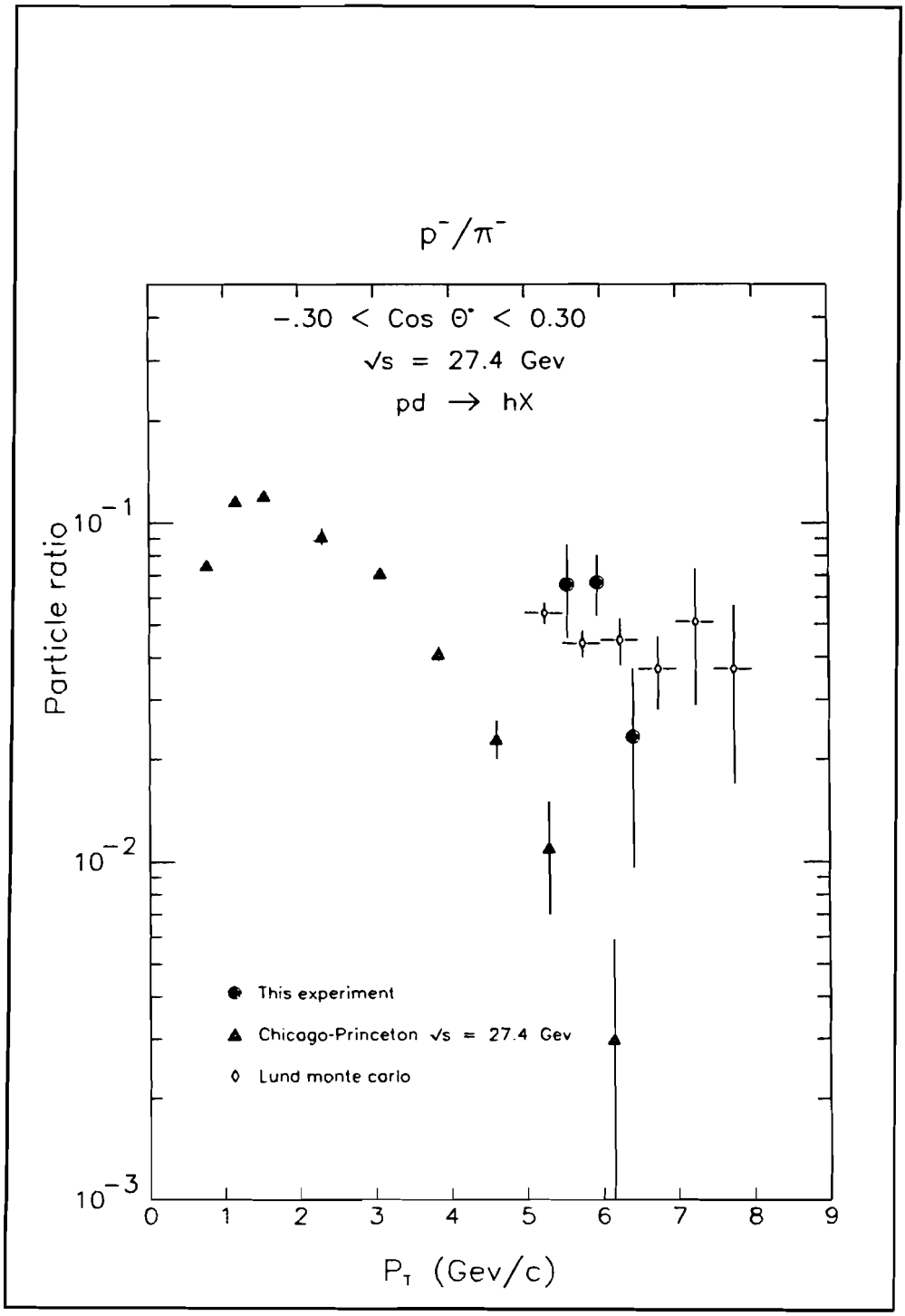

Figure 44. $\bar{p}/\pi^-$ ratio *versus* $p_\perp$ in *pd* at $\sqrt{s} = 27.4$ *Gev*

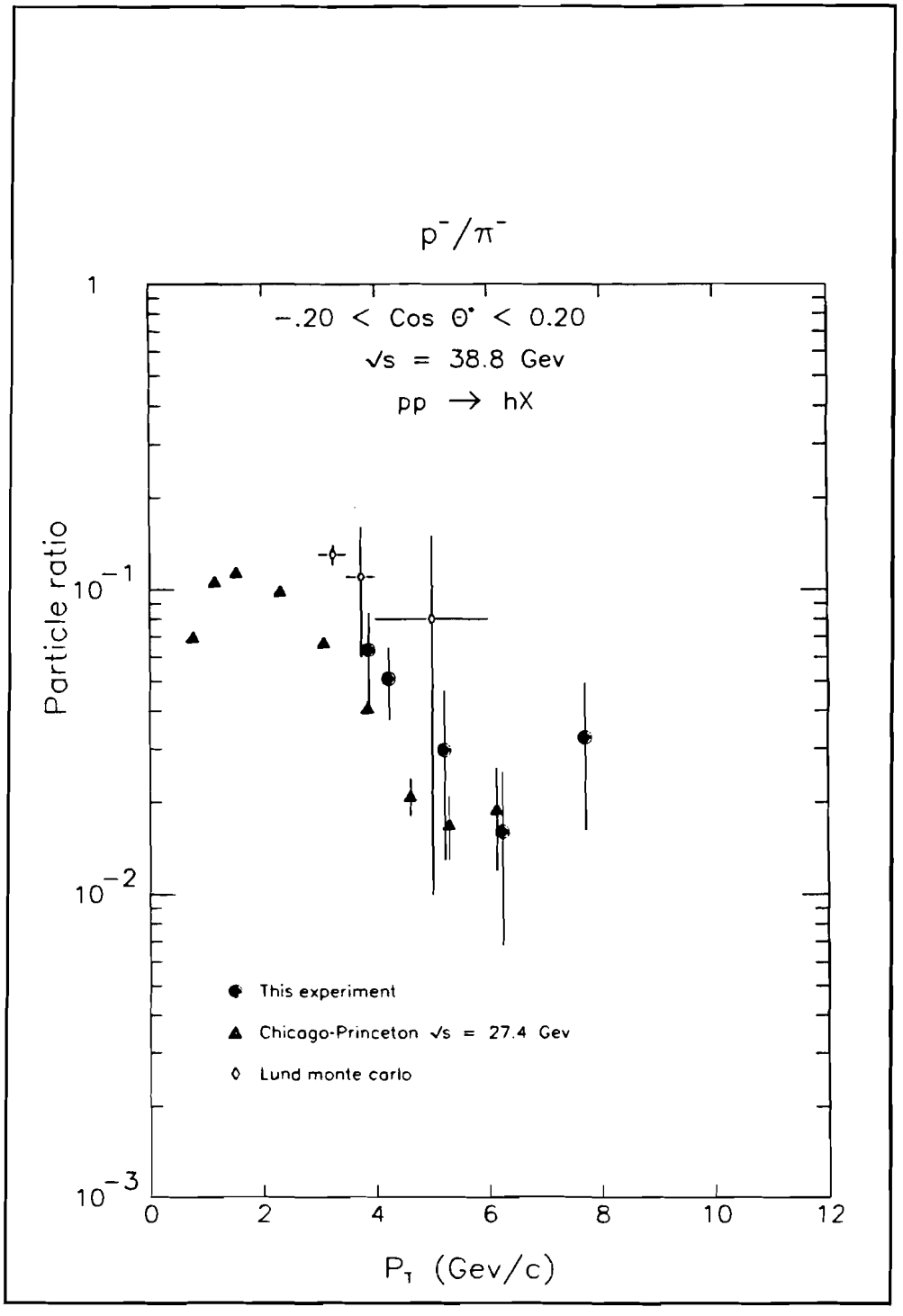

Figure 45. $\bar{p}/\pi^-$ ratio *versus* $p_\perp$ in pp at $\sqrt{s} = 38.8$ *Gev*

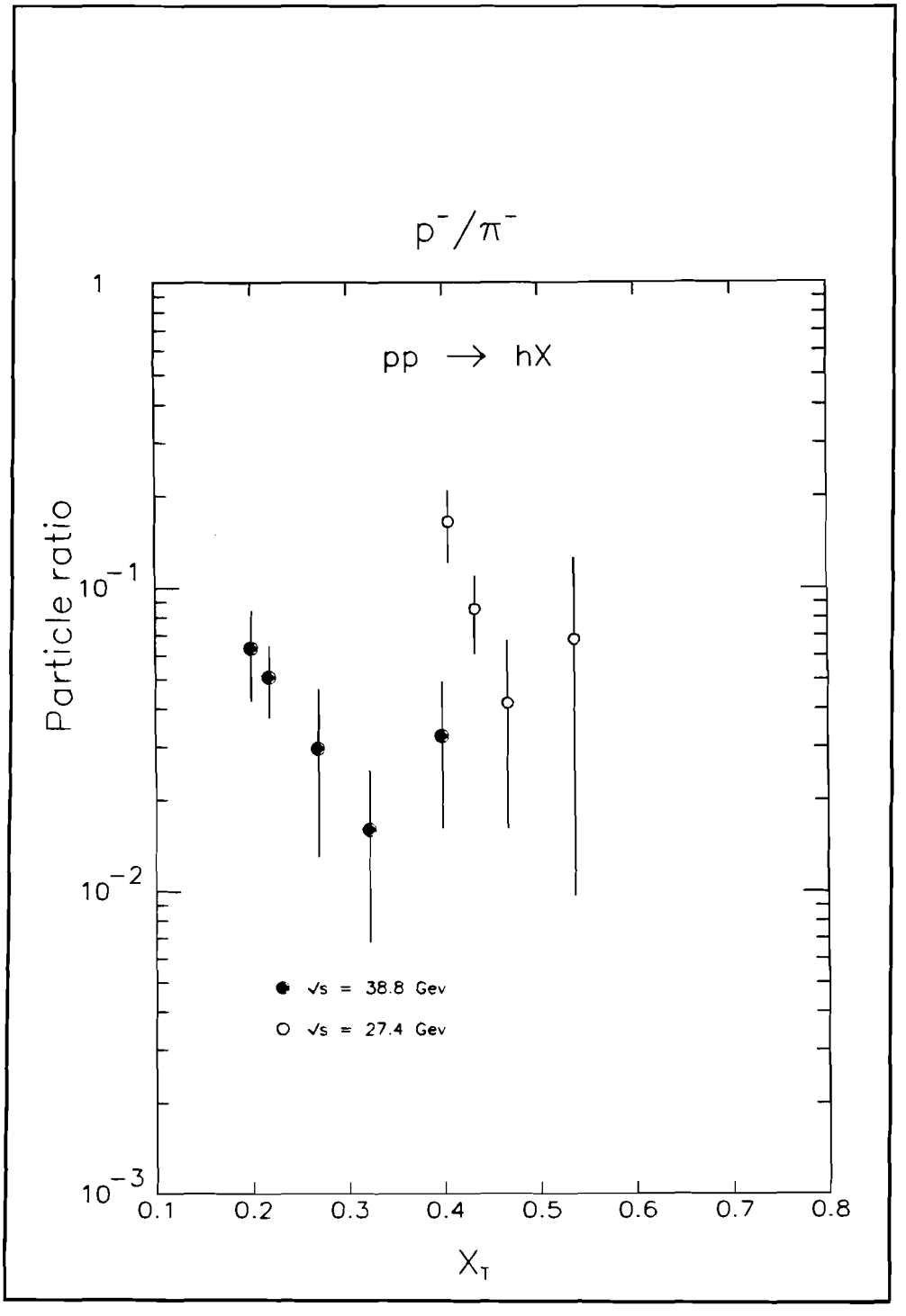

Figure 46. $\bar{p}/\pi^-$ ratio *versus* $x_\perp$ in *pp* at $\sqrt{s} = 27.4$ & 38.8 *Gev*

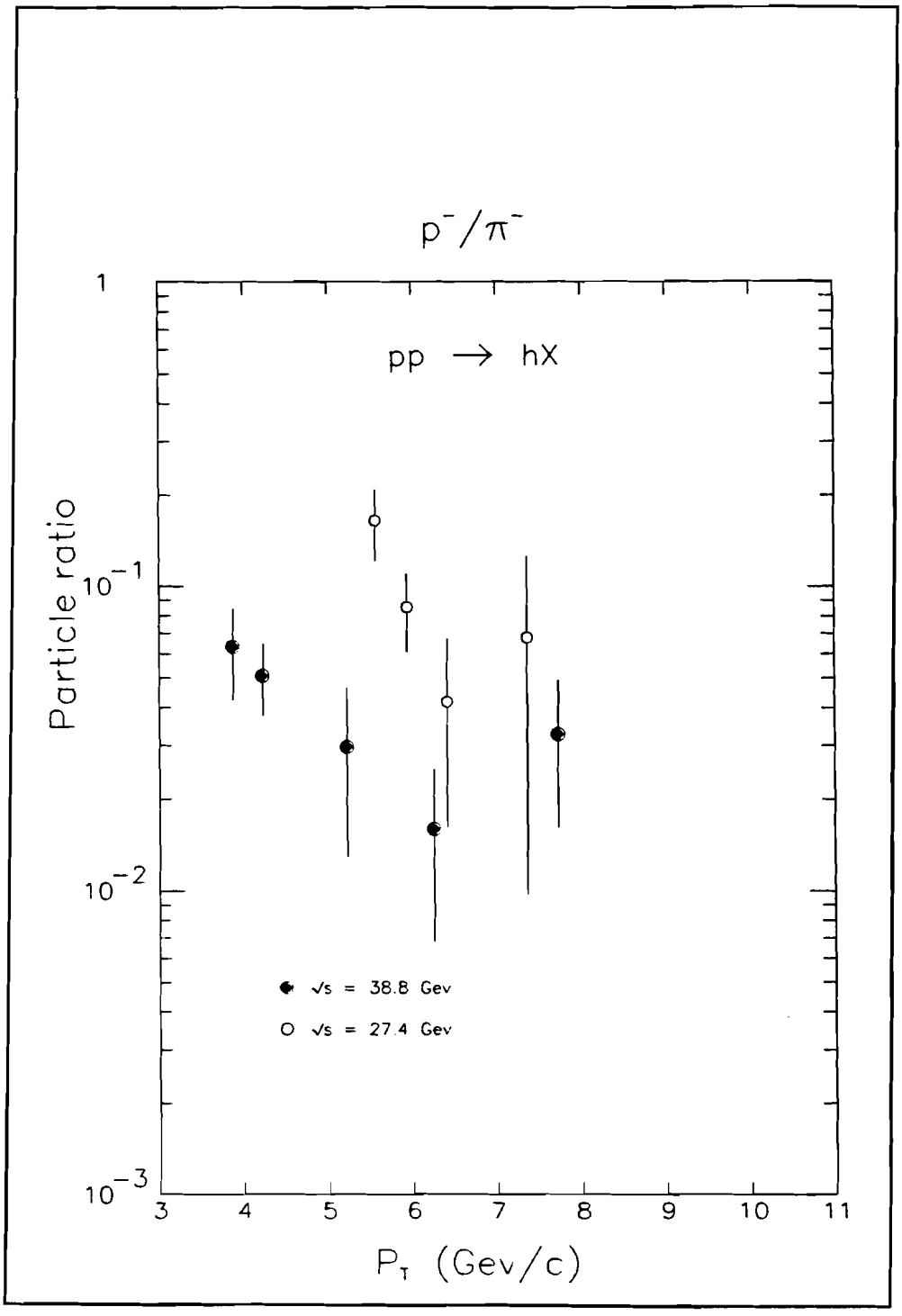

Figure 47. $\bar{p}/\pi^-$ ratio *versus* $p_\perp$ in pp at $\sqrt{s} = 27.4$ & 38.8 *Gev*

VI. C. Single Hadron Unlike-sign Ratios

The measurement of the unlike-sign particle ratios, in contradistinction to the like-sign ratios, requires an accurate knowledge of the relative efficiency of trajectories in different parts of the apparatus. In this analysis, this problem introduces relatively larger uncertainty in the measured unlike-sign particle ratios.

In Figures 48-56 and Tables 21-23 the unlike-sign ratios for pions, kaons and protons in *pp* and *pd* interactions are shown for the two collision energies. The errors shown in the figures and tables are the statistical and systematic uncertainties added in quadrature. The $\sqrt{s} = 27.4$ *Gev* data is fairly consistent with Chicago-Princeton's results but suffers from poor statistical precision. On the other hand the measurements taken at $\sqrt{s} = 38.8$ *Gev* are more precise and in good agreement with the measurements at the lower energy. The π^+/π^- ratio agrees well with the predictions of the Lund model and confirms the simple assumption that the ratio mainly reflects the relative abundance of u and d quarks in the proton at high x. The K^+/K^- and $p/\overline{p}$ ratios show the preponderance of hadrons containing the valence quarks of the proton with the $p/\overline{p}$ ratio demonstrating the paucity of $\overline{p}$'s (no valence quarks) compared to p's (three valence quarks.

Table 21: Unlike-sign particle ratios $\sqrt{s} = 27.4$ Gev pp

$p_\perp$ bin Gev/c	$\langle p_\perp \rangle$ Gev/c	π^+/π^-
5.2 – 5.7	5.55	1.44 ± 1.00
5.7 – 6.2	5.95	2.09 ± 0.76
$p_\perp$ bin Gev/c	$\langle p_\perp \rangle$ Gev/c	K^+/K^-
5.2 – 5.7	5.53	5.59 ± 4.16
5.7 – 6.2	5.95	6.63 ± 2.66
$p_\perp$ bin Gev/c	$\langle p_\perp \rangle$ Gev/c	$p/\bar{p}$
5.2 – 5.7	5.55	2.07 ± 1.55
5.7 – 6.2	5.95	5.42 ± 2.46

Table 22: Unlike-sign particle ratios $\sqrt{s} = 27.4$ *Gev pd*

$p_\perp$ bin *Gev/c*	$\langle p_\perp \rangle$ *Gev/c*	π^+/π^-
5.2 – 5.7	5.57	0.90 ± 0.30
5.7 – 6.2	5.95	1.46 ± 0.28
6.2 – 6.7	6.42	1.93 ± 0.44
6.7 – 7.2	6.92	0.80 ± 0.37
7.2 – 7.7	7.34	1.19 ± 0.72
$p_\perp$ bin *Gev/c*	$\langle p_\perp \rangle$ *Gev/c*	K^+/K^-
5.2 – 5.7	5.57	5.33 ± 2.14
5.7 – 6.2	5.95	6.66 ± 1.57
6.2 – 6.7	6.41	8.38 ± 2.43
6.7 – 7.2	6.98	3.86 ± 2.02
7.2 – 7.7	7.37	16.42 ± 13.41
$p_\perp$ bin *Gev/c*	$\langle p_\perp \rangle$ *Gev/c*	$p/\bar{p}$
5.2 – 5.7	5.56	2.25 ± 1.13
5.7 – 6.2	5.95	2.96 ± 0.92
6.2 – 6.7	6.41	11.12 ± 7.15

Table 23: Unlike-sign particle ratios $\sqrt{s} = 38.8$ *Gev pp*

$p_\perp$ bin *Gev/c*	$\langle p_\perp \rangle$ *Gev/c*	π^+/π^-
3.6 – 4.0	3.88	1.62 ± 0.48
4.0 – 4.5	4.23	1.42 ± 0.22
4.5 – 5.0	4.72	1.41 ± 0.23
5.0 – 5.5	5.19	1.56 ± 0.30
5.5 – 6.0	5.64	1.57 ± 0.33
6.0 – 6.5	6.20	1.64 ± 0.47
7.0 – 7.5	7.25	3.09 ± 1.37
7.5 – 8.0	7.78	1.65 ± 0.72
8.0 – 9.0	8.47	1.50 ± 0.73
$p_\perp$ bin *Gev/c*	$\langle p_\perp \rangle$ *Gev/c*	K^+/K^-
4.0 – 4.5	4.23	2.46 ± 0.42
4.5 – 5.0	4.72	2.45 ± 0.47
5.0 – 5.5	5.20	5.09 ± 1.32
5.5 – 6.0	5.64	4.03 ± 1.08
6.0 – 6.5	6.16	5.70 ± 1.89
7.0 – 7.5	7.26	11.74 ± 5.59
7.5 – 8.0	7.81	8.82 ± 4.46
8.0 – 9.0	8.45	7.86 ± 4.66
$p_\perp$ bin *Gev/c*	$\langle p_\perp \rangle$ *Gev/c*	$p/\bar{p}$
3.6 – 4.0	3.89	9.14 ± 4.22
4.0 – 4.5	4.23	5.73 ± 1.89
5.0 – 5.5	5.23	5.99 ± 4.21
6.0 – 6.5	6.16	8.05 ± 5.65
7.5 – 8.0	7.79	2.49 ± 1.58

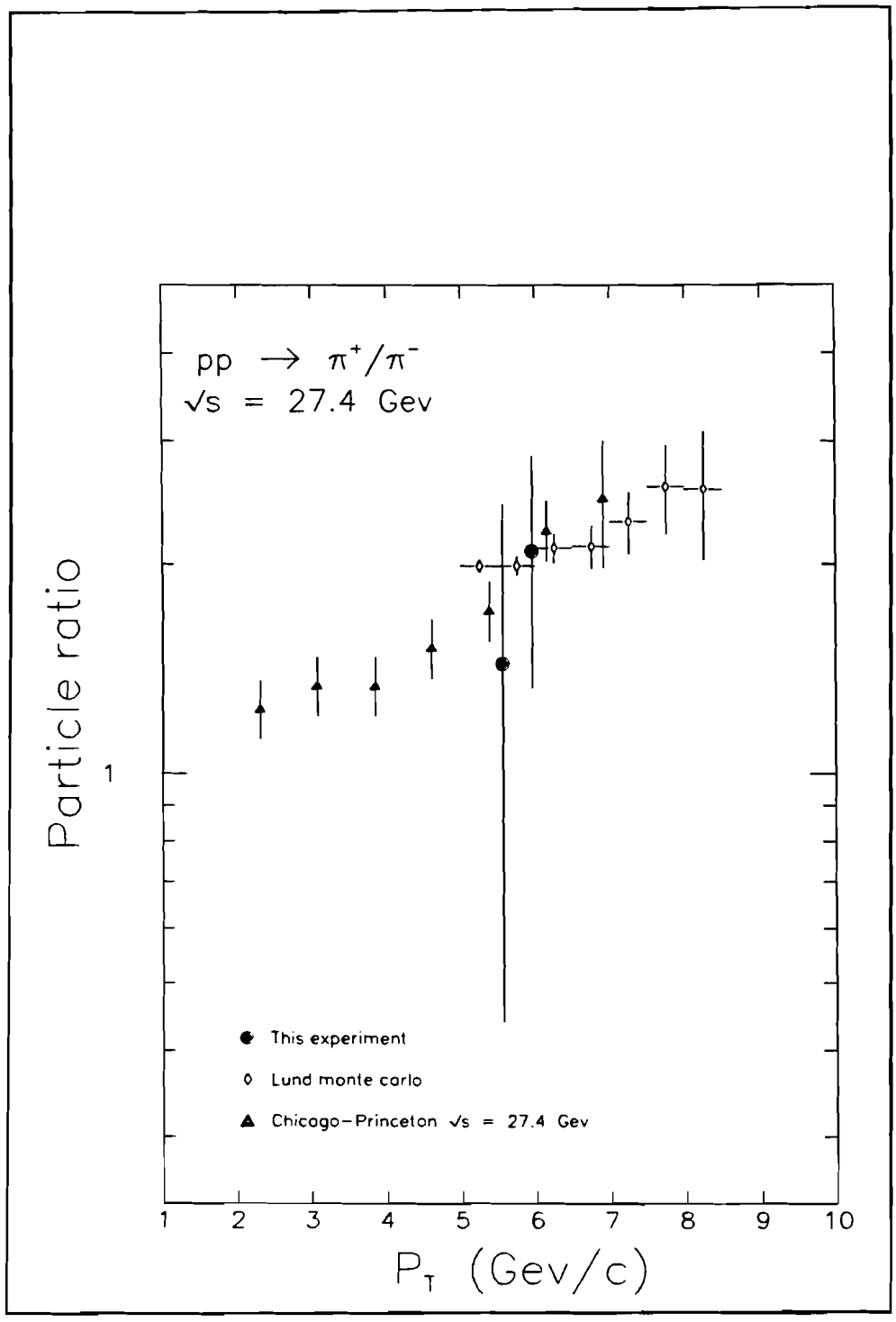

Figure 48. π^+ / π^- **ratio** *versus* $p_\perp$ **in** *pp* **at** $\sqrt{s} = 27.4$ *Gev*

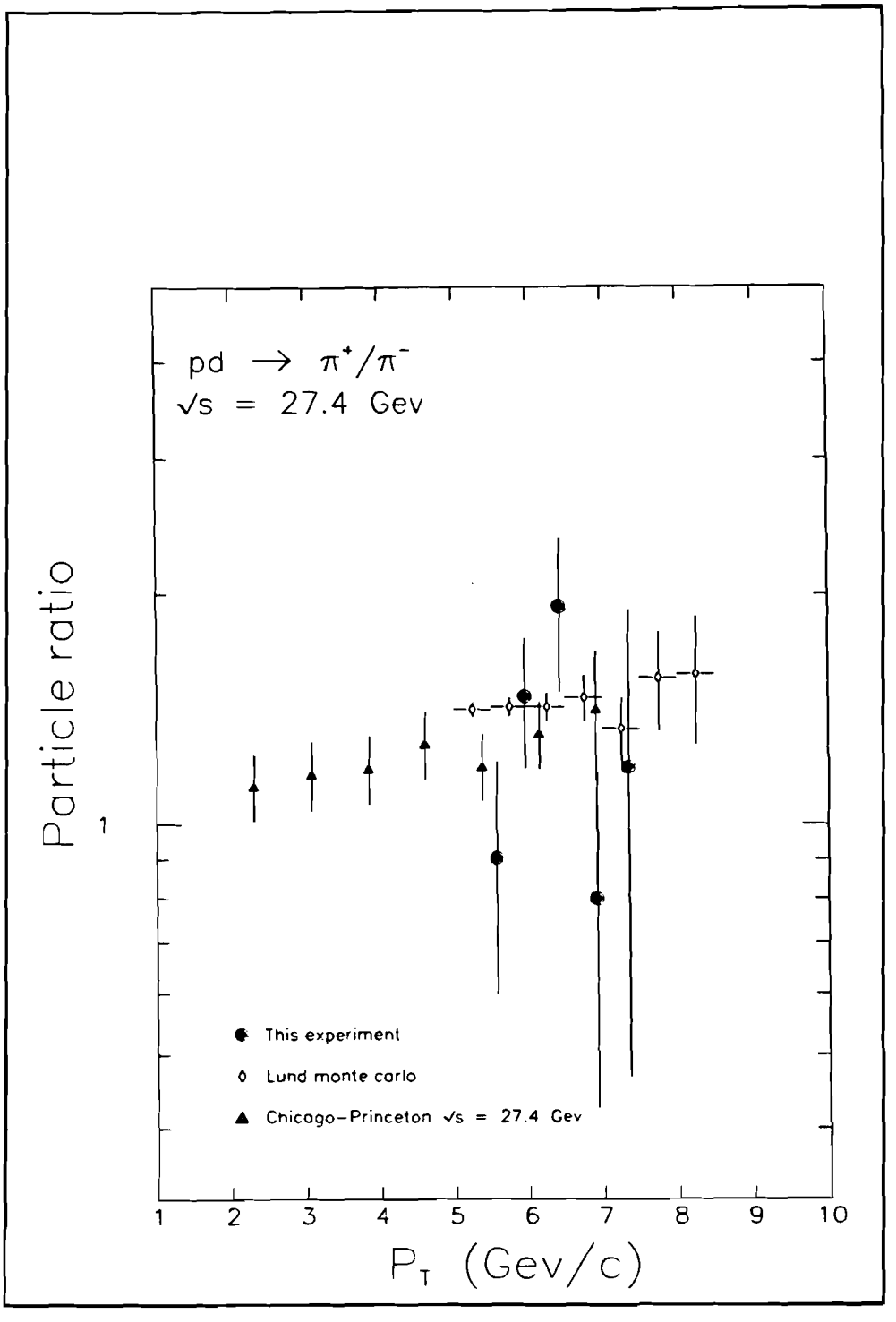

Figure 49. π^+ / π^- ratio *versus* $p_\perp$ in pd at $\sqrt{s} = 27.4$ *Gev*

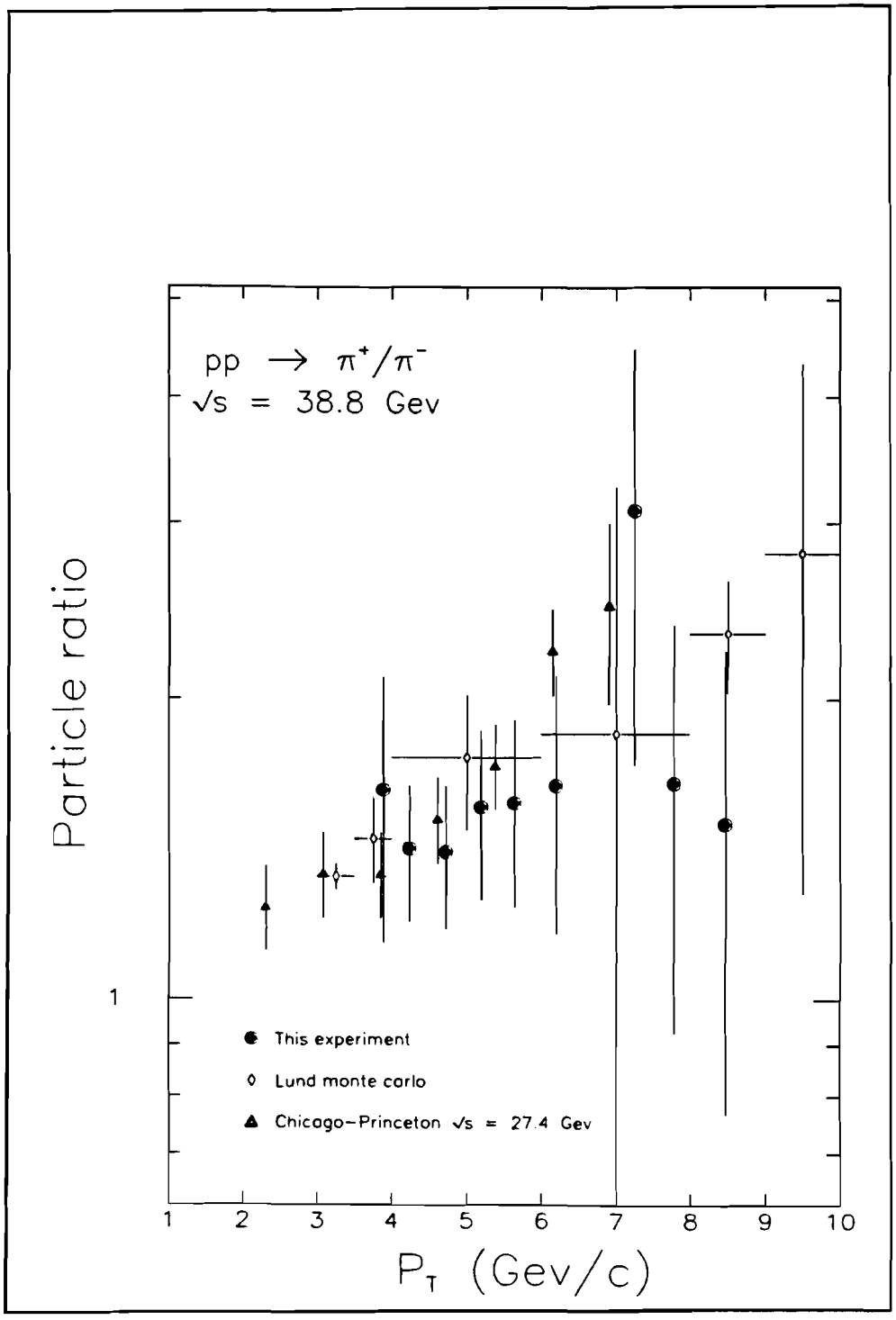

Figure 50. π^+ / π^- ratio *versus* $p_\perp$ in pp at $\sqrt{s} = 38.8$ *Gev*

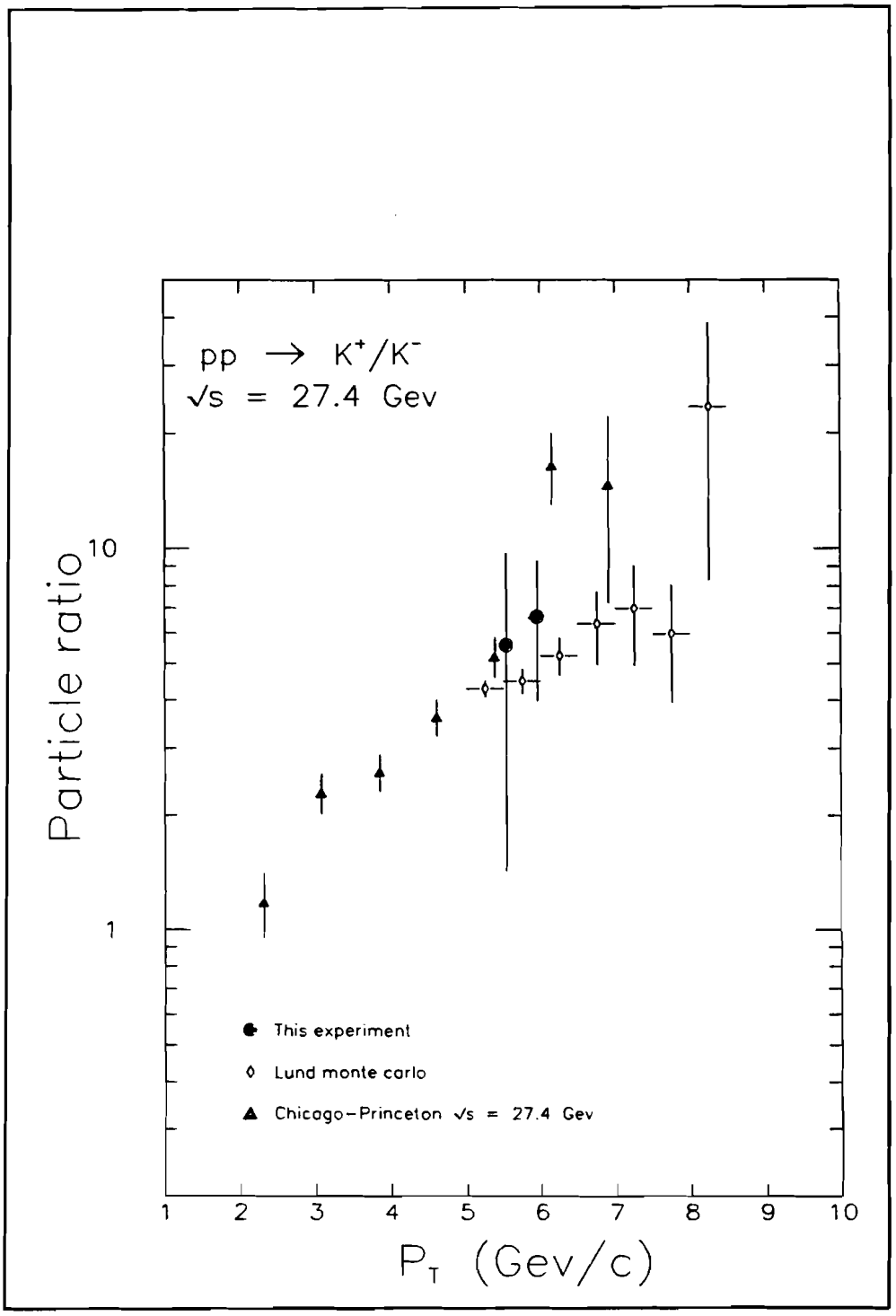

Figure 51. K^+/K^- ratio *versus* $p_\perp$ in pp at $\sqrt{s} = 27.4$ *Gev*

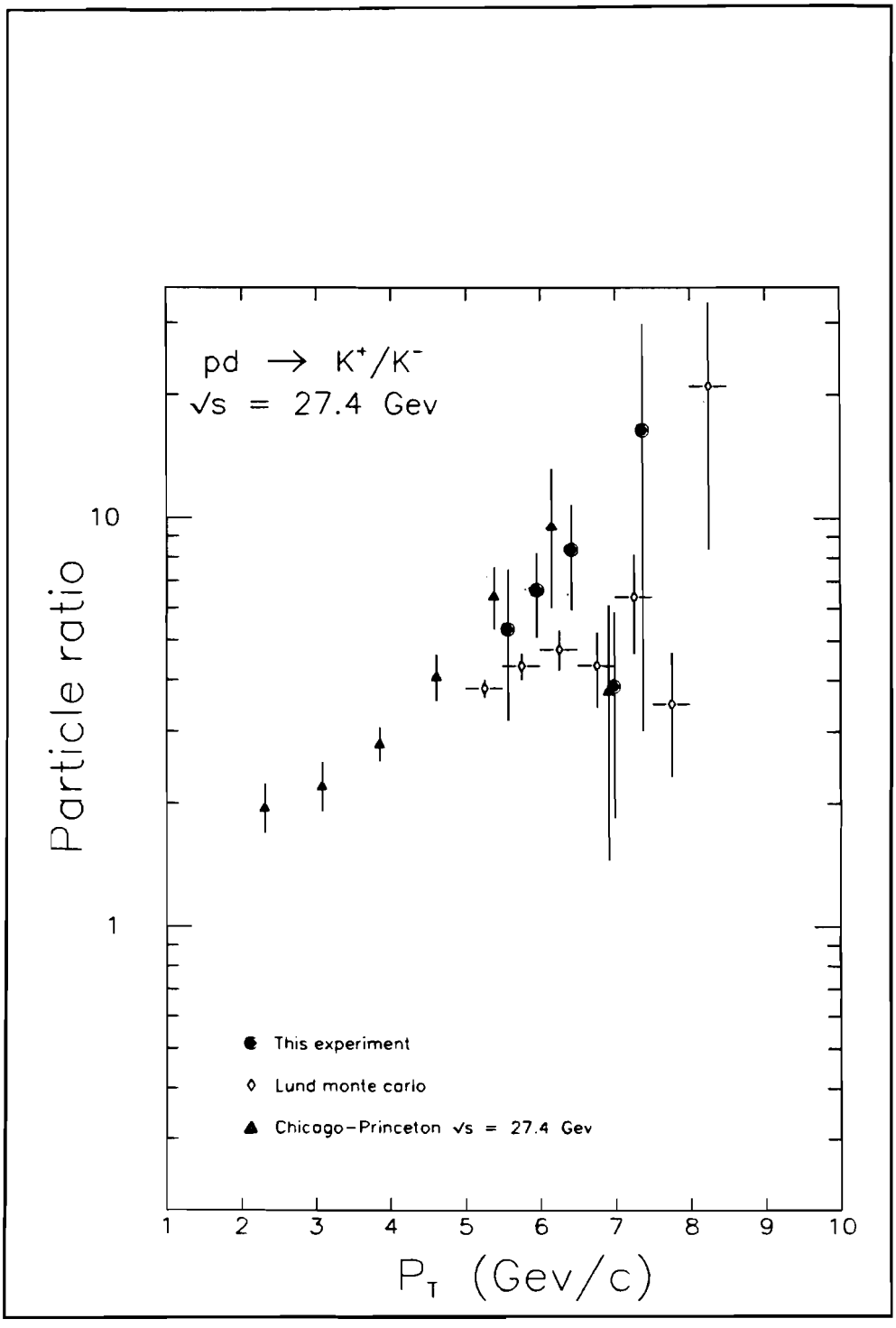

Figure 52. K^+/K^- ratio *versus* $p_\perp$ in *pd* at $\sqrt{s} = 27.4$ *Gev*

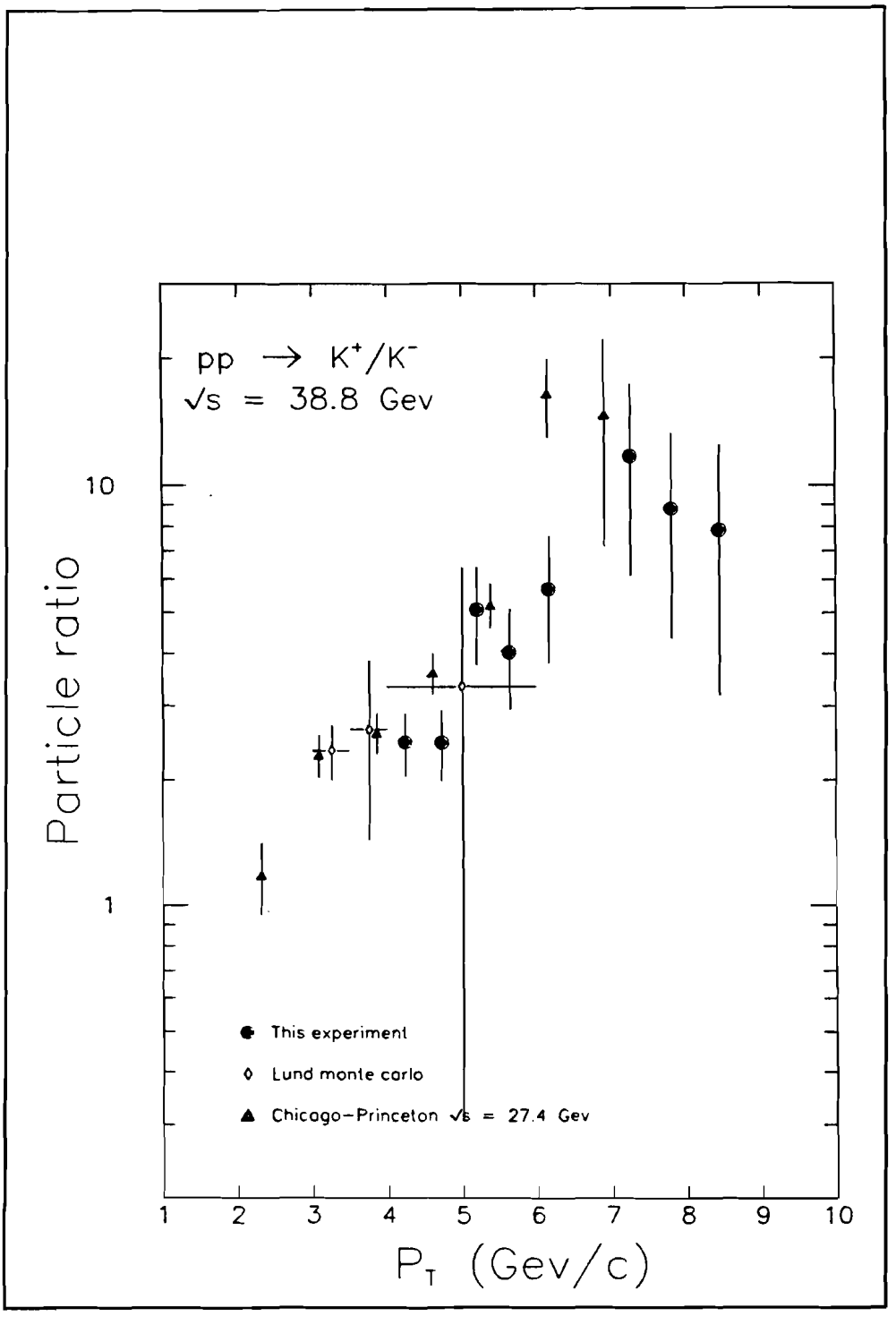

Figure 53. K^+/K^- ratio *versus* $p_\perp$ in pp at $\sqrt{s} = 38.8$ *Gev*

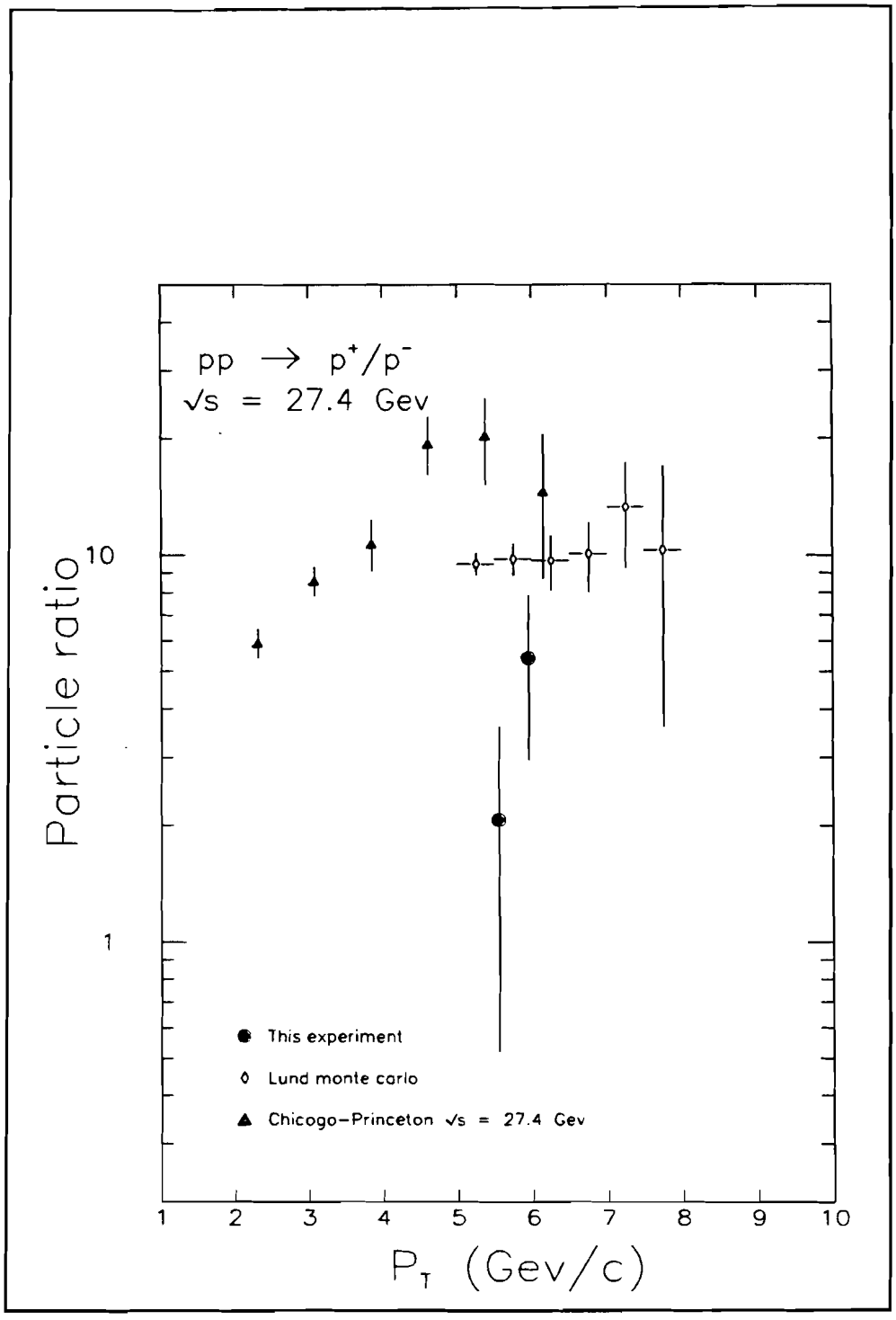

Figure 54. $\bar{p}/p$ ratio *versus* $p_\perp$ in pp at $\sqrt{s} = 27.4$ *Gev*

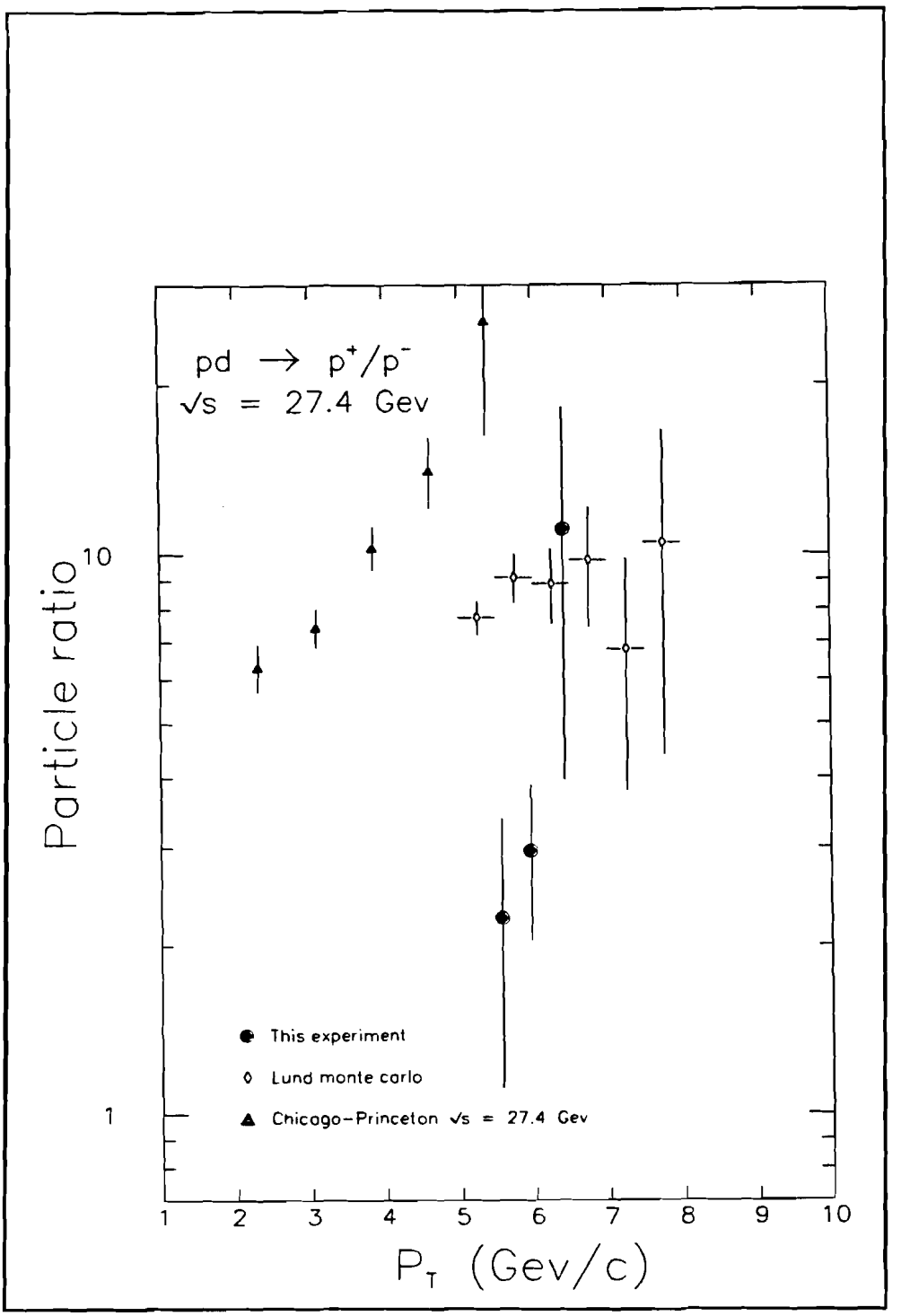

Figure 55. $\bar{p}/p$ ratio *versus* $p_\perp$ in pd at $\sqrt{s} = 27.4$ Gev

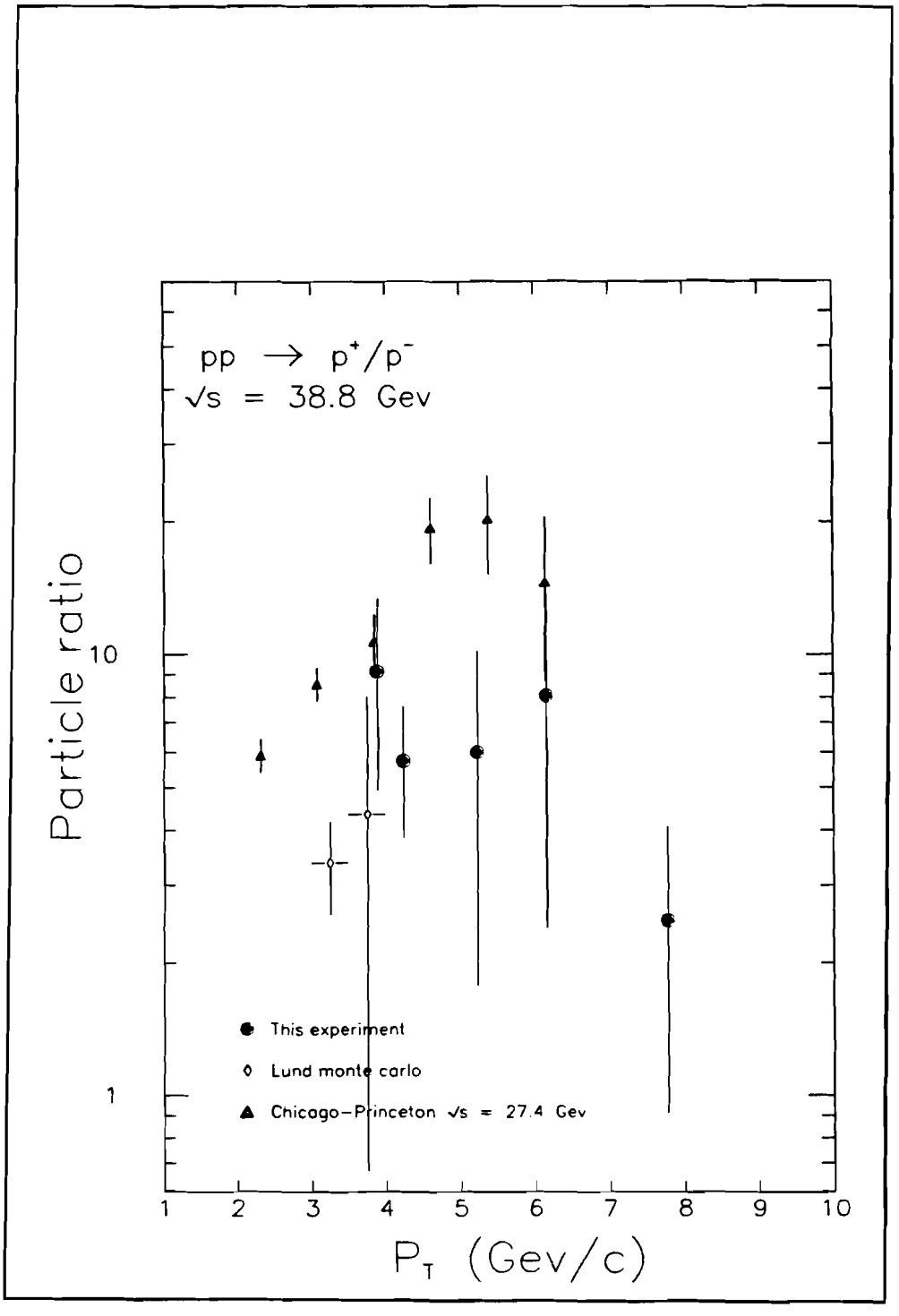

Figure 56. $\bar{p}/p$ ratio *versus* $p_\perp$ in pp at $\sqrt{s} = 38.8$ *Gev*

VI. D. The Dihadron Correlation Function

Figure 57 and Table 24 show the unlike-sign hadron correlation function, $R_{h^+h^-}$, measured at $\sqrt{s} = 38.8$ *Gev* versus the pseudo-mass, m', where m' is equal to the sum of the magnitude of the transverse momentum of each of the two hadrons, in comparison to the results of the Columbia-Fermilab-Stony Brook (CFS) experiment[59] taken at $\sqrt{s} = 27.4$ *Gev* in proton-beryllium collisions.[60] The uncertainties shown in Figure 57 and Table 24 are the statistical and systematic errors added in quadrature. The correlation function is the ratio of the probability of observing two hadrons with opposing transverse momenta, $p_{\perp 1}$ and $p_{\perp 2}$, to the probability if the hadrons are uncorrelated. As shown in the previous section, high $p_\perp$ hadrons carry a large fraction of the scattered parton momentum; thus two opposing high $p_\perp$ hadrons could be expected to carry both of the partons involved in the "hard-scattering" interaction and show a greater correlation as the "hardness" of the interaction increases. The results show a similar exponential rise of $R_{h^+h^-}$ with pseudo-mass as seen by CFS; however, the correlation function measured by CFS is affected by the anomalous nuclear enhancement (also know as A-dependence)[61] of the single hadron production rate and by the

---

[59] H. Jöstlein et al.

[60] R is determined as a function of pseudo-mass because 1) m' facilitates direct comparison of single and dihadron data, 2) m' is a measure of the "hardness" of the constituent scattering, and 3) m' was used by CFS.

[61] R.L. McCarthy et al., Phys. Rev. Lett. 40, 213 (1978); Y.B. Hsiung et al., Phys. Rev. Lett. 55, 457 (1985); V.V. Abramov et al., Z. Phys. C24, 201

anomalous nuclear reduction[62] of the dihadron production rate which should decrease the magnitude of $R^{CFS}_{h^+h^-}$ by a factor of .34±.04 relative to $R^{E605}_{h^+h^-}$. On the other hand the correlation function measured by E605 is averaged over a larger azimuthal angular range than E494 and thus samples kinematic regions where the two hadrons are not truly back-to-back. The estimated effect to the correlation function due to the relative p_{out}[63] acceptance of the two experiments increases the $R^{CFS}_{h^+h^-}$ by 2.1 ± .2. Overall $R^{CFS}_{h^+h^-}$ is predicted to be .7 ± .1 times as large as $R^{E605}_{h^+h^-}$; however, the measured values of $R_{h^+h^-}$ show that the CFS results are about a factor of three higher in the region of overlap. Two additional effects that could resolve the inconsistency between the two experiments are the decrease of the correlation function at a given pseudo-mass as a function of beam energy indicated in the measurements of CFS[64] and the fact that the correlation function for *pp* collisions should be smaller than the correlation function for an isoscalar, A = 1, target due to charge conservation.

Of greater interest is the relative correlation function, $r_{\alpha\beta}$, defined in section V.D., which could indicate flavor dependence of the hard-scattering interaction. (If only quark–quark collisions contributed to single and dihadron production then the relative correlation function would be one for all pairs.) To this end the

(1984); Antreasyan et al, Phys. Rev. D19, 764 (1979)

[62] P.B. Straub, Ph.D. thesis.

[63] p_{out} is defined as the component of the lower $p_\perp$ hadron's momentum perpendicular to the plane formed by the beam and higher $p_\perp$ hadron's momentum.

[64] See Figure 23 of Jöstlein et al.

relative correlation functions measured in this experiment are shown in comparison to measurements made by CFS and predictions by the Lund monte carlo in Figure 58 (only statistical uncertainties are plotted). Table 25 gives the plotted data with the statistical and systematic uncertainties. In addition the CFS experiment sought to extrapolate their results to proton-nucleon interactions by correcting for anomalous nuclear enhancement which is labelled "A-corrected". Agreement of the *pp* relative correlation function and the "A-corrected" values of CFS confirm the validity of this technique within the precision of the two sets of measurements. However, the deviation of some of the *pp* measurements, such as $\pi^+ - \pi^-$, $\pi^+ - K^-$ and $K^+ - K^-$ from unity seems to point to flavor-dependence of the constituent interaction which is at odds with the basic tenets of QCD. This discrepancy may be explicable in terms of the intrinsic transverse momentum, $k_\perp$, of the constituent partons as proposed by CFS. Although the data in this experiment were obtained at a higher m' than CFS, both results are at nearly the same $m'/\sqrt{s}$ of .25; hence, the observations made by CFS — that the intrinsic $k_\perp$ biases the single hadron particle fractions — are probably applicable here. In addition the fact that quark–gluon and gluon–gluon scattering also contribute to the production of hadrons in this pseudo-mass range could also cause $r_{\alpha\beta}$ to deviate from unity. In particular gluon–gluon scattering would introduce a correlation between particle–anti-particle pairs. Note, however, that the flatness in the unlike-sign

single hadron ratios at $p_\perp > 7$ Gev/c could indicate the diminished effect of intrinsic $k_\perp$ and non-quark–quark interactions at even higher pseudo-mass and point to a region where the flavor-dependence of the hard-scattering process could be studied without bias.

The wide disagreement between the measurements of this experiment and the Lund predictions may be related to the failure of the model to correctly forecast single positive hadron production.

Table 24: Correlation Function

Pseudo-mass (Gev/c)	$R_{h^+h^-}$	Statistical uncertainty
7.81	951.2	615.7
7.98	1180	772
8.17	1080	771
8.36	1030	622
8.59	1520	775
8.36	2940	1400
9.02	2570	1410
9.23	4730	2090
9.80	8760	3200
10.14	17200	5220
10.79	40600	11400
11.92	164000	98900
13.26	589000	356000

Table 25: Relative Correlation Function

Pair	$r_{\alpha\beta}$	Statistical uncertainty	Systematic uncertainty
$\pi^+\pi^-$	1.32	.05	.004
$K^+\pi^-$	1.08	.07	.02
$p\pi^-$	.50	.10	.18
π^+K^-	.47	.07	.01
K^+K^-	.60	.12	.005
pK^-	.44	.26	.004
$\pi^+\bar{p}$	.45	.39	.24
$K^+\bar{p}$	.69	.60	.18
$p\bar{p}$	2.03	1.79	.98

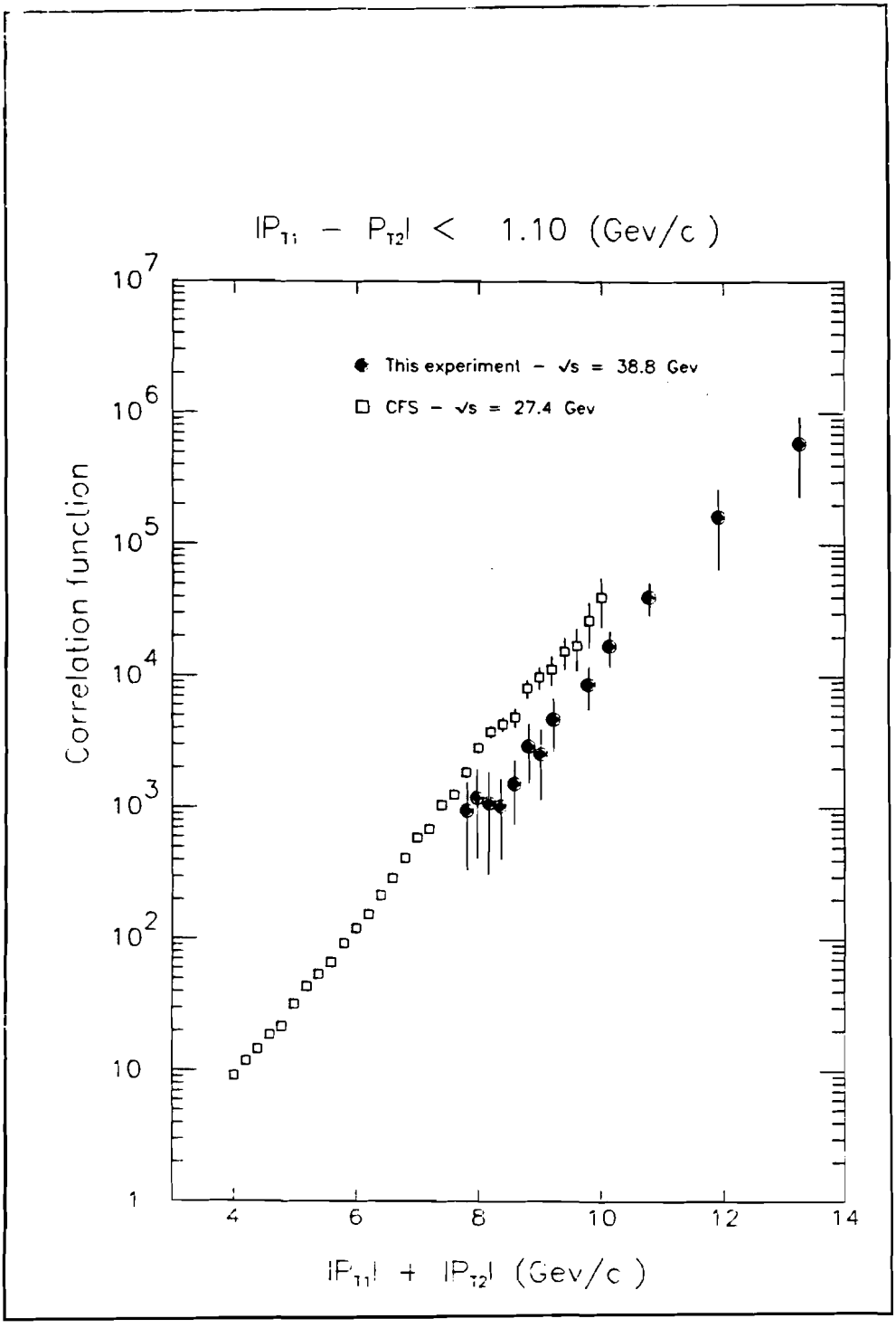

Figure 57. The correlation function, $R_{h^+h^-}$, *versus* m'.

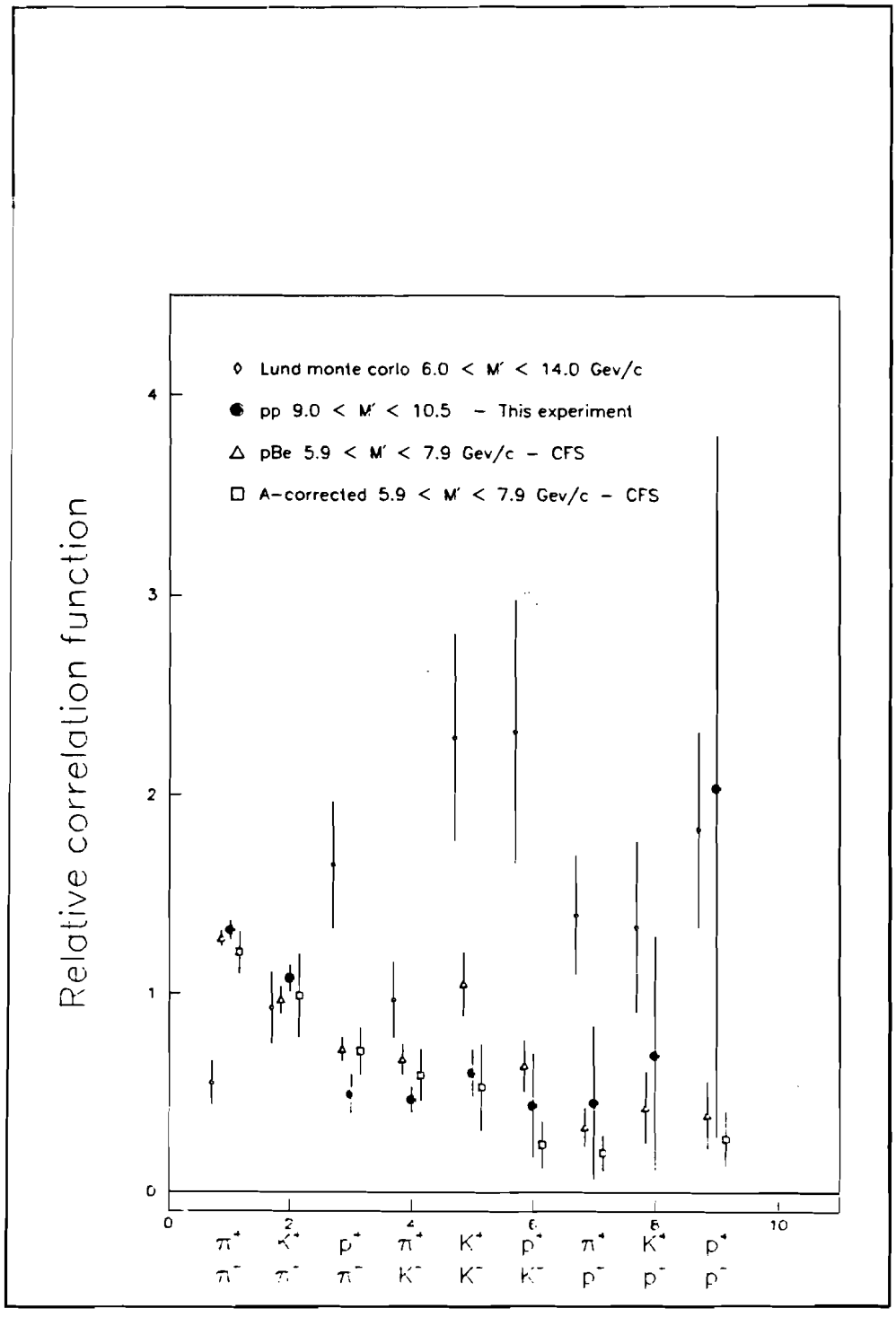

Figure 58. The relative correlation function, $r_{\alpha\beta}$, *versus* species.

VII. Summary of Conclusions

Measurements of single hadron production in pp interactions at $\sqrt{s} = 27.4$ and $\sqrt{s} = 38.8$ Gev and pd interactions at $\sqrt{s} = 27.4$ Gev indicate the following conclusions:

1) The steep dependence of the invariant cross section as a function of transverse momentum is approximately the same as measured in other experiments performed at comparable energies.

2) The scaling fit, $E\frac{d^3\sigma}{dp^3} = Af(x_\perp)p_\perp^{-N}$, yields a power of N consistent other experiments.

3) Analysis of the single hadron K^+/π^+production ratio in this experiment and in μp interactions confirms that high $p_\perp$hadrons produced in pp collisions carry at least 60% of the scattered parton momentum.

4) The Lund monte carlo does not properly model the production of high $p_\perp$single, positive hadrons in pp and pd collisions.

5) At large transverse momentum (> 7 Gev/c) in $\sqrt{s} = 38.8$ Gev pp interactions, the like-sign single hadron production ratios tend to be constant.

The dihadron correlation function measurement in $\sqrt{s} = 38.8$

Gev pp interactions suggests the following conclusions:

1) The shape of the dihadron correlation function measurements in pp collisions at $\sqrt{s} = 38.8$ *Gev* show good agreement with results of pBe collisions at $\sqrt{s} = 27.4$ *Gev* .

2) The indications of flavor dependence of the parton-parton constituent interaction in the relative correlation function are probably due to the intrinsic transverse momentum of the partons in the nucleon and the contributions of quark–gluon and gluon–scattering to high $p_\perp$ hadron production.

References

V.V. Abramov *et al.*, Zeitschrift für Physik C25 (1984), p. 204.

M. Adams *et al.*, Nuclear Instruments and Methods **217** (1983), 237–243.

H. Aihara *et al.*, Physical Review Letters **53** (1984), p. 2199.

T. Åkesson *et al.*, Nuclear Physics **B246** (1984), 408–430.

B. Alper *et al.*, Nuclear Physics **B100** (1975), 237–290.

M. Althoff *et al.*, Zeitschrift für Physik **C17** (1983), p. 5.

E. Andersson *et al.*, Physics Reports **97** (1983), p. 31.

A.L.S. Angelis *et al.*, Nuclear Physics **B209** (1982), 284-300.

D. Antreasyan *et al.*, Physical Review Letters **38** (1977), 112–114.

D. Antreasyan *et al.*, Physical Review **D19** (1979), 764–778.

M. Arneodo *et al.*, Physics Letters **150B** (1985), p. 458.

J.J. Aubert *et al.*, Physics Letters **135B** (1984), p. 225.

P. Baringer *et al.*, ANL-HEP-PR-85-121 (1985).

W. Bartel *et al.*, Physics Letters **104B** (1981), p. 325.

H.–U. Bengtsson and G. Ingleman, CERN LU-TP/84-3 **Th.3820** (1984).

Ch. Berger *et al.*, Nuclear Physics **B124** (1983), p. 189.

R. Bouclier *et al.*, Nuclear Instruments and Methods **205** (1983), 403–423.

A. Breakstone *et al.*, Zeitschrift für Physik **25** (1984), 21–27.

A. Breakstone *et al.*, Physics Letters **135B** (1984), p. 510.

A. Breakstone *et al.*, Zeitschrift für Physik **C28** (1985), p. 335.

F. W. Büsser *et al.*, Nuclear Physics **B106** (1976), 1–30.

F.E. Close,, "An Introduction to Quarks and Partons", Academic Press, London, 1979, p. 312.

A.P. Contogouris, R. Gaskell and S. Papadopoulos, Physical Review **D17** (1978), 2314–2323.

G. Coutrakon, SUNY at Stony Brook, Ph.D. thesis (1982).

J.A. Crittenden, Columbia University, Ph.D thesis (1986).

J.A. Crittenden *et al.*, Physical Review **D34** (1986), 2584–2600.

R. Cutler and D. Sivers, Physical Review **D16** (1978), 679–689.

M. Derrick *et al.*, Physics Letters **158B** (1985), p. 519.

M. Derrick *et al.*, Physical Review Letters **54** (1985), p. 2568.

W.T. Eadie, D. Drijard, F.E. James, M. Roos and B. Sadoulet, "Statistical Methods in Experimental Physics", North Holland, New York, 1971.

S. Ekelin and S. Fredriksson, Physics Letters **149B** (1984), p. 509.

T. Ekelöf, CERN-EP/84-168 Lectures given at the 1984 SLAC Summer Institute in Particle Physics, 23 July - 3 August (1984).

R.P. Feynman *et al.*, Nuclear Physics **B128** (1977), p. 1.

R. D. Field. CALT-68-696 Lectures given at La Jolla Institute Summer Workshop, July 31 - August 18 (1978), 105-117.

R. D. Field, Physical Review Letters **40** (1978), 997-1000.

R.D. Field and R.P. Feynman, Nuclear Physics **B136** (1978), p. 1.

R.D. Field and R.P. Feynman, Physical Review **D15** (1977), p. 2590.

R.J. Fisk, SUNY at Stony Brook, Ph.D. Thesis (1978).

H. Glass, SUNY at Stony Brook. Ph.D. thesis (1985).

R. Gray, University of Washington, Ph.D thesis, in preparation.

R. Gray and J.P. Rutherfoord, Nuclear Instruments and Methods **A244** (1986), 440-443.

Y.B. Hsiung *et al.*, Physical Review Letters **55** (1985), p. 457.

H. Jöstlein *et al.*, Physical Review **D20** (1979), p. 53.

Ph. Mangeot *et al.*, Nuclear Instruments and Methods **216** (1983), 79-91.

R.L. McCarthy *et al.*, Physical Review Letters **40** (1978), p. 213.

J.F. Owens, E. Reya and M. Glück, Physical Review **D18** (1978), p. 1501.

Y. Sakai, Kyoto University, Ph.D. thesis (1984).

A. Seiden, *Comparison of Jet Fragmentation in Various Processes*, Invited paper, 6^{th} International Conference on Proton Antiproton Physics, Aachen, Germany, July 1986.

T. Sjöstrand, Computer Physics Communications **27** (1982), p. 243.

P.B. Straub, University of Washington, Ph.D thesis, in preparation.

K.D. Williamson Jr. and F.J. Edenskuty, Eds., "Liquid Cryogens", CRC Press,Inc., 1981, p. 3.

T. Yoshida, Kyoto University, Ph.D thesis (1987).

Appendix A. The Helium Purifier

The helium in the Čerenkov radiator must be very pure to permit transmission of ultraviolet Čerenkov photons. In particular, concentrations of oxygen in excess of about 1 *ppm* would render the Čerenkov detector useless; hence, the helium purification system concentrates on the removal of oxygen from helium.

As shown in Figure 59, gas exiting the radiator either passes directly into the helium purifier or goes through the control tube, described later. In either case, the helium is pumped at a rate of about 2.5 radiator volumes(220,000 liters) per day by a set of pumps.[65] At this point, 2% H_2 / 98% He gas is introduced into the flow before the gas enters a Deoxo catalyser[66] that combines the hydrogen with oxygen to produce water vapor. After leaving the Deoxo, gas can enter one of the two dryer-trap systems. The dryer and trap both contain molecular sieve material to remove impurities; the trap is kept at liquid nitrogen temperature to freeze out water vapor and other contaminants. Gas exiting the trap is warmed to room temperature in a heat-exchanger and returned to the upstream end of the radiator vessel.

[65] Model 2737-CM390, Thomas Industries,Inc., Power Air Division, Sheboygan, Wisconsin.

[66] Model 1800-100, Engelhard Systems, Union NJ 07083

An advantage of a helium gas radiator, chosen for its low index of refraction and small chromatic dispersion, is its ability to use a cold trap at 77°K to remove impurities. Other gases in use or considered for ring-imaging Čerenkov detectors such as nitrogen, argon, hydrocarbons or fluorocarbons[67] will liquify at this temperature. One problem encountered with this purification system was inadvertent hydrogen gas contamination from uncatalysed H_2/He gas. Hydrogen raised the index of refraction slightly and approximately doubled the effect of chromatic dispersion on the photon position resolution during the 400 *Gev/c* running. By purging the radiator with helium gas and halving the H_2/He flow rate, the hydrogen was essentially removed from the radiator for the 800 *Gev/c* running period.

Since the molecular sieve material can become saturated with impurities, dual dryer-trap systems were employed. While one system is purifying the gas, the other is recharged. Recharging comprises a warm($\approx$ 100° C) gaseous nitrogen flush for about two days, followed by a two day pumpdown with the heat still applied and concluded by a two day evacuation at room temperature.

The control tube is a 12.7 *m* long, 15 *cm* diameter aluminum pipe with a solar-blind photomultiplier tube (UVPM) on the up-stream end and a Am^{241}-Kr ultraviolet light source[68] on the other

[67] T. Ekelöf, Lectures given at the 1984 SLAC Summer Institute in Particle Physics 23 July - 3 Aug., CERN-EP/84-168 (1984).
[68] R. Bouclier et al, Nucl. Inst. & Methods 205, 403 (1983).

end. By comparing the current from the UVPM when the control tube was evacuated to $\leq 4 \times 10^{-4}$ *Torr* and when the control tube contained flowing helium gas, the mean transmission rate for ultraviolet Čerenkov photons was found to be 78 ± 3% over the course of both runs. This transmission rate compares favorably with prototype test results of 81 to 87% obtained with an 8 *m* long radiator utilizing helium from dewar boil-off at a flow rate of about one radiator volume (550 liters) per hour.[69]

The pressure of the gas in the radiator vessel was maintained between 5 - 9 *inches* of H_2O above atmospheric pressure by filling with He gas from liquid helium boil-off or venting to the atmosphere. The radiator vessel was wrapped in fiberglass insulation to reduce temperature gradients across the volume of the radiator vessel to less than 2° C; the mean temperature was allowed to vary with "room" temperature in a range from 12° C to 27° C ("room" temperature varies appreciably in Fermilab's Meson laboratory.)

[69] Ph. Mangeot et al, Nucl. Inst. & Methods 216, 79 (1983).

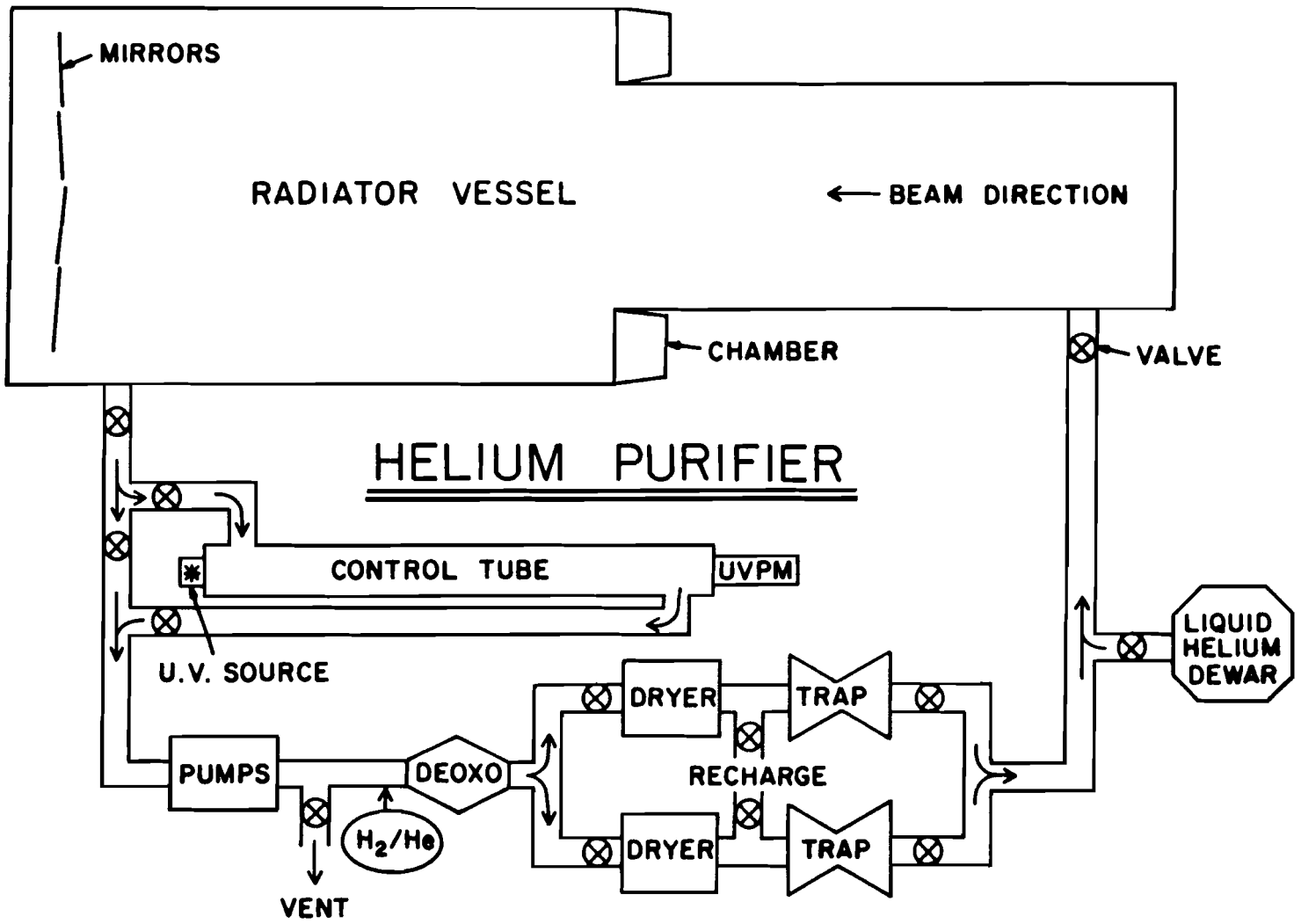

Figure 59. Helium Purification System

Appendix B. Detector Efficiency

The efficiency of the following detector elements was determined using tracks found in events with the pre-scaled ETFI trigger:

1) Hodoscopes,

2) Wire chambers, and

3) Trigger logic.

The tracking algorithm was modified for these triggers so that masking with the calorimeter and station 2 hodoscopes was not performed.

For the purpose of determining the efficiency of individual hodoscopes, each counter was divided into 8 equal size slices in the long direction. The efficiency of each slice is defined as the ratio of the number of tracks through the slice when the hodoscope fired to the total number of tracks through the slice. The average hodoscope efficiency for each hodoscope plane was about .97.

The efficiencies of the station 1 MWPC's and the station 2 and 3 drift chambers were calculated for each quarter plane of each chamber — the planes were quartered vertically. For each quarter plane the efficiency is N_{hits}/N_{tracks} where N_{hits} is the number of tracks with the predicted wire fired on the track and N_{track} is the

number of tracks. The following table lists the average wire chamber efficiencies for the 800 Gev/c running period:

Table 26: Wire Chamber Efficiencies

Station 1	Eff'y	Station 2	Eff'y	Station 3	Eff'y
Y1A	.74	Y2	.95	Y3	.91
U1A	.88	Y2′	.95	Y3′	.92
V1A	.95	U2	.96	U3	.94
Y1B	.88	U2′	.95	U3′	.92
U1B	.91	V2	.95	V3	.94
V1B	.84	V2′	.96	V3′	.93

The efficiency of each of the trigger logic bits (YU, YD, Y and 2Y) that required a at least one trigger matrix were determined in the following way. The trigger matrices satisfied by the tracks in an event — called a 'track' trigger matrix — were determined. A 'track' trigger matrix was defined as a track with a trajectory that fulfilled the pre-set hodoscope pattern of the trigger matrix and that fired the hodoscopes. Then the combinations of trigger matrices in the dc logic were checked against the list of 'track' trigger matrices to see which dc logic bits should have been set. The efficiency of a logic bit is the number of events with 'track' logic bits divided by the number of events with the actual dc logic bits set. The efficiencies of the bits Y, YU, YD and 2Y determined in this fashion were all greater than .999 .

Appendix C. Accidental Pair Rate[70]

The accidental pair rate was determined using two hodoscope counters that could not be traversed by a single track emanating from the downstream end of the SM12 magnet. Real coincidences were minimized by the spill cuts, described in Section IV.G., which insured that the coincidence rate between the two counters was proportional to the square of the interaction rate in the target. Given the rates in the two counters, A and B, the probability of an accidental coincidence per proton is

$$P(A \wedge B)_{acc} = P(A) \times P(B),$$

where $P(A)$ =probability of a hit in counter A per proton. Let N_p = the number of incident protons per bucket and N_A = the total number of counts in A, then

$$P(A) = (N_A) / \sum_{buckets} N_p$$

and

[70] R.J. Fisk, Ph.D. Thesis, State University of New York at Stony Brook, (1978)

$$P(A \wedge B)_{acc} = (N_A \times N_B)/(\sum_{buckets} N_p)^2.$$

If $N^{acc}_{A\wedge B} = \sum_{buckets} N_p^2 P(A \wedge B)_{acc}$ is just the total number of accidental coincidences, then

$$\frac{N^{acc}_{A\wedge B}}{N_A \times N_B} = \frac{\sum_{buckets} N_p^2}{(\sum_{buckets} N_p)^2} \equiv \frac{1}{N_{eff}},$$

where N_{eff} is defined as the effective total number of buckets. If N_p were constant then N_{eff} would be the actual number of RF buckets. Hence the accidental pair rate is simply the product of the singles rates divided by N_{eff}.

Appendix D. Hadron Species Identification

Let $f^{\alpha}(\rho_1,\cdots,\rho_N)$ be the probability density for particle type α ($\alpha = \pi$,K, or p) to produce N detected photons at reduced radii $\rho_i, i = 1,2,\cdots,N$, where $\rho_i = R_i/R_\infty$ for the i^{th} photon at measured radius R_i and R_∞ is the radius of an infinite momentum track. In other words, $f^{\alpha}(\rho_1,\cdots,\rho_N)$ is the probability density evaluated at the point, $(\rho_1,\cdots,\rho_N)$, in N-dimensional reduced-radii space. Then

$$f^{\alpha}(\rho_1,\cdots,\rho_N) =$$

$$\sum_{j_1=0}^{1}\cdots\sum_{j_N=0}^{1}\left[\frac{P^{\alpha}_{\text{real}}(\sum_{i=1}^{N} j_i,\rho^{\alpha}_{\text{T}},R^{\alpha}_{\text{T}})P_{\text{junk}}(N-\sum_{i=1}^{N} j_i)}{\binom{N}{\sum_{i=1}^{N} j_i}}\right]\times$$

$$\prod_{i=1}^{N}\left\{j_i\frac{1}{\sqrt{2\pi}\sigma_i}\exp\left(-\frac{(\rho_i-\rho^{\alpha}_{T})^2}{2\sigma_i^2}\right)+(1-j_i)\frac{2\rho_i}{\rho^2_{max}}\right\}$$

where

ρ^{α}_{T} = predicted normalized radius for particle type α given track T,

j_i = 0 if the i^{th} photon is "junk" (not a Čerenkov photon) and

= 1 if the i^{th} photon is real,

N = number of detected photons with $\rho < \rho_{max}$, $\rho_{max} \approx 1.2$, and

R^{α}_{T} = predicted absolute radius for particle type α given track T.

The term in the square brackets is the probability of an interpretation of the reduced radii of an event $\{\rho_i\}$ given by the $\{j_i\}$. The N sums reflect the 2^N possible interpretations for a given set of N photons. The term multiplied by j_i in the curly brackets is the probability density for a single real photon with predicted variance, σ_i^2; the second term is the probability density for a junk photon in a ring of reduced radius ρ_{max} assuming a constant junk photon distribution for $\rho < \rho_{max}$.

$P^{\alpha}_{\text{real}}(n, \rho^{\alpha}_{\text{T}}, R^{\alpha}_{\text{T}})$ is the probability of detecting n real photons on a ring of predicted reduced radius ρ^{α}_{T} and absolute radius R^{α}_{T} for particle type α. P^{α}_{real} depends on a combination of 3 effects:

1) the particle velocity, β^{α}, since the number of produced Čerenkov photons is proportional to $\sin^2\theta_{\check{C}} = 1 - (1/n\beta)^2$,

2) the absolute ring radius, R^{α}_{T}, because the detector resolution of individual photons decreases as R^{α}_{T} decreases (nearby photons can become merged), and

3) the 'sparking' probability; that is, the probability that the detector is inefficient for a given event. This probability, p_{off}, ranges from about 0% to 15% on a run-to-run basis.

Explicitly, for the case of $n > 0$,

$$P^{\alpha}_{\text{real}}(n, \rho^{\alpha}_{\text{T}}, R^{\alpha}_{\text{T}}) = (1 - p_{\text{off}}) \times$$

$$\sum_{k=n}^{\infty} \text{Resprob}(n, k; R^{\alpha}_{\text{T}}) exp\left[-a\left(\frac{\rho^{\alpha}_{\text{T}}}{\beta^{\alpha}}\right)^2\right] \frac{\left[a\left(\frac{\rho^{\alpha}_{\text{T}}}{\beta^{\alpha}}\right)^2\right]^k}{k!}$$

and for $n = 0$,

$$P^{\alpha}_{\text{real}}(n, \rho^{\alpha}_{\text{T}}, R^{\alpha}_{\text{T}}) = p_{\text{off}} + (1 - p_{\text{off}}) exp\left[-a\left(\frac{\rho^{\alpha}_{\text{T}}}{\beta^{\alpha}}\right)^2\right],$$

where

n = number of detected photons,

a = mean number of detected real photons that hit the detector from an infinite momentum track, determined from muon tracks,

Resprob$(n, k; R^{\alpha}_{\text{T}})$ = resolution probability — the probability of resolving n photons in an event with k photons striking the detector with predicted absolute radius R^{α}_{T} for particle type α and track T, calculated by monte carlo technique utilizing the spatial resolution of the chamber and the photon–finding algorithm.

$P_{\text{junk}}(n)$ = probability of having n junk photons in an event, calculated on a run–by–run basis using muon tracks.

The $n > 0$ term in P^{α}_{real} is the probability of the detector being on times the sum over Poisson probability densities for $k \geq n$ photons folded with the resolution probability. The $n = 0$ term is simply the probability of the detector being off for an event plus the probability that no photons are emitted by track T of particle type α when the detector is on.

Appendix E. The Information Matrix[71]

If g_α is defined as the particle fraction in a given bin and f_α^i is defined as the probability density that track i is type α, then $g_\alpha f_\alpha^i$ is proportional to the probability that track i is type α. The likelihood equation is then

$$L = \prod_{i=1}^{N} \sum_{\alpha=1}^{3} f_\alpha^i g_\alpha,$$

where N = the total number of tracks. The maximum likelihood estimate of the particle fractions, g_α, are the values of g_α for which L is a maximum given the set of N independent observations f_α^i.[72] Hence the likelihood equation must be maximized subject to the constraint that $\sum_{\alpha=1}^{3} g_\alpha - 1 = 0$; in other words each track must be either π, K or p.

Use a Lagrange multiplier, λ, and maximize

$$X = \ln L + \lambda(\sum_{\alpha=1}^{3} g_\alpha - 1)$$

with respect to g_α, then

---

[71] P.B. Straub, Ph.D. Thesis; W.T. Eadie, D Drijard, F.E. James, M. Roos and B. Sadoulet, Statistical Methods in Experimental Physics, (North Holland, New York, 1971)

[72] W.T. Eadie *et al.*

$$\sum_{i=1}^{N} \frac{f_\alpha^i}{\sum_{\beta=1}^{3} f_\beta^i g_\beta} + \lambda = 0.$$

The value of λ follows immediately from the fact that

$$\sum_{i=1}^{N} \frac{f_\alpha^i g_\alpha}{\sum_{\beta=1}^{3} f_\beta^i g_\beta} = g_\alpha N,$$

so $\lambda = -N$. Thus the likelihood equations are

$$\xi_\alpha \equiv \frac{1}{N} \sum_{i=1}^{N} \frac{f_\alpha^i}{\sum_{\beta=1}^{3} f_\beta^i g_\beta} - 1 = 0.$$

Now define the true value of g_α to be g_α° and the likelihood estimator of g_α to be $\hat{g}_\alpha$[73] and expand $\xi_\alpha(g^\circ)$ to first order in a Taylor series about $\xi_\alpha(\hat{g})$:

$$\xi_\alpha(g^\circ) = \xi_\alpha(\hat{g}) + \sum_{\beta=1}^{3} (g_\beta^\circ - \hat{g}_\beta) \frac{\partial \xi_\alpha}{\partial g_\beta}\bigg|_{\hat{g}}.$$

Use the fact that $\xi_\alpha(\hat{g}) = 0$ and define the *information matrix*,

$$I_{\alpha\beta} \equiv \frac{\partial \xi_\alpha}{\partial g_\beta}\bigg|_{\hat{g}} = \frac{1}{N} \sum_{i=1}^{N} \frac{f_\alpha^i f_\beta^i}{\left(\sum_{\gamma=1}^{3} f_\gamma^i g_\gamma\right)^2},$$

so that

$$\xi_\alpha(g^\circ) = (g_\beta^\circ - \hat{g}_\beta) I_{\alpha\beta}.$$

[73] The estimator, $\hat{g}_\alpha$, is the value of g_α which solves ξ_α given the observed f_α^i.

Invert the information matrix.

$$(I^{-1})_{\alpha\beta}\xi_\alpha(g^\circ) = (g^\circ_\beta - \hat{g}_\beta)$$

and take the expectation value of $(g^\circ_\beta - \hat{g}_\beta)(g^\circ_\alpha - \hat{g}_\alpha)$ to obtain the covariance or error matrix for the particle fractions, g_α:

$$E\left[(g^\circ_\beta - \hat{g}_\beta)(g^\circ_\alpha - \hat{g}_\alpha)\right] = (I^{-1})_{\alpha\gamma}(I^{-1})_{\beta\eta}E\left[\xi_\gamma(g^\circ)\xi_\eta(g^\circ)\right].$$

Writing the expectation value of the product of likelihood equations explicitly,

$$E\left[\xi^\circ_\gamma\xi^\circ_\eta\right] = E\left[\left(\frac{1}{N}\sum_{i=1}^{N}\frac{f^i_\gamma}{\sum_{\beta=1}^{3}f^i_\beta g_\beta} - 1\right)\left(\frac{1}{N}\sum_{j=1}^{N}\frac{f^j_\eta}{\sum_{\beta=1}^{3}f^j_\beta g_\beta} - 1\right)\right].$$

The expectation value of a product of uncorrelated random variables is the product of the expectation values. In this case, $f^i_\gamma f^j_\eta$

are uncorrelated unless $i = j$,

$$E[\xi_\gamma^\circ \xi_\eta^\circ] = E\left[\frac{1}{N}\sum_{i=1}^{N}\frac{f_\gamma^i}{\sum_{\beta=1}^{3} f_\beta^i g_\beta} - 1\right] E\left[\frac{1}{N}\sum_{j=1}^{N}\frac{f_\eta^j}{\sum_{\beta=1}^{3} f_\beta^j g_\beta} - 1\right]$$
$$-\frac{1}{N^2}\sum_{i=1}^{N}\delta_{\gamma\eta} E\left[\frac{f_\gamma^i}{\sum_{\beta=1}^{3} f_\beta^i g_\beta}\right] E\left[\frac{f_\eta^i}{\sum_{\beta=1}^{3} f_\beta^i g_\beta}\right]$$
$$+\frac{1}{N^2}\sum_{i=1}^{N} E\left[\frac{f_\gamma^i f_\eta^i}{\left(\sum_{\beta=1}^{3} f_\beta^i g_\beta\right)^2}\right].$$

The second term on the right hand side of the above equation subtracts the incorrect uncorrelated terms present in the first term and the third term adds the correct correlated terms. This expression can be evaluated by noting that the first term is the product of the expectation value of the likelihood functions, $\xi_\gamma^\circ = 0$. Again using the likelihood equation, the second term becomes unity divided by N, and the final term can be identified with $I_{\gamma\eta}/N$. Thus

$$E\left[(g_\beta^\circ - \hat{g}_\beta)(g_\alpha^\circ - \hat{g}_\alpha)\right] = (I^{-1})_{\alpha\gamma}(I^{-1})_{\beta\eta}\frac{1}{N}\left(I_{\gamma\eta} - 1\right)$$

or, finally,

$$E\left[(g_\beta^\circ - \hat{g}_\beta)(g_\alpha^\circ - \hat{g}_\alpha)\right] = \frac{1}{N}\left[\left(I^{-1}\right)_{\alpha\beta} - \left(I^{-1}\right)_{\alpha\beta}^2\right].$$

The first term is readily identified with the normal variance while the second is the reduction due to the constraint, $\sum_{\alpha=1}^{3} g_\alpha = 1$. This final expression is the covariance or error matrix. Each diagonal element is the variance on each g_α and each off-diagonal element is the correlation of errors between the different particle fractions.